Hardware in the loop sloshing using a testbed platform

Marco Rubaga

Delft University of Technology & GMV Portugal

TU Delft

Hardware in the loop sloshing using a testbed platform

by

Marco Rubaga

to obtain the degree of Master of Science
at Delft University of Technology,
to be defended publicly on 12th of January 2026.

Student Number:	5031680
Project Duration:	April, 2025 - December, 2025
Faculty:	Faculty of Aerospace Engineering, Delft
University Supervisor:	Dr. Stefano Speretta
GMV Supervisor:	Nuno Paulino
Thesis Examination Committee:	Angelo Cervone - Chair
	Jasper Bouwmeester
	Stefano Speretta

TU Delft

gmv INNOVATING SOLUTIONS

Preface

This thesis serves as the final deliverable toward the Master of Science degree in Aerospace Engineering, with a specialization in Space Engineering, at Delft University of Technology. It marks the culmination of four years of study in Delft, where I completed my Bachelor's degree during a global pandemic and my Master's degree, the first half in Delft and the second half in Lisbon, Portugal.

I would like to begin by thanking my family. My parents, Dora and Luca, who have nurtured me, given me incredible opportunities, and constantly encouraged me to pursue my passions and strive for excellence. My sisters, Diana and Alice, for the shared journey we have had together and for remaining close to me despite the physical distance that currently separates us. I am also deeply grateful to my grandparents, Augusto and Lia, who have always supported my curiosity and curiosity-driven learning from a young age. To my girlfriend, Flavia, thank you for your unwavering support, not only throughout this thesis, but also during periods of significant change throughout my university career.

I would also like to thank my housemates Matteo, Fabien, Antonio, Ionut, and especially Giorgio, for the countless shared moments and for being willing, and sometimes unwilling, participants in my cooking experiments. To my close friends in Delft and Lisbon, Geko, Alfonso, Luigi, Sergio, Silvio, Emma, Alessandro C., Alessandro B., Niek, Tom, Jose, Eduardo, and Luis, thank you for your friendship and support along the way. To my friends in Vienna, Johannes, Davide, Caleb, and Darina, thank you for being part of this journey as well.

I am grateful to my supervisors, Stefano Speretta and Nuno Paulino, for their guidance, patience, and support over the past nine months. Finally, I would like to thank the GMV Portugal office for the opportunity to conduct my thesis work within industry.

Thank you to everyone who has supported me throughout this journey. Your encouragement, kindness, and presence have been an essential part of what made this achievement possible.

Marco Rubaga

Lisbon, December 2025

Summary

Sloshing in liquid filled tanks remains a critical challenge for modern aerospace systems due to its strong coupling with spacecraft attitude dynamics. As contemporary missions demand higher agility, employ larger propellant tanks, operate over longer lifetimes, and must comply with ESA's Debris Mitigation Policy through guaranteed deorbiting, the influence of sloshing induced forces and torques becomes increasingly significant. These disturbances can degrade pointing performance, excite flexible structures, increase actuator usage, and, in extreme cases, lead to loss of mission. Both historical flight anomalies and more recent incidents, such as the SpaceX Falcon 1 failure in 2007, demonstrate that sloshing continues to pose a real risk to guidance and control systems. This motivates the need for experimental platforms capable of investigating sloshing dynamics in a controlled and repeatable manner, with a particular focus on regimes relevant to spacecraft attitude control.

Sloshing arises when the free surface of a liquid oscillates in response to external excitation, producing wave patterns that shift the instantaneous center of mass of the fluid. When the excitation frequency approaches a natural sloshing mode, resonance occurs and significant disturbance forces and torques are transmitted to the supporting structure. While sloshing is inherently a nonlinear free surface phenomenon, its behavior at small amplitudes can often be approximated using simplified mechanical analogues, most commonly equivalent pendulum models.

Replicating representative sloshing conditions on ground based platforms is inherently challenging, especially when attempting to capture behavior relevant to space applications. A key dimensionless parameter governing sloshing behavior is the Bond number, which characterizes the relative importance of gravitational forces compared to surface tension. Low Bond number conditions, which are common in space systems, are difficult to achieve under Earth gravity. Consequently, experimental studies must rely on scaling and equivalency principles to relate ground test results to flight conditions. This challenge directly motivates the first research question of this thesis: *To what extent can an on ground test platform replicate and characterize relevant sloshing regimes for spacecraft in microgravity and launch vehicles in high g regimes?*

For control oriented analysis, linear representations of sloshing are particularly valuable because they enable straightforward evaluation of stability margins and robustness. However, such models are only valid over a limited excitation range. As excitation amplitude increases, nonlinear effects such as wave steepening and amplitude dependent frequency shifts emerge. Identifying the range over which sloshing behavior can be treated as approximately linear, and determining reliable indicators for the transition to nonlinear dynamics, therefore constitutes a central objective of this work. This directly motivates

the second research question: *How accurately do existing sloshing models, both linear and nonlinear, predict the behavior observed on the test platform?*

These questions are investigated experimentally using the TRACTOR platform. Originally developed to study flexible structures and robotic interaction in the context of in orbit assembly, the platform consists of a rigid central body supported by a low friction thrust bearing, enabling near free rotation about a single vertical axis. For the purposes of this thesis, the flexible elements and robotic walker were removed and replaced by a rigidly mounted sloshing tank. This configuration results in a single rotational degree of freedom that closely resembles spacecraft yaw dynamics, making the platform well suited for studying rotationally excited sloshing and its coupling to attitude motion.

Excitation of the platform is provided by a reaction wheel that applies torque directly about the rotational axis, allowing precise control of the excitation profile through sinusoidal sweeps in torque. The platform is instrumented with inertial sensors measuring angular rate and linear acceleration, enabling accurate capture of the dynamic response of the combined platform–tank system. Prior to sloshing experiments, the intrinsic dynamics of the platform were characterized, including estimation of the total rotational inertia, identification of nonlinear friction in the bearing and drivetrain, and assessment of preferential excitation directions arising from small structural asymmetries.

To extract sloshing dynamics from experimental data, both time domain and frequency domain identification approaches were investigated. Time domain methods were found to be ineffective due to contamination of the measurements by nonlinear bearing friction and sensor noise. As a result, a frequency domain identification approach was adopted. Frequency response functions derived from angular velocity measurements were estimated and fitted using MATLAB's *tfest* function. The identified models were constrained to three poles and two zeros, consistent with the expected linear sloshing representation. This methodology enabled systematic evaluation of changes in resonant frequency, notch depth, coherence, and signal to noise ratio as excitation amplitude increased, providing clear indicators of the onset of nonlinear behavior.

The experimental results were compared against synthetic data generated using a strictly linear sloshing model implemented on an analogous platform. By subjecting the synthetic model to the same excitation profiles as the experiments, direct comparisons between linear predictions and measured responses were obtained.

The results reveal clear signatures of nonlinear sloshing as excitation amplitude increases beyond approximately 0.1 Nm in amplituide. The first sloshing mode exhibits amplitude dependent frequency shifts, a hallmark of nonlinear behavior, while the coherence between the input torque and residuals decreases as nonlinear dynamics become more pronounced. At low excitation amplitudes, where linear behavior was expected, observability was limited by poor sensor signal to noise ratios. At higher amplitudes, increased platform nutation due to static and dynamic imbalances introduced energy into unintended degrees of freedom, reducing the clarity of the observed nonlinear phenomena. Despite

these limitations, a clear divergence between synthetic linear predictions and experimental data was observed, supporting the conclusion that the measured effects are at least partially attributable to nonlinear fluid behavior. The Bond number regime achieved during testing was found to be equivalent to that of the liquid oxygen tank of a Centaur upper stage with its reaction control thrusters active. This supports the ability of the platform to replicate and study sloshing phenomenon that occur in space in a laboratory setting.

Based on the experimental findings, several recommendations were formulated to improve experimental methodology, model fidelity, and platform design. These include replacing the inertial sensors with higher performance units capable of cleaner low amplitude measurements and improved estimation of angular accelerations and platform tilt. Expanding the sensor suite to include cameras for direct measurement of wave height and surface shape was also recommended. From a modeling perspective, the use of conical pendulum representations allows to more closely match experimental nonlinear behavior, leading to more precise identification of nonlinearity onset. Finally, platform enhancements were proposed, including increasing the torque bandwidth of the reaction wheel to enable broadband excitation, mounting the system on an air bearing to reduce nonlinear friction effects, and improving mechanical tolerances to correct existing misalignments.

Contents

Nomenclature

Symbols

Symbol	Definition	Unit
A	Surface area (e.g., cross-section of tank or pendulum segment)	[m^2]
Bo	Bond number (non-dimensional gravity-capillary ratio)	[-]
C	Damping coefficient or constant in mechanical models	[N·s/m]
d	Characteristic diameter or tank width	[m]
f	Frequency of excitation or slosh mode	[Hz]
F	Force (total slosh force or actuator force)	[N]
g	Gravitational acceleration	[m/s^2]
h	Fill height of liquid in tank	[m]
H_n	Pendulum segment height (in multi-pendulum model)	[m]
I	Moment of inertia (of system/platform)	[$kg·m^2$]
k	Spring stiffness	[N/m]
K_n	Effective stiffness of pendulum segment n	[N/m]
L	Characteristic length or tank length	[m]
m	Mass	[kg]
m_n	Mass of pendulum segment n	[kg]
n	Slosh mode number	[-]
Q	Quality factor (related to damping)	[-]
R	Radius (e.g., of spherical tank)	[m]
Re	Reynolds number	[-]
t	Time	[s]
T	Period of oscillation	[s]
u, v, w	Velocity components in x, y, z directions	[m/s]
V	Translational velocity (e.g., tank or fluid velocity)	[m/s]
X_0	Amplitude of tank motion or platform sweep	[m]

Symbol	Definition	Unit
x_n	Displacement of pendulum segment n	[m]
α	Angular displacement (e.g., pitch angle, pendulum angle)	[rad]
δ	Free surface displacement (sloshing wave elevation)	[m]
Δ	Logarithmic decrement (used in damping)	[-]
γ	Damping ratio (dimensionless)	[-]
λ	Eigenvalue / spatial wave number / thermal conductivity (context dependent)	[1/m] or [W/m·K]
μ	Dynamic viscosity	[Pa·s]
ν	Kinematic viscosity	[m^2/s]
ϕ	Velocity potential in sloshing analysis	[m^2/s]
ρ	Fluid density	[kg/m^3]
σ	Standard deviation or stress (in context of uncertainty or material response)	[-] or [Pa]
τ	Time constant or shear stress	[s] or [Pa]
θ	Angular displacement (often used for pendulums)	[rad]
ω	Angular frequency (of sloshing or excitation)	[rad/s]

Acronyms

ABMA Army Ballistic Missile Agency. 35

AOCS Attitude and Orbit Control System. 4, 30

ARMAX Autoregressive Moving Average with Exogenous Inputs. viii, 109, 110

ARX Autoregressive with Exogenous Input. viii, 109, 110

CEF Cross-axis Energy Fraction. 85, 96, 97

CFD Computational Fluid Dynamics. 6, 14, 22, 27, 35

CMG Control Moment Gyroscope. 30

CNES Centre National d'études Spatiales. 35

CoM Centre of Mass. 30, 39

EoL End of Life. 4

EoM Equation of Motion. 21, 44, 111

ESA European Space Agency. 1, 4, 35, 39

FRF Frequency Response Function. xiv, 77, 78, 80–82, 92, 96, 97, 102–106, 111

GNC Guidance and Navigation. 1, 2

ICBM Intercontinental Ballistic Missile. 3

IMU Inertial Measurement Unit. xiii, xiv, 5, 37, 38, 57, 60, 67–69, 76, 80, 84, 103, 106–108, 110, 113

IOA In Orbit Assembly. 1, 2

IOANT In-Orbit Assembly with Navigation and Control Technologies. 1–3, 60, 61, 68

LNG Liquefied Natural Gas. 32

NLLS Nonlinear Least Squares. xiv, 73–75

ODE Ordinary Differential Equation. 52, 109

PDE Partial Differential Equation. 9

RCS Reaction Control Thrusters. 99, 101, 105

RW Reaction Wheel. 30, 36

S/C Spacecraft. 5, 41, 44, 104

SNR Signal to noise ratio. 84, 95, 105, 106

TF Transfer Function. 52

TRACTOR Test Rig for Analysis and Control of Traveling Oscillations in a Resonant Beam. 2, 5, 40, 106, 112, 113

TRL Technology Readiness Level. 2

List of Figures

List of Tables

1

Thesis Context & Introduction

This master's thesis was carried out within the GNC division of the Flight Segment and Robotics unit of GMV Portugal. While the thesis specifically investigates the phenomenon of sloshing in propellant tanks, it is embedded within the broader context of the In-Orbit Assembly with Navigation and Control Technologies (IOANT) project and makes use of shared hardware components. The following sections will provide an overview of the IOANT project's objectives and detail the hardware employed throughout the thesis.

1.1. IOANT Project

The IOANT project, supported by the European Space Agency (ESA), is an advanced research initiative focused on developing the key technologies required for the autonomous In Orbit Assembly (IOA) of large-scale space antennas [3][51]. As future space missions increasingly demand larger and more capable structures, particularly in telecommunications, Earth observation, and deep-space exploration the limitations of launch vehicle dimensions and deployable mechanisms become critical bottlenecks. IOANT addresses these constraints by enabling the construction of modular antenna systems directly in space, allowing for significantly larger apertures than what is currently achievable with monolithic or folded designs.

The primary goal of the project is to develop and validate a robust Guidance and Navigation (GNC) system capable of autonomously coordinating the entire assembly process [3][51]. This includes precise handling of structural modules using robotic manipulators, real-time navigation in a microgravity environment, and adaptive control strategies that account for evolving system dynamics such as changes in the overall mass, inertia, and structural flexibility of the antenna as new components are added. This is portrayed in Figure 1.1 demonstrating the in orbit assembly of large antennas, where a walking tripedal

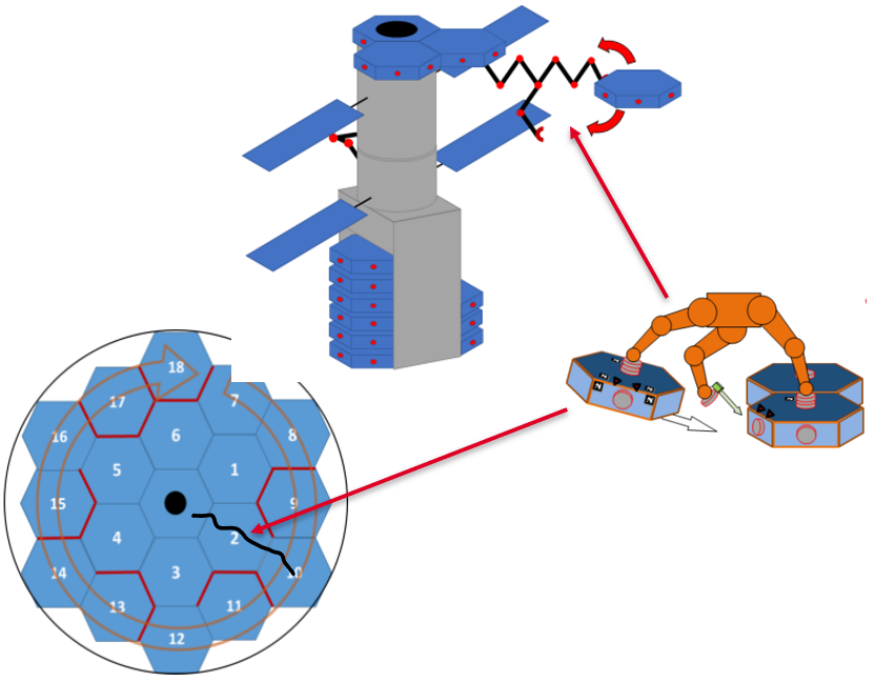

Figure 1.1: In orbit assembly of large antennas [3][51]

robot takes antenna segments and assembles them in orbit.

The IOANT project is structured in two phases:

1. A simulation phase, where a complete GNC solution is designed, modeled, and tested within a high-fidelity dynamic environment.
2. A hardware validation phase, which includes ground-based experiments using scaled-down prototypes to demonstrate key aspects of the GNC system and robotic assembly.

By achieving a Technology Readiness Level (TRL) of 4/5, the IOANT project seeks to establish the foundational technologies necessary for future on-orbit construction missions. It ultimately aims to enable scalable, reconfigurable, and maintainable space infrastructures, reducing dependency on complex deployment mechanisms and paving the way for next-generation orbital platforms[51].

1.2. Hardware

Throughout the masters thesis the author has worked in the IOANT project designing, building and testing the hardware utilized for the scaled down experiments. The piece of hardware is called Test Rig for Analysis and Control of Traveling Oscillations in a Resonant Beam (TRACTOR) and it is meant to emulate the challenges in the scenario of IOA, a central structure housing actuators and providing a near frictionless rotating surface with a single degree of freedom representing the antenna segment stack, a flexible structure mimicked with a slim beam and an assembly robot represented by a walker moving on the flexible beam [51]. This scale experiment replicating different aspects of IOA is shown

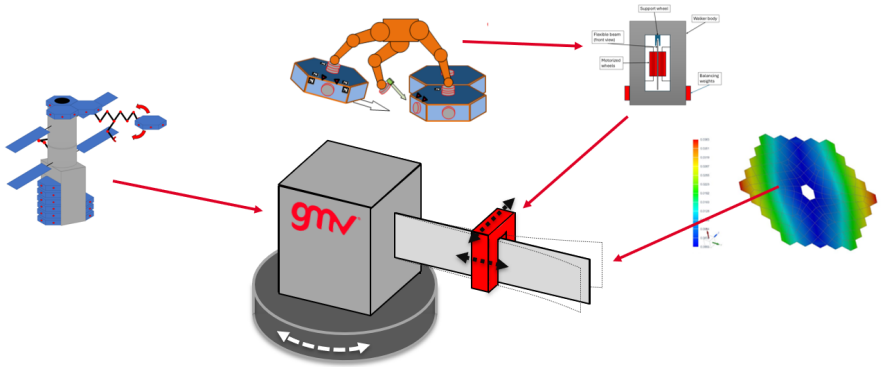

Figure 1.2: Tractor Beam [3]

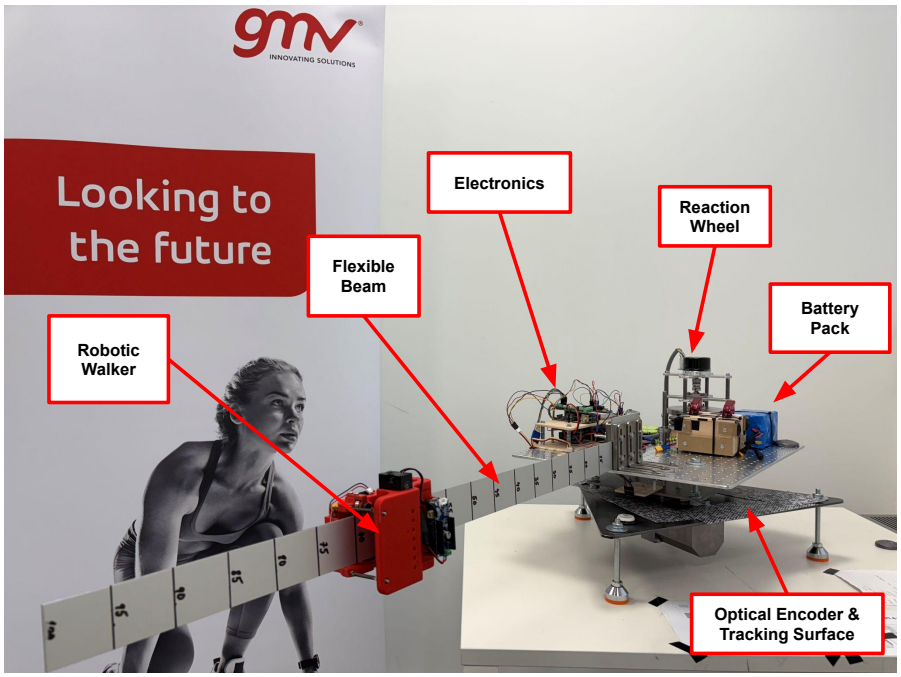

Figure 1.3: Fully Assembled TRACTOR platform with beam for flexible mode analysis mounted

in Figure 1.2, this has then been brought to reality with an actual hardware structure. The structure is shown in Figure 1.3 as used in the IOANT experiments, for the purposes of the thesis the beam and walker are not utilized and are removed, being replaced by a sloshing tank. The only shared components are the avionics, actuator, sensors and thrust bearing.

1.3. Introduction

Sloshing in propellant tanks from space vehicles is an effect that has been known since 1957, with the first reported catastrophic instance of sloshing occurring during the launch of Jupiter Intercontinental Ballistic Missile (ICBM) on April 26th of 1957 [41]. In this occasion the steps in guidance for gravity turn synchronized with the sloshing mode of the liquid oxygen tank resulting in total vehicle loss: this problem was mitigated in further flights by introducing baffles within the tanks to dampen the sloshing

mode. In 2001 the NEAR satellite went into safety mode due to unexpected reaction following an orbital maneuver strongly suspected being the result of sloshing, causing a one year delay to the project [47]. The problem has not been completely mitigated in modern times, with the launch of SpaceX Falcon 1 in 2007 suffering a total loss of the second stage due to a high altitude gust exciting the sloshing mode of the fuel tank, causing it to resonate with the structure leading to a premature engine shutdown and payload loss [54].

Similarly to launch vehicles, sloshing is a cause of concern in satellites, where it can be excited during orbit corrections or orientation manoeuvres and may enter into resonance with flexible structures such as solar arrays and antennas that have low resonant frequencies. Sloshing in satellites also causes tumbling motions which require a large expenditure in fuel to correct, limiting the useful mission lifetime [26].

Furthermore, sloshing, and its accurate modeling are becoming an ever more important topic in recent years, as modern satellites face competing requirements that pose important sloshing related challenges. As part of the ESA Space Debris Mitigation Policy, international standard ISO 24113 has been adopted [19]. It outlines key guidelines for space debris mitigation, including design and operational measures, maximum debris lifetimes, casualty risk thresholds for reentry, mandatory passivation of energy sources, and criteria distinguishing controlled from uncontrolled reentry [19]. These requirements are enforced across ESA missions to limit long-term debris proliferation and reduce risks to both orbital assets and populations on Earth. This requirement has imposed the need for increased actuation during End of Life (EoL) phase, resulting in larger fuel tanks on new satellites.

As tank sizes increase, so does the impact of sloshing on spacecraft dynamics, especially within the AOCS. This gives rise to competing requirements: on one hand, missions demand high pointing accuracy, precise center-of-mass control, and quick fuel settling times, all of which are degraded by sloshing [26]. On the other hand, operational needs such as fast re-pointing maneuvers and orbit changes inherently excite sloshing, worsening the very effects engineers seek to suppress. This tension between agility and stability makes fuel sloshing a central and challenging topic in modern Attitude and Orbit Control System (AOCS) design [26]. There is a clear need for research to be done on sloshing, being able to accurately predict sloshing in space and high fidelity sloshing models.

2

Literature Study

State of the Art

Despite its critical relevance across aerospace, marine, and automotive applications, sloshing remains an underrepresented topic in the broader scientific literature. The most comprehensive and authoritative compilation of foundational knowledge is found in the book ”Dynamic Behavior of Liquids in Moving Containers” written by Franklin T. Dodge [16] in the 1960’s and updated since. This book continues to serve as the principal reference for analytical formulations and linear mechanical model development in sloshing studies. This work has been extensively cited and relied upon due to its rigorous treatment of linear sloshing theory, which has historically dominated the field. However, recent research trends are increasingly shifting toward nonlinear [37] [5], complex sloshing dynamics coupled to structures [38]. This shift has come about due to increased Spacecraft (S/C) agility which can excite nonlinear sloshing modes that need to be accurately modeled and controlled to meet stringent pointing requirements. Linear sloshing of modeling may miss certain important aspects such as rotary sloshing [37] and thus introducing unwanted torques. This has driven the growing need for advanced, high-fidelity representations.

The state of the art for platforms to investigate sloshing on Earth mainly excite the liquid through lateral harmonic translations [18]. This is also what is expected in typical linear sloshing theory (relying on linear inputs). These platforms have used a variety of tank shapes, spherical, cylindrical and rectangular with IMU’s and cameras used to sense the movement of the liquid or the structure the tanks are mounted on [18]. The only rotary on ground test platform found in literature is described by [38], which corresponds to a tank placed in a simulated spacecraft spinning about the Z axis with a maximum slew rate of 20 deg/sec. The TRACTOR platform, with its single degree of freedom in rotation around Z-axis allows for continued research using rotary excitation, additionally the TRACTOR platform can

perform slews up to 40 deg/sec allowing to it to better mimic the performance characteristics of an agile satellite.

Sloshing in different gravity fields, particularly microgravity has been a topic of interest since the 1960's as the first satellites where launched. Classically linear sloshing theory is quite limited and cannot model the liquid behavior in microgravity requiring specialized models to be built, either equivalent mechanical models and or when computing power became available Computational Fluid Dynamics (CFD), which has been validated by use of flight data; either from 0g flights or from spaceflights [58][12]. As computers become more powerful and computing power becomes cheaper CFD is more heavily relied on for microgravity simulations. Ground platforms can investigate different gravity regimes by varying the size of their tank with respect to the local gravity conditions, a process known as Bond number equivalency [38] [16].

2.1. Analytical Description

Lateral sloshing is considered in this thesis due to its significant impact on spacecraft stability and control, particularly during attitude maneuvers and trajectory corrections. Unlike axial sloshing, which often aligns with the primary direction of thrust (and will be treated further on), lateral sloshing introduces transverse forces and moments that can couple with the spacecraft's attitude dynamics. These interactions are especially critical in microgravity environments, where even small lateral motions of the fluid can induce perturbations that compromise pointing accuracy and control authority.

The analytical treatment of lateral sloshing begins with the assumption of an ideal fluid, an incompressible, inviscid, and irrotational liquid contained in a rigid container. Under these assumptions, the flow can be described using potential theory. A fixed cartesian x,y,z coordinate frame is shown in Figure 2.1, this coordinate frame is attached to and moves with the tank. Translational and yaw oscillations are shown along the x and y axes, and roll oscillations along z axis. Angular oscillations α_y and roll α_z are shown. The inertial X,Y,Z coordinate system is stationary.

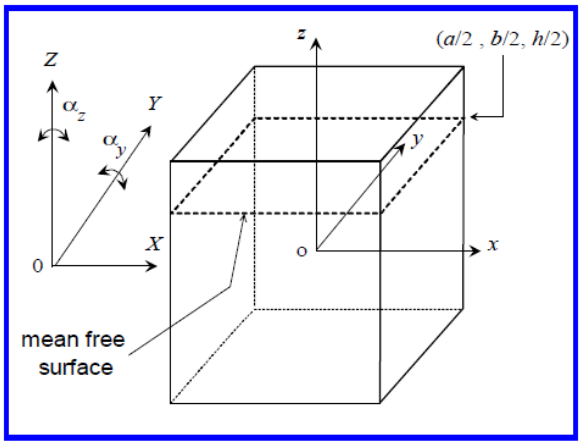

Figure 2.1: Coordinate system utilized for the derivation of slosh equations [16]

Due to the initial assumptions, the fluid velocity field $\vec{v}$ is given by the gradient of a velocity potential function Φ. The x,y,z components of the velocity u,v,w are computed from the spatial derivative of the potential.

$$u = \frac{\partial \Phi}{\partial x} \qquad v = \frac{\partial \Phi}{\partial y} \qquad w = \frac{\partial \Phi}{\partial z} \qquad \vec{v} = \nabla \Phi$$

The velocity potential must satisfy the condition of incompressibility given by the Laplace equation:

$$\nabla \cdot v = 0 \Leftrightarrow \nabla^2 \Phi = 0$$

This forms the core of analytical expressions of sloshing valid across all coordinate systems. The motion of the tank is assumed to be harmonic varying in time as exp(iΩt), with Ω as the frequency of motion. Multifrequency time dependent motions of the tank are expressed utilizing Fourier series [16].

The equation of motion for sloshing can be found by utilizing the unsteady form of Bernoulli's equation. In the context of potential flow theory, the unsteady Bernoulli equation relates the pressure field to the velocity potential Φ, fluid density ρ, gravitational acceleration g, and local velocity components u, v, w. The general nonlinear form of the equation is:

$$\frac{\partial \Phi}{\partial t} + \frac{p}{\rho} + gz + \frac{1}{2}\left(u^2 + v^2 + w^2\right) = f(t) \tag{2.1}$$

Here, p is the pressure, z is the vertical coordinate (positive upward), and $f(t)$ is an arbitrary function of time that arises from integration. Since only the derivatives of the velocity potential Φ carry physical meaning, the function $f(t)$ can be absorbed into the definition of Φ without affecting the dynamics.

In practical sloshing problems, especially under small-amplitude motion, the velocity components u, v, and w are sufficiently small that the nonlinear term $\frac{1}{2}(u^2 + v^2 + w^2)$ may be neglected. This results in a linearized form of the Bernoulli equation:

$$\frac{\partial \Phi}{\partial t} + \frac{p}{\rho} + gz = 0 \tag{2.2}$$

This linearized equation is widely used in analytical slosh modeling, as it provides a tractable relationship between the potential function and the pressure distribution in the fluid, assuming small-amplitude, irrotational, and incompressible flow within a rigid container [16] [22].

2.1.1. Boundary Conditions

Mathematical solutions of Equation 2.2 must be tailored to satisfy the boundary condition on the walls and free surface of the tank.

Free Surface

The surface is free to move so if the gas density is negligibly small compared to the liquid, the pressure at the surface is equal to the static pressure p_o of the gas above. The nonlinear Brenoulli equation (Equation 2.1) for the liquid at the free surface is written as:

$$\frac{\partial \Phi(x,y,z,t)}{\partial t} + g\delta(x,y,t) = -\frac{p_o}{\rho} \quad \text{for } z = h/2 \tag{2.3}$$

$\Phi(x,y,z,t)$ is the small displacement of the free surface above the undisturbed level z = h/2. Equation 2.3 can be interpreted as the dynamic condition at the free surface, enforcing the pressure balance. A kinematic condition is also required, this ensures that the fluid particles on the free surface stay attached to that surface, Equation 2.4 demonstrates this.

$$\frac{\partial \delta}{\partial t} = w = \frac{\partial \Phi}{\partial z} \quad \text{for } z = \frac{h}{2} \tag{2.4}$$

These two conditions link the fluid motion (via velocity potential Φ) to the shape and evolution of the free surface δ. The kinematic condition tells us how the surface moves in response to fluid motion. The dynamic condition tells us how the fluid pressure responds to surface motion. They are combined by differentiating Equation 2.3 w.r.t. t and Equation 2.4 w.r.t. z, combining the two results in Equation 2.5. This is evaluated at the point $z = h/2$ as this is the fill level for which the largest sloshing effects are generally seen.

$$\frac{\partial^2 \Phi}{\partial t^2} + g\frac{\partial \Phi}{\partial z} = 0 \quad \text{for } z = h/2 \tag{2.5}$$

The time derivative of Φ will include the natural frequencies of the sloshing. The frequencies are directly related to the imposed gravity field.

Boundary condition at wall

As viscosity and viscous stresses have been assumed to be negligibly small the only condition that can be imposed at the tank wall is the liquid velocity perpendicular to the plane of the wall has to be equal to the velocity V_n (n for normal) of the tank wall perpendicular to itself. The usual no slip condition cannot be imposed. Due to the tank not being stationary, the usual boundary condition (liquid velocity perpendicular to a tank being equal to 0) cannot be applied: the tank oscillations back and fourth cause a nonstandard wall boundary problem which can be solved by utilizing Fourier series [16].

Since the sloshing problem is assumed to be linear, a series of individual mathematical problems can be considered. A single different type of problem for different types of interested tank motions. The results of these individual problems are added up to obtain the velocity potential for entire motion. These standard motions are:

Tank Motion Type	**Boundary Condition at Wetted Surfaces**
Horizontal motion (x-axis)	$\mathbf{n} \cdot \nabla\Phi = iX_0\Omega e^{i\Omega t}$
Pitching motion (y-axis)	$\mathbf{n} \cdot \nabla\Phi = (\mathbf{z}e_x - xe_z)\alpha_0\Omega e^{i\Omega t}$
Rolling motion (z-axis)	$\mathbf{n} \cdot \nabla\Phi = (\mathbf{x}e_y - ye_x)\gamma_0\Omega e^{i\Omega t}$

Table 2.1: Boundary conditions at wetted surfaces for different tank motions [16], [22]

In Table 2.1, Φ is the velocity potential, $\mathbf{n}$ is the outward unit normal to the surface, and e_x, e_y, e_z are the unit vectors in the x-, y-, and z-directions, respectively. X_0 is the amplitude of horizontal displacement, α_0 and γ_0 are the amplitudes of pitching and rolling oscillations, Ω is the angular frequency, and $e^{i\Omega t}$ represents harmonic motion.

Other types of excitations will not be explicitly shown in derivations but have been utilized in different experiments. These other types of excitations are sinusoidal, ramp, random or rotational [18]. In particular rotational excitation of sloshing has not been extensively studied and therefore represents a gap in current literature. These excitation types are important to study since in nature the excitation sources of sloshing do not follow sinusoidal patterns as is often the case in theorized ideal calculations [18].

2.1.2. Solutions of Equations

To analytically determine the sloshing modes of a fluid in a container, we solve the Laplace equation under the assumptions of an ideal, incompressible, inviscid, and irrotational fluid. The objective is to find the velocity potential $\Phi(x, y, z, t)$ that satisfies $\nabla^2\Phi = 0$. This equation must be solved subject to appropriate boundary conditions:

- no flow through the rigid walls,
- no flow through the bottom of the tank, and
- free-surface boundary conditions (both kinematic and dynamic).

Each different standard tank shape can be described as its own problem with its own analytical solutions, a number of different tank shapes are described in the book ”The new dynamic behavior of liquids in moving containers” written by Franklin T. Dodge[16]. These yield the natural sloshing frequency, and resulting forces.

Rectangular tank

Consider a rectangular tank of width L and depth H, extending infinitely in the y-direction (2D approximation). We assume time-harmonic motion of the form:

$$\Phi(x, z, t) = \phi(x, z)e^{i\omega t}$$

Substituting into the Laplace equation gives:

$$\frac{\partial^2\phi}{\partial x^2} + \frac{\partial^2\phi}{\partial z^2} = 0$$

We solve this using separation of variables:

$$\phi(x, z) = X(x)Z(z)$$

Substituting into the Partial Differential Equation (PDE) yields:

$$\frac{1}{X}\frac{d^2X}{dx^2} + \frac{1}{Z}\frac{d^2Z}{dz^2} = 0 \quad \Rightarrow \quad \frac{d^2X}{dx^2} + \lambda^2 X = 0, \quad \frac{d^2Z}{dz^2} - \lambda^2 Z = 0$$

where λ is the separation constant and corresponds to the spatial frequency of the sloshing mode.

Boundary Conditions and Solutions

- Side walls (no flow): $\frac{\partial \Phi}{\partial x} = 0 \Rightarrow \frac{dX}{dx} = 0$ at $x = 0, L$, leading to cosine solutions:

$$X(x) = \cos\left(\frac{n\pi x}{L}\right), \quad \lambda = \frac{n\pi}{L}, \quad n = 0, 1, 2, \ldots$$

- Bottom wall (no vertical flow): $\frac{\partial \Phi}{\partial z} = 0$ at $z = 0$, giving:

$$Z(z) = A\cosh(\lambda z)$$

- Free surface (linearized dynamic condition):

$$\frac{\partial^2 \Phi}{\partial t^2} + g\frac{\partial \Phi}{\partial z} = 0 \quad \text{at } z = H$$

  Substituting the assumed time-harmonic form yields:

$$-\omega^2\phi + g\frac{\partial \phi}{\partial z} = 0 \quad \Rightarrow \quad \frac{dZ}{dz} = \frac{\omega^2}{g}Z \quad \text{at } z = H$$

Natural Frequencies

Applying the boundary condition at the free surface gives the dispersion relation:

$$\omega_n^2 = g\lambda_n \tanh(\lambda_n H), \quad \text{where } \lambda_n = \frac{n\pi}{L}$$

The resulting eigenfunctions $\phi(x, z)$ describe the sloshing mode shapes, while the corresponding eigenvalues ω_n represent the natural sloshing frequencies. In rectangular tanks, these solutions take the form of trigonometric and hyperbolic functions, and their characteristics depend on the tank dimensions and fluid depth. This equation can also be expressed in terms of tank width and height:

$$\omega_n^2 = \pi(2n-1)\left(\frac{g}{a}\right)\tanh\left[\pi(2n-1)\left(\frac{h}{a}\right)\right]$$

subscript n indicated mode number n. Frequency decreases as the depth h decreases or the tank width a increases. Naturally n=1 is the mode with the lowest frequency.

Sloshing Wave shape

In Figure 2.2 the wave shape for symmetric and antisymmetric sloshing is demonstrated. Force results only from antisymmetric sloshing, this is due to a relative shift in the center of mass of the liquid (Denoted as c.m. in the figures), creating a moment arm. Symmetric modes, lacking a moment arm produce no lateral forces and torques [16], the energy from input goes into producing standing waves. This makes antisymmetric sloshing more interesting for slosh in the context of space. The c.m. shift for the first antisymmetric mode n = 1 is substantially greater than in following modes with the same maximum wave amplitude, n=1 wave produces much greater forces and torques than any other mode.

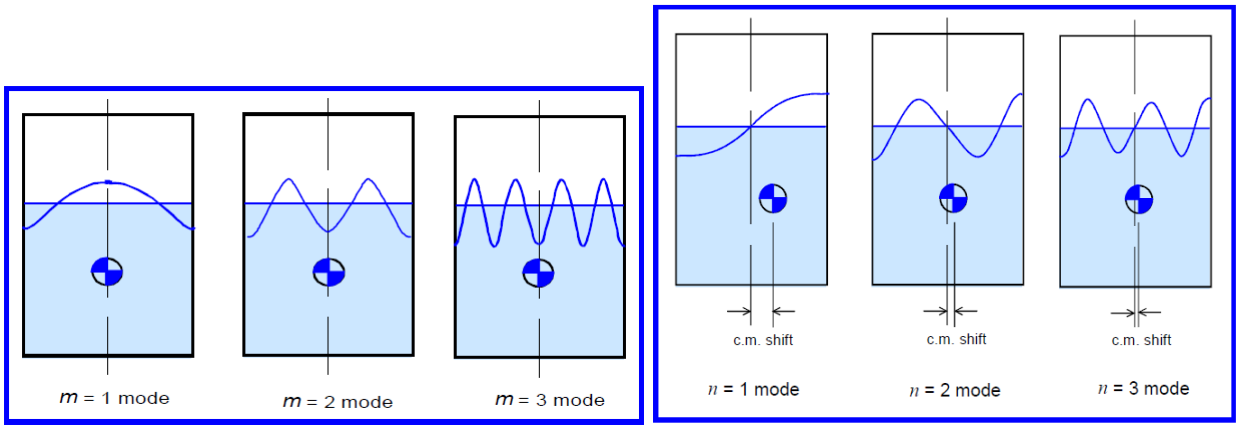

Figure 2.2: Shape of symmetric and antisymmetric sloshing modes for rectangular tank. [16]

The waves treated so far have been 2D waves, however for a 3D situation waves, the calculation of the natural frequency of which is not trivial to demonstrate but the shape is a summation of the 2D x and y shapes [16].

2.1.3. Resultant Forces and Torques

The calculation of the forces and torques induced by sloshing is based on the pressure distribution obtained from the linearized unsteady Bernoulli equation. Under the assumption of an inviscid, incompressible, and irrotational fluid, the pressure field is given by:

$$p = -\rho \left(\frac{\partial \Phi}{\partial t} + gz \right)$$

To compute the total force $\mathbf{F}$ and torque $\mathbf{M}$ exerted by the fluid on the tank, this pressure is integrated over the wetted surface of the container. For example, the x-component of the total force is:

$$F_x = -\rho \int_{\text{wall}} \frac{\partial \Phi}{\partial t} \, dA_x$$

The corresponding torque components are calculated by integrating the moment of the pressure forces relative to a reference point, such as:

$$M_y = -\rho \int_{\text{wall}} \left(z \frac{\partial \Phi}{\partial t} \right) dA_x$$

These expressions reflect the contribution of unsteady pressure acting along displaced surface elements. To evaluate them, the velocity potential Φ is typically expanded in terms of sloshing eigenfunctions that satisfy the Laplace equation and the tank's boundary conditions. These boundary conditions depend on the imposed tank motions and are summarized in Table 2.1.

It is important to note that the sloshing response depends on the frequency of the imposed motion. When the excitation frequency is much lower than the lowest sloshing natural frequency, the fluid tends to

behave as if it were frozen that is, it moves rigidly with the tank without significant free surface deformation. In contrast, when the excitation approaches one of the natural sloshing frequencies, dynamic amplification occurs, and the liquid response becomes dominated by slosh wave modes. As the excitation frequency increases far above the natural resonant frequency the liquid returns to behaving like a frozen liquid.

2.1.4. Tank Shapes

The same analysis to yield the eigenfunctions, eigenvalues, natural frequency, wave shape, force and torques has been done for a number of different tank shapes. The tank shapes described in [16] provide the detailed analytical solutions (which are however not shown for brevity) for the following tank shapes:

- Rectangular Tank
- Circular Cylindrical Tank
- Sector-Annular Cylindrical Tank
- Horizontal Cylindrical Tank
- Spherical Tank
- Toroidal Tank

The rectangular tank, characterized by flat walls and right-angled corners, is often used in laboratory experiments due to its geometric simplicity and well-defined boundary conditions. It serves as a baseline geometry for validating analytical and numerical models of sloshing dynamics. Though not common in flight systems, it may appear in modular or compact spacecraft fuel tanks[18]. The sloshing modes in rectangular tanks are relatively simple to model and exhibit strong lateral wave motions, making them useful for fundamental sloshing studies[22].

The circular cylindrical tank is widely used in rockets and launch vehicles [18] because of its structural efficiency and symmetry, which facilitate even pressure distribution and predictable fluid behavior. These tanks are often used in space applications for storing cryogenic and hypergolic propellants [18]. The sloshing modes in this geometry are described by Bessel functions, and both axisymmetric and asymmetric modes can be derived analytically[16][22].

Sector-annular cylindrical tanks are wedge-shaped and represent a segment of a hollow cylinder. This geometry is relevant in spacecraft designs where tanks must be arranged around a central structure such as an antenna mast or payload [18], where a full cylindrical tank is not possible. The non-uniform boundary conditions lead to more complex wave shapes and sloshing behavior [16].

Horizontal cylindrical tanks are commonly found in aircraft, missiles, and tanker vehicles [18]. They are oriented lengthwise with respect to the primary axis of the vehicle. The orientation introduces unique sloshing dynamics, particularly under the influence of gravity and longitudinal acceleration. Sloshing

in this geometry often couples with the pitch or roll motion of the vehicle, generating additional torques that can affect stability and control [16][22].

Spherical tanks are also often used in spacecraft and satellites [18] due to their optimal surface-area-to-volume ratio and uniform stress distribution, which enhances structural performance. These tanks are particularly effective for pressurized propellant storage. Sloshing modes in spherical tanks follow spherical harmonic functions and exhibit high symmetry. Despite this, the resulting fluid motion can induce complex torques interacting with the spacecraft's attitude dynamics [22].

Toroidal tanks have a doughnut-shaped geometry, allowing fluid to be stored in a ring-like structure around a central void. This configuration is advantageous in spin-stabilized spacecraft or systems where central space is needed for instruments or structural elements [18]. Although toroidal tanks are symmetric, the sloshing dynamics are complex and require advanced analytical approaches. The geometry minimizes center-of-mass shifts but can still generate significant lateral forces and torques [22][16].

2.1.5. Vertical Sloshing

So far only lateral sloshing was considered, however propellant tanks are also known to suffer from vertical sloshing. This happens when the tank is subjected to vibrations along the thrust or gravity-vector. Vertical excitation is equivalent to a time varying axial thrust acceleration so the Equation 2.3 has been rewritten for steady axial acceleration [16]. Full analytical results exist for this type of sloshing.

$$\frac{\partial \phi}{\partial z} + \left(a_z - X_0 \omega^2 \cos \omega t\right) \delta = 0$$

where X_0 is the amplitude of the vertical vibration, a_z is the vertical acceleration and ω is its frequency. The velocity potential is written as a series of normal slosh modes with integration constant denoted by the model amplitude A_m [16]. From this point the procedure is equal to the one shown in the section above.

2.1.6. Tank inclination

The effect of tank inclination on the sloshing frequency of liquids was investigated by Bugg [6]. Experiments where ran by tilting a tank between 0° and 60° relative to the vertical, and varying the liquid depth-to-radius ratio $\frac{d}{r}$. Two distinct oscillation modes were identified: one with the nodal line along the minor axis of the free surface, and another along the major axis. Results showed that increasing tilt decreased the frequency of the minor-axis mode significantly more than the major-axis mode. A notable result was that inclining the tank to 60° reduced the longitudinal slosh frequency by 27% However, it was concluded that for practical launch scenarios (tank tilt $\leq$ 10°), the effect on propellant dynamics was minimal [6][18].

2.2. Damping Effects

Damping for a sloshing of a liquid comes into effect in the form of energy dissipation that occurs at the walls and free surface of the tank due to viscous forces on boundary layers and internally due to viscous stresses. As the scale of the tank changes, so does the dominant dissipation method. For smaller tanks, boundary layer viscous effects are prevalent while for larger ones the internal viscous stresses become dominant [22].

When a liquid undergoes free oscillations in a stationary tank (i.e., with no external energy input), the wave amplitudes decay over time. This decay is quantified using the logarithmic decrement (Δ), defined as the natural logarithm of the ratio of successive peak amplitudes. The damping ratio (γ), another common metric, is related to Δ by $\gamma = \Delta/2\pi$, and represents the fraction of critical damping present[16].

In practical modeling, damping is typically included by first determining γ through experiments or separate analyses, then inserting this value into inviscid analytical solutions by analogy with linear spring-mass-damper systems. This approach avoids the complexity of re-solving the full fluid dynamics equations with viscosity and allows reasonable force and motion predictions even near resonance, where undamped models would predict unrealistic infinities.

2.2.1. Measuring Damping

Damping is generally determined experimentally through the use of scale models. CFD can also be utilized to compute damping but this method is computationally expensive and may less convenient than scale testing for complex tank geometries. The methods for experimentally determining the damping ratio are wave amplitude decay and force amplitude response.

Wave Amplitude Decay

The tank is oscillated at its resonant frequency until a steady state is reached, the input is then stopped and the rate of decay of the free surface displacement is monitored. The logarithmic decay of wave heights is then computed. This method only works for the fundamental mode as all other higher modes will quickly decay leaving only the fundamental.

Slosh force amplitude response

Either the force of wave amplitude is plotted against Ω or the half power bandwidth technique is utilized to compute the damping utilizing the relation:

$$\gamma_n = \frac{1}{2}\frac{\Delta\Omega}{\omega_n}$$

where $\Delta\Omega$ is the difference between the excitation frequencies at which the force or amplitude is equivalent to $\frac{1}{\sqrt{2}}$ times the maximum amplitude.

2.2.2. Damping in various tank shapes

Damping is not typically analytically calculated due to its complexity. Relations have been experimentally determined for the common tank shapes, all of the damping correlations pertain to the fundamental slosh mode [16]. As damping is only correlated to the viscous effects dimensionless analysis reveals that it is only a function of tank shape, fill level and the inverse of the Reynolds number:

$$Re_1 = \frac{\nu}{\sqrt{gL^3}} \quad \text{or} \quad Re_2 = \frac{\nu}{L^2\omega_n} \tag{2.6}$$

where ν is the kinematic viscosity of the liquid and L is a characteristic tank dimension, such as the diameter.

The first form of the Reynolds number, Re_1, shown in Equation 2.6, is commonly used in empirical correlations. It assumes a characteristic slosh velocity of $(gL)^{0.5}$, where g is the gravitational acceleration and L is the characteristic length. However, because g appears in the denominator, Re_1 is not suitable for applications in low-gravity environments where $g \approx 0$.

An alternative form, Re_2, uses the characteristic velocity $L\omega_n$, where ω_n is the natural sloshing frequency. This formulation is valid across a broader range of gravity conditions, including microgravity, and is therefore adopted in the slosh damping correlations for low-gravity. Sloshing relations have been developed for the following tank shapes:

- Circular cylindrical tank
- Cylindrical tank - spherical dome
- Spherical tank
- Oblate spheroidal tank
- Horizontal toroidal tanks

2.2.3. Baffles

Generally damping caused solely by viscous effects tends to be quite small, even at small scales, and it can therefore be said that sloshing motions are weakly naturally damped. Generally γ is equal or less than 0.01 for tanks with diameters of approximately 1 meter [22]. Therefore in order for attitude control systems to function properly and maintain stable flight, it is useful to increase γ, baffles fulfill this purpose. They serve to break up the wavefront dispersing the energy of sloshing and thus effectively lowering γ. Baffles has the disadvantage of adding dead mass to the tank system.

For circular tanks, series of ring baffles are often utilized attached to tank walls as seen in Figure 2.3. These baffles are most effective when placed near the free surface of the liquid and therefore spacing between baffles is sized so that the minimum damping exceeds the damping requirements regardless of tank fill level[16]. A ring baffle is a flat, annular structure typically mounted to the inner wall of a tank,

with its plane usually oriented perpendicular to the tank's axis. The outer edge of the ring is generally attached to the tank wall sometimes with a small clearance while the inner edge may include a lip for structural support. However, any feature that blunts the sharpness of this inner edge tends to reduce the baffle's effectiveness in damping sloshing. To reduce mass, baffles may be perforated, and further gains in damping and weight efficiency can be achieved by using flexible baffle designs[16].

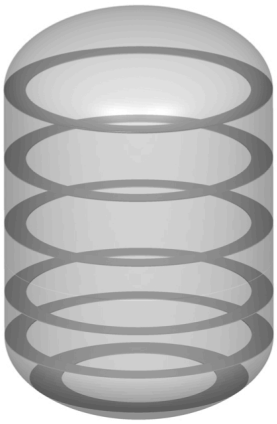

Figure 2.3: Example of baffles inside of a propellant tank to increase sloshing damping [34]

2.3. Modeling

Since integrating the analytical fluid dynamics equations into control systems coupled to spacecraft dynamics is too computationally expensive equivalent mechanical models have been developed[22]. The model regimes, assumptions along with complete linear and nonlinear models will be presented.

2.3.1. Model Regimes

In the modeling of liquid sloshing dynamics, different flow and modeling regimes can be defined. each with different assumptions underpinning the mathematical formulation. Three general regimes for modeling have been identified and presented from [22] and are shown in Figure 2.4.

- The first regime denoted by a as seen in Figure 2.4, is the linear regime. This is where the free surface is continuous and flat for small tank accelerations. The motions of linear sloshing can be replicated by another linear dynamic system. Such systems come in the form a pendulum or a mass spring system [16]. The small angle approximation $\sin\theta = \theta$ for asymmetric modes is used, simplifying the equations of motion describing the pendulum or spring mass systems. Damping, if included, is typically represented using linear viscous terms with small damping coefficients [16][22].
- The second mode, b in Figure 2.4 is characterized by relatively large amplitude oscillations in which in which the free liquid surface experiences a non-planar motion. This sloshing regime

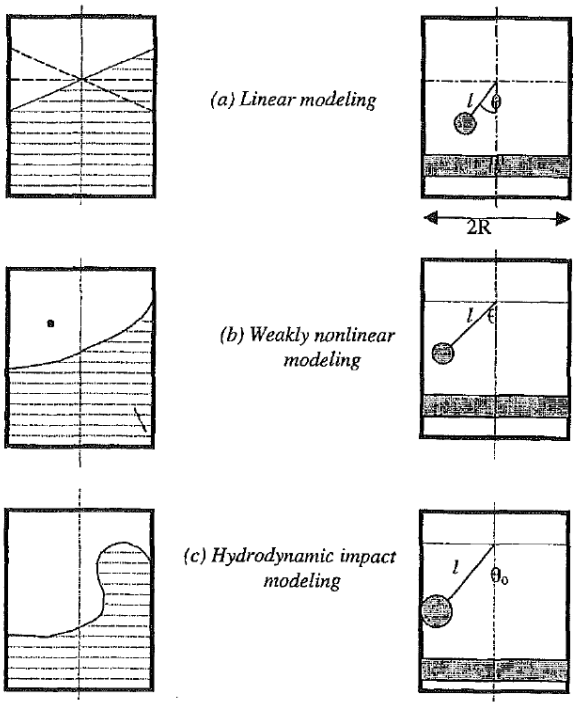

Figure 2.4: Different sloshing modeling regimes [22]

can be described by a differential equation where the nonlinearity is weak and can be analyzed utilizing standard perturbation techniques. To model non planar and rotational sloshing the simple pendulum has to be replaced by a compound pendulum [20]. The equivalent mechanical model is a pendulum describing relatively large motion such that $\sin\theta \approx \theta - \theta^3/3!$ [22].

- Strongly nonlinear motion (c) where the non-linearity is due to rapid velocity changes associated with hydrodynamic pressure impacts of liquid motion close to the free surface this is seen Figure 2.4 [22]. The velocity changes of free liquid surface are usually treated as being instantaneous given the strongly non-linear system behavior. Equivalent mechanical model is a pendulum impacting the tank walls [16].

If a liquid completely fills the rigid tank that it is contained by the entire system can be replaced by an equivalent rigid body. When the fill level of the tank decreases below 100% the resulting sloshing will have one or more natural modes that are not representable by a rigid body but will need to be represented by a mechanical model [36] [59].

2.3.2. Linear Models

The two prevalent linear models for sloshing are displayed in Figure 2.5. These are the pendulum model and the mass spring model, generally the pendulum model is preferred for in space applications due to the fact that the natural frequency is dependent on axial acceleration g, therefore closely following the behavior of a liquid. For a mass spring system the value of the spring constant K needs to be modified for changes in gravity (g) [22][16]. Transformation from one model to the other is done through the

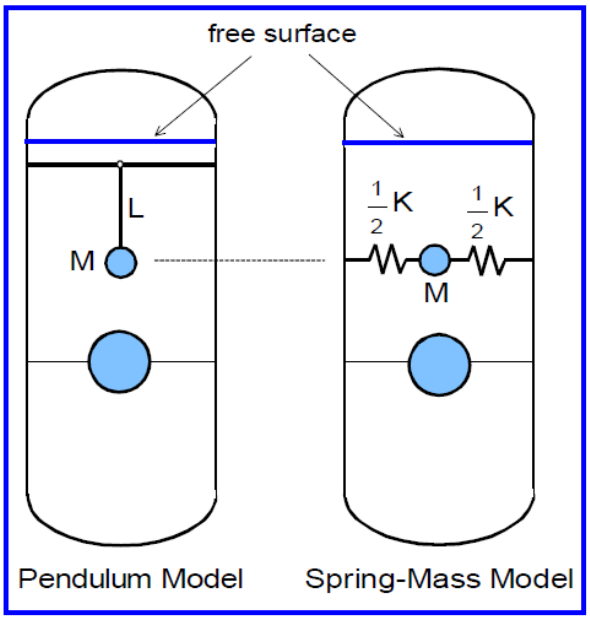

Figure 2.5: Pendulum and Spring mechanical models[16]

spring constant of $K = mg/L$ for the spring mass being at the same elevation as the pendulum mass. Damping is included in these models in the form of a linear dashpot for the spring mass model system and an angular dashpot for the pendulum model.

Equations of Motion

The equations of motion for the given mechanical system are based on a derivation given in [16]. This derivation is based off the spring model is is is simpler to derive than the pendulum model. The tank and fluid analogue utilized in this analysis is shown in Figure 2.6 and is independent to tank shape and fill level. Damping is initially neglected in this derivation for simplicity. Two spring mass systems are present in Figure 2.6, they represent the first and second sloshing modes. The derivation will be completed for a single mode, the fundamental mode, on an antisymmetric tank.

The model is split into two parts, there is the spring mass system that represents the proportion of the liquid actively participating in sloshing while the rest of the liquid is frozen. The spring masses are considered to not have any inertia, therefore only the fixed rigidly attached mass m_0 has inertia I_0. The CoM of the system is given by the checkered circle, all heights H_n are with reference to the CoM. The tank width is $2a$. Gravity g (or equivalent axial accelerations) axis along the vertical tank axis. The tank is exited by a small time varying linear displacement X_0 and angular rotation α_0 about an axis passing through the CoM. The deflection of the spring masses due to tank motion is represented by x_n.

To preserve liquid static properties, the sum of all the masses must be the same as the liquid mass m_{liq}, and the center of mass of the model must be at the same elevation as the liquid. These constraints are expressed analytically by Equation 2.7 and Equation 2.8.

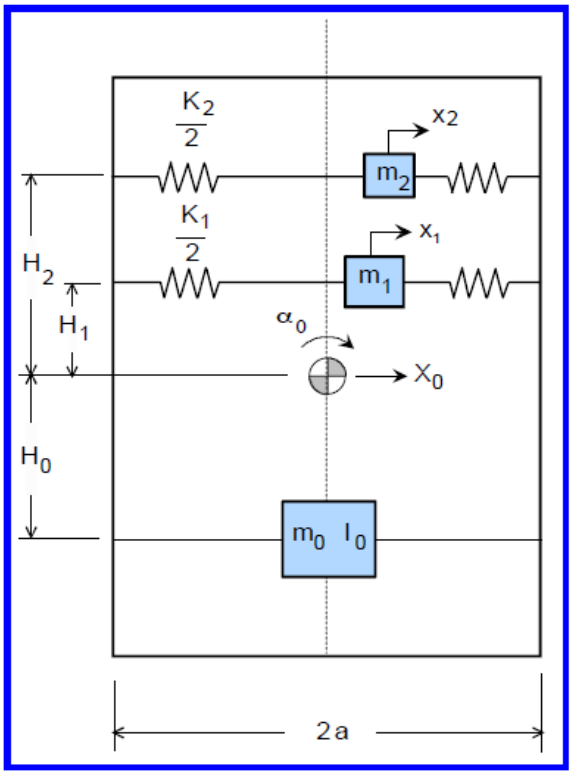

Figure 2.6: Spring Model for Derivations [16]

.

$$m_0 + \sum m_n = m_{\text{liq}} \tag{2.7}$$

$$m_0 H_0 + \sum m_n H_n = 0 \tag{2.8}$$

The model must also duplicate the sloshing forces, torques and natural frequencies: this can be done through the use of Equation 2.9, in which ω_n is the slosh natural frequency of nth mode.

$$\frac{K_n}{m_n} = \omega_n^2 \tag{2.9}$$

The net force exerted on the tank in the negative X_0 direction can be given by the reversed inertia forces of the moving masses, as shown in Equation 2.10. In this summation of forces and torques $\sin \alpha_0$ has been replaced by α_0 due to small amplitude assumption (making the system linear). Relation Equation 2.10 is reduced by substituting Equation 2.8 into it, yielding the simplified equation for net force Equation 2.11.

$$-F = m_0 \left(\ddot{X}_0 - H_0 \ddot{\alpha}_0 \right) + \sum m_n \left(\ddot{X}_0 + H_n \ddot{\alpha}_0 + \ddot{x}_n \right) \tag{2.10}$$

$$-F = m_0\ddot{X}_0 + \sum m_n\left(\ddot{X}_0 + \ddot{x}_n\right) \tag{2.11}$$

The net torque exerted on the tank is given by Equation 2.12. The final summation term is the torque caused by the offset of the spring masses from the centerline of the tank.

$$-M = \left(I_0 + m_0H_0\right)\ddot{\alpha}_0 + \sum m_nh_n\left(\ddot{x}_n + H_n\ddot{\alpha}_0\right) - g\sum m_nx_n \tag{2.12}$$

The overall equation of motion for each single spring mass system is then found as Equation 2.13

$$m_n\left(\ddot{X}_0 + \ddot{x}_n + H_n\ddot{\alpha}_0\right) + K_nx_n - m_ng\alpha_0 = 0 \tag{2.13}$$

Since the tank undergoes oscillatory translational motion along the x-axis and rotational pitching motion about the y-axis the components of this tank motion are given as $-X_0{}^{i\Omega t}$ and $-i\alpha_0{}^{i\Omega t}$. By including these into the equation of motion found in Equation 2.13, we yield Equation 2.14, where K_n has been eliminated be using relation Equation 2.9.

$$x_n = -\frac{i\Omega^2X_0}{\omega_n^2 - \Omega^2}\left(\frac{H_n + g/\Omega^2}{\omega_n^2 - \Omega^2}\right)i\Omega^2\alpha_0 \tag{2.14}$$

The forces and torques on the tank can be analytically expressed by Equation 2.15 and Equation 2.16.

$$\frac{F_{\text{amp}}}{i\Omega^2m_{\text{liq}}} = -\left[1 + \sum\frac{m_n}{m_{\text{liq}}}\left(\frac{\Omega^2}{\omega_n^2 - \Omega^2}\right)\right]X_0 - \alpha_0\sum\frac{m_n}{m_{\text{liq}}}\left(\frac{H_n\Omega^2 + g}{\omega_n^2 - \Omega^2}\right) \tag{2.15}$$

$$\begin{aligned}\frac{M_{\text{amp}}}{i\Omega^2} = -\alpha_0\left[I_0 + m_0H_0^2 + \sum m_nH_n^2 + m_{\text{liq}}\sum\frac{m_n}{m_{\text{liq}}}\left(\frac{H_n\Omega^2 + 2H_ng + gh^2/\omega_n^2}{\omega_n^2 - \Omega^2}\right)\right] \\ -m_{\text{liq}}X_0\sum\frac{m_n}{m_{\text{liq}}}\left(\frac{H_n\Omega^2 + g}{\omega_n^2 - \Omega^2}\right)\end{aligned} \tag{2.16}$$

If the tank is not antisymmetric, the sloshing mode will depend on the direction of the tank acceleration, therefore there exists a set of modes for each separate axis, which need to be modeled separately. These modes need to be summed up and decomposed based on the angular acceleration. For tanks with multiple modes (such as a rectangular tank having modes in x and y axis) the participating mass of each mode will be equivalent to the total liquid mass. However, the total sum of liquid actively participating in sloshing means will never be larger than the total mass of liquid present in the tank [22][16]., due to conservation of mass. If each mode has liquid mass m_{liq} then x and y modes (in rectangular tank) cannot be active at once since the liquid mass would be $2m_{liq}$, instead each mode may at most have $0.5m_{liq}$ active simultaneously.

The model parameters, mass, height, placement location, rigidly attached mass are independent of the amplitude or frequency of simple harmonic excitation of the tank. Dependency on spring constant or

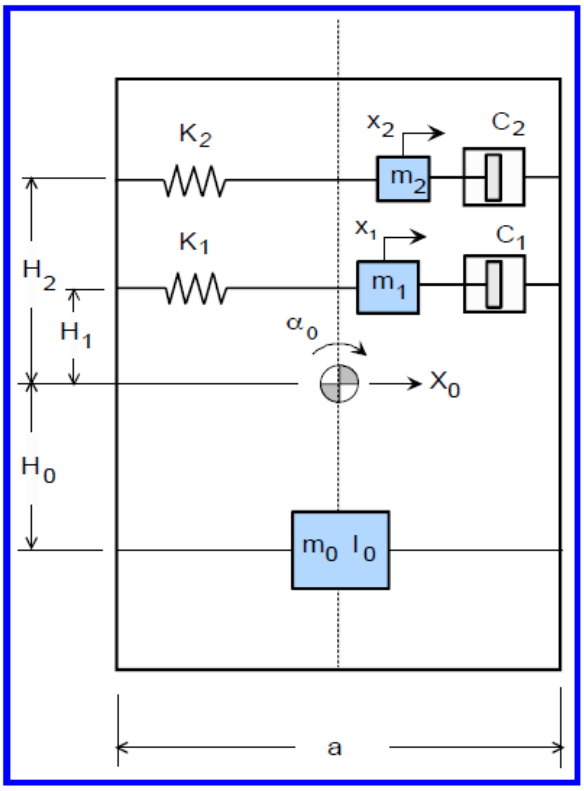

Figure 2.7: Spring Mass system model with dashpot [16]

gravitational acceleration g can be eliminated by switching from spring mass to pendulum. This is done by locating the pendulum hinge point for each slosh mass m_n at elevation $L_n + H_n$ where $L_n = \sqrt{\frac{g}{\omega_n}}$ is pendulum length [16]. Both the spring mass and pendulum models capture the same linear sloshing behavior, for space applications the pendulum model is preferred due to it adapting to different levels of g while the mass spring system is used for Earth bases sloshing as g can normally be assumed constant.

The model parameters have been developed in a similar fashion for rectangular and axisymmetric cylindrical and spherical tanks, these can be found directly in the Dodge book [16] where a computer program called SLOSH has been develop to quickly obtain the model parameters of analog mechanical models.

Damping inclusion

Damping can be introduced into mechanical models using linear viscous forces, which are valid approximations when the damping coefficient γ is small. This assumption is realistic, as damping coefficients (even in the presence of baffles) typically fall within the range of 0.01 to 0.05 [16]. In mechanical terms, linear damping is modeled using a dashpot: a piston moving through a viscous fluid. This element is added in series with the mass, as illustrated in Figure 2.7. In a spring-mass system, the dashpot exerts a force proportional to the linear velocity, whereas in a pendulum system, it behaves as an angular dashpot, opposing the angular velocity.

Damping can also be naturally included in the Equation of Motion (EoM) as previously derived and is

presented in Equation 2.17. For this equation $\gamma_n = \frac{C_n}{2m_n\omega_n}$ which is the damping coefficient of the n$^{\text{th}}$ mode and C_n is the value of the dashpot coefficient.

$$m_n\left(\ddot{X}_0 + \ddot{x}_n + H_n\ddot{\alpha}_0\right) + 2\gamma_n m_n\omega_n\dot{x}_n + K_n x_n - m_n g\alpha_0 = 0 \tag{2.17}$$

Replicating the analysis previously carried out to obtain the expressions for force and torque including damping yields, Equation 2.18 and Equation 2.19. Experimental results comparing cylindrical tanks to equivalent mechanical models have shown good agreement with theory for the fundamental mode n=1 [1]. However, validating higher-order modes experimentally proves to be far more challenging. In particular, measuring the damping coefficient γ_2 is difficult because higher modes decay much faster than the first. As a result, when applying the wave amplitude decay method to determine damping, the contribution of these higher modes persists only briefly, making accurate measurement unreliable [16].

$$\frac{F_{\text{amp}}}{i\Omega^2 m_{\text{liq}}} = -X_0\left[1 + \sum\frac{m_n}{m_{\text{liq}}}\left(\frac{\Omega^2}{\omega_n^2 - \Omega^2 + 2i\gamma_n\omega_n\Omega}\right)\right] - \alpha_0\sum\frac{m_n}{m_{\text{liq}}}\left(\frac{H_n\Omega^2 + g}{\omega_n^2 - \Omega^2 + 2i\gamma_n\omega_n\Omega}\right) \tag{2.18}$$

$$\begin{aligned}\frac{M_{\text{amp}}}{i\Omega^2} = &-\alpha_0\left[I_0 + m_0H_0^2 + \sum m_nH_n^2 + m_{\text{liq}}\sum\frac{m_n}{m_{\text{liq}}}\left(\frac{H_n^2\Omega^2 + 2H_ng + gh^2/\omega_n^2}{\omega_n^2 - \Omega^2 + 2i\gamma_n\omega_n\Omega}\right)\right] \\ &- m_{\text{liq}}X_0\sum\frac{m_n}{m_{\text{liq}}}\left(\frac{H_n\Omega^2 + g}{\omega_n^2 - \Omega^2 + 2i\gamma_n\omega_n\Omega}\right)\end{aligned} \tag{2.19}$$

2.3.3. Nonlinear Models

The key assumption behind analytical derivations and the equivalent mechanical models so far have been that wave amplitudes are small, this allows the use of linear relations to model damping. However these relation do not hold when modeling a sloshing fluid that is in either regime b or c from Figure 2.4, for those situations specialized models are needed. The nonlinearities treated in the third regime (c) are highly complex, thus modeling approaches favor CFD, as a result limited literature exits regarding the full derivations. Therefore description efforts will remain for the second regime b with slight nonlinearities focusing on the conical pendulum.

The conical pendulums is a pendulum that is free to swing in any plane. An example of such a model and its instabilities is seen in Figure 2.8. This system consists of a conical pendulum subjected to harmonic excitation, with its angular motion described relative to the x, y, and z axes. As in other pendulum-based sloshing models, the pendulum length L is chosen such that its natural frequency matches that of the first sloshing mode. The excitation is applied along the y-axis with an amplitude ϵ, which is scaled relative to the pendulum length L. Due to the excitation direction, stable motion occurs in the y-z plane, where $\beta = 0$ and $\alpha = \gamma$. To enable linearization of the equations of motion, small-angle approximations are employed: $\sin\alpha \approx \alpha - \frac{\alpha^3}{3!}$ and $\cos\alpha \approx 1 - \frac{\alpha^2}{2}$ [16][20].

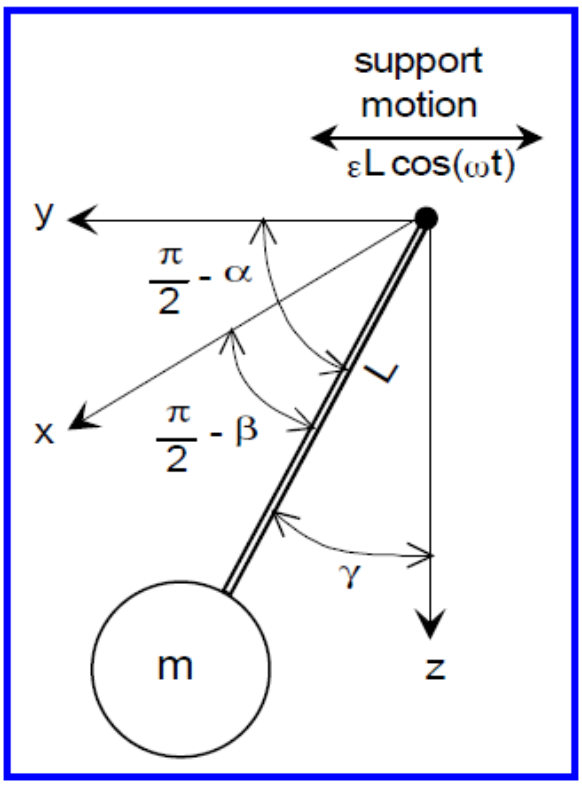

Figure 2.8: Conical Pendulum used for rotary sloshing [16]

The planar angular displacements of α and β of a mass m swinging in x and y axes are given by the nonlinear coupled differential Equation 2.20. In these equations, the angle γ has been eliminated in these equations by using trigonometric relations.

$$\begin{aligned}\left(\frac{d^2}{dt^2}+\frac{g}{L}\right)\alpha-\frac{g}{6L}\alpha^3+\frac{1}{2}\left(\frac{d^2}{dt^2}+\frac{g}{L}\right)\alpha\beta^2&=\epsilon\omega^2\cos\omega t\\ \left(\frac{d^2}{dt^2}+\frac{g}{L}\right)\beta-\frac{g}{6L}\beta^3+\frac{1}{2}\left(\frac{d^2}{dt^2}+\frac{g}{L}\right)\beta\alpha^2&=0\end{aligned} \tag{2.20}$$

The angle γ is eliminated in Equation 2.20 by applying the trigonometric identity $\sin^2\gamma = \sin^2\alpha + \sin^2\beta$. this simplification allows for the identification of two primary types of motion. The first corresponds to planar nonlinear oscillation, characterized by the condition $\beta = 0$. The second is a rotary motion in which the pendulum exhibits continuous rotation around the z-axis. The stability of these solutions depends on both the amplitude of motion and the angular configuration of the system[20].

To assess the stability, small perturbations are introduced into the equations of motion. If these perturbations grow over time, the motion is deemed unstable; if they decay, the motion is considered stable [16]. This behavior is effectively captured by introducing the dimensionless frequency parameter

$$\mu = \epsilon^{-2/3}\left[\frac{\omega^2-\omega_1^2}{\omega_1^2}\right].$$

While the lower frequency boundary derived using this method aligns well with experimental results, the upper frequency limit for rotary sloshing demonstrates significant discrepancies when compared to physical observations[20][22]. This effect was treated in a paper titled Modeling and Simulation of Rotary Sloshing in Launch Vehicles, written by Jeb S. Orr in 2021 describing and comparing different models used for the simulation of rotary sloshing within the context of a spin stabilized launch vehicle [37].

Initially the author critiques linear mechanical analogues (normal pendulums) as they suffer from two main issues; the first being that near resonance they do not adequately capture the behavior of the liquid and secondly that they miss important coupling between the degrees of freedom of lateral sloshing modes [37]. As explained the most popular nonlinear model is a conical pendulum

which can predict the formation of stable rotary fluid cycles when the tank is exposed to a sinusoidal lateral excitation. Experimentally, four fundamental response regions have been identified [37] and reported below:

- Stable, in plane motion or unstable high amplitude motion below the resonant frequency
- chaotic motion near resonance
- rotary motion in a narrow band just above resonance
- stable rotary or planar motion above resonance

The conical pendulum model exhibits the correct nonlinear phenomena of stiffening, softening and jump resonance. The resonant frequency of the sloshing fluid is not longer independent of amplitude but changes with increasing input amplitude [16][21]. When comparing with fluid test data (from Hutton [21] the rotary dynamics of the pendulum did not exhibit the proper amplitude ratio at frequencies above resonance. Therefore a modified mechanical model including a variable nonlinear spring is tested to refine the model [5]. This is called the Bauer nonlinear model first theorized in 1966 [5].

The comparison of the conical pendulum and Bauer are seen in Figure 2.9, the y-axis represents the wave height X_w and the x-axis, η representing the natural frequency ratio. This comparison was only done for the first mode. The Bauer model clearly matching the experimental data collected by [21] better than the pendulum above resonance for the case when rotary sloshing does occur [37]. These are important results, if after resonance the sloshing liquid enters into a rotary cycle limit then the conical pendulum does not accurately predict the wave height (and therefore force imparted to the tank).

Finally a Monte Carlo analysis was conducted using a high fidelity launch vehicle simulation with the aim to asses the likelihood of rotary sloshing development in a typical liquid rocket configuration. Since as previously, describes a linear pendulum would miss this motion the aim was to find out if an updated model would be useful to implement in launch vehicles. The result was that in a small number of cases a stable lightly damped rotary sloshing mode occurred producing a disturbance torque not predicted by the purely linear model [37]. Therefore, it has been suggested by the author that careful use of advanced,

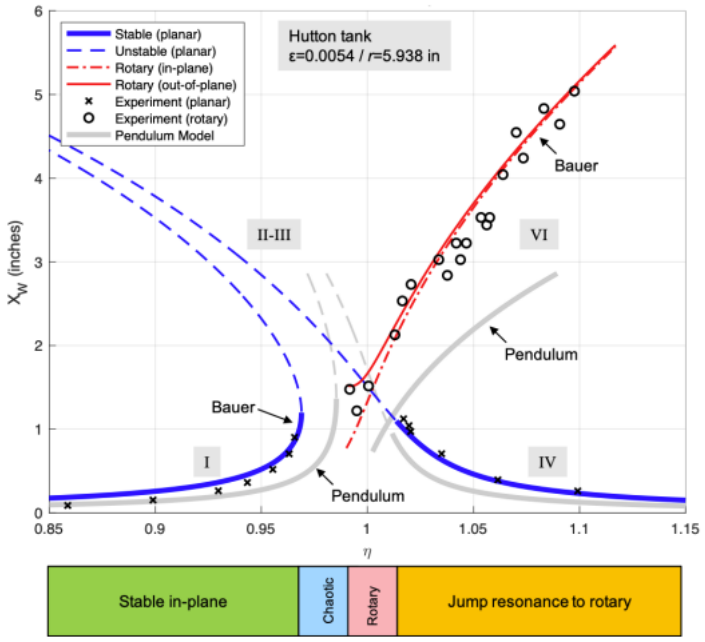

Figure 2.9: Comparison of spherical pendulum, Bauer model with experimental data collected from [58] [37]

test-correlated nonlinear models such as an improved Bauer model should be considered in the flight certification process. This serves as important motivation and a starting point in the investigation of rotary sloshing owing to its relevance when considering launch vehicles.

2.3.4. Coupled Nonlinear Fluid-Spacecraft Models

Lee D. Peterson (1989) presents an analytical and experimental investigation into the interactions between a nonlinear fluid model and a linear model of spacecraft dynamics. The motivation stems from the observation that linear slosh models fail to capture critical nonlinear behaviors, especially near resonance or during large-amplitude motions. During specific spacecraft maneuvers, such as attitude control, slosh motion in onboard fuel tanks can interact nonlinearly with the spacecraft dynamics, potentially inducing undesired oscillations or instabilities [38].

To analyze the coupled dynamics, a conical pendulum is employed as an approximation of the sloshing fluid inside a partially filled cylindrical tank, while the spacecraft is modeled as a rigid body capable of rotational motion about a principal axis [38]. These assumptions lead to a lumped parameter representation of the system, whose nonlinear equations of motion are derived using Lagrangian mechanics. The total kinetic and potential energy of the coupled spacecraft-fluid system is calculated, yielding a model with three degrees of freedom (DoF): the spacecraft body angle, and the two angular displacements of the slosh pendulum, θ and φ [38].

Numerical integration of the resulting equations provides time-domain responses across various scenarios, including changes in initial conditions, slosh-to-spacecraft mass ratios, frequency ratios, and Bond numbers. Key dynamic variables, such as spacecraft angular displacement, sloshing mass trajectories,

and energy transfer between the spacecraft and fluid, are tracked throughout the simulations [38].

An important methodological detail involves the manipulation of Bond numbers both through varying tank geometries and by adjusting fluid viscosity using additive elements. While Bond numbers below 20–30 were unobservable under 1g conditions due to excessive damping, low-Bond regimes were explored via parabolic flight campaigns using a KC-135 aircraft [38].

The results indicate that nonlinear slosh dynamics cannot be simply superimposed onto a linear structural model of the spacecraft to accurately predict the behavior of the coupled system. A nonlinear subsystem embedded within an otherwise linear dynamic structure may exhibit fundamentally different behavior than when analyzed in isolation [38]. Consequently, only a fully coupled model can yield accurate predictions of spacecraft motions arising from sloshing forces—whether in high- or low-gravity environments.

Moreover, these findings emphasize the need to retain higher fluid modes and incorporate capillary effects when modeling spacecraft-fluid interactions, particularly at low Bond numbers. Linear models or uncoupled nonlinear models may significantly mischaracterize system responses under strong coupling. This insight carries important implications for spacecraft attitude control system design. For instance, a coupled nonlinear model might reveal a 10% eigenfrequency shift due to fluid-structure interaction, which must be addressed as a model uncertainty in linear controller design to ensure robust stability and performance [38].

2.3.5. Linear to Nonlinear transition

In this section a brief presentation of what factors regarding slosh excitation lead to linear or nonlinear sloshing. The results presented here are for sloshing in nominal Earth gravity conditions, not low gravity.

Relative Slosh wave amplitude

Sloshing will remain approximately linear if the free-surface wave height does not greatly deviate from the liquid depth or tank dimension. Literature suggests for cylindrical tanks keeping the peak wave amplitude between 15% of the tank radius [16][53], this is known as small amplitude slosh. For sloshing amplitudes greater than 25% of the radius nonlinear effects such as surface steepening and possible wave breaking may [53]. During the transition period between these two amplitude oscillations the liquid exhibits a transitory behavior [53]. This method can serve as a verification of linear sloshing taking place in a tank.

Excitation Amplitude

While there is no single consensus reading what constitutes as a small external excitation there are indications from [16] that the linear lateral excitation of a tank should be no larger than the linear peak wave amplitude. This indication connected to the previously presented information suggests that linear displacements below 15% of the tank radius result in linear sloshing. If the linear displacements surpass

25% of the tank radius then the resulting sloshing is nonlinear [16][22].

2.4. CFD

Computational Fluid Dynamics (CFD) is a discipline within fluid mechanics that uses numerical methods and algorithms to simulate and analyze fluid flow problems [7]. In a typical CFD approach, the continuous fluid domain is discretized into a finite set of control volumes or elements, and the governing equations of fluid motion (the Navier–Stokes equations or simplifications thereof) are solved approximately on this grid. Modern CFD software allow to compute the evolution of fluid properties (velocity, pressure, and density) over time and space by iteratively solving these equations under defined boundary conditions [7]. With sufficient computational power, CFD can provide detailed insight into complex flow phenomena that would be difficult or impossible to obtain analytically or through simple correlations [56]. CFD techniques are employed across many fields of engineering due to their ability to numerically predict fluid behavior with high fidelity.

CFD is a useful tool for simulating sloshing, the motion of liquid and gas phases inside the tank is computed by solving the Navier–Stokes equations with appropriate multiphase flow models [9] [16]. A common approach for sloshing problems is the Volume of Fluid (VOF) method or similar interface-capturing techniques, which track the liquid free-surface within each computational cell [9]. For example, open-source CFD solvers like OpenFOAM implement dedicated two-phase flow solvers that handle an incompressible liquid and gas with a free surface, allowing for tank motion either by moving the mesh or by adding equivalent acceleration forces to the fluid [9]. Using such methods, CFD can simulate how the liquid surface oscillates, deforms, or even breaks into droplets under external excitations. Turbulence models can be included to capture turbulent mixing during violent sloshing, and fluid viscosity and surface tension [56] can be accounted for making CFD a useful tool for studying sloshing mechanics in low gravity conditions. CFD has been used in missions such as SPICEsat mission which used FLOW-3D software as a primary modeling tool for sloshing in its tanks [24].

The outcome of a CFD sloshing analysis typically includes time histories of the fluid free-surface shape, pressure distribution on the walls, and resultant forces/torques on the container. These detailed results make it possible to identify critical effects like impact pressures on tank roofs or walls, and to measure energy dissipation/damping due to fluid viscosity or baffles [56] [9]. Thus, CFD is especially useful in sloshing research as it enables a physics-based, high-fidelity simulation of the fluid motion, providing insights into nonlinear slosh behavior that simpler models would miss.

2.5. Hydrodynamic regimes

For the purposes of this thesis we are not only interested in modeling high gravity but also low gravity sloshing. This type of slosh generally intended as the slosh occurring in satellites that are still are subjected to the gravity field of Earth. Truly 0g deep space slosh is extremely difficult to model and requires extensive CFD simulations [26]. The motions of liquid-gas systems can be influenced by

capillary, body (gravity), inertia and viscous forces [26][16]. It is useful to be able to isolate the most prominent effect to reduce them for the sake of a simpler analysis. Thankfully, fluid dynamics studies have yielded dimensionless numbers separating hydrodynamic behaviors in different regimes.

The relative importance of inertial and capillary forces is given by the Weber number (We) seen in Equation 2.21. L is the characteristic length of a system, V is the characteristic velocity and σ is the surface tension. If We » 1, then inertia forces are dominant [16], this will mean that the liquid will behave more similarly to a ”ball” with inertia within the fuel tank.

$$\text{We} = \frac{\text{inertia}}{\text{capillary}} = \frac{\rho V^2 L}{\sigma} \tag{2.21}$$

$$\text{Bo} = \frac{\text{gravity}}{capillary} = \frac{\rho g L^2}{\sigma} \tag{2.22}$$

The Bond number, shown in Equation 2.22 is the ratio of gravitational to capillary forces. It determines weather the major force on the liquid is gravity. Typically for space applications, there are three broad regimes (of Bond numbers) considered in sloshing literature [26][22], however, these are not strictly defined regimes:

- **High G Slosh (Bo>1000)**: This is the regime typically experienced on Earth and in large scale propellant tanks. The angle with the surface is $\theta = 90$ and there exist extensive analytical models for common geometries along with test correlated models (spring and pendulum). There is very good agreement with linear and some weakly nonlinear motions (such as slow rotary slosh)[26].
- **Low-G Slosh (30<Bo<1000)** In this regime mechanical models representing linear motions require corrections, the purely inviscid models suffer from inaccuracies. Hybrid models are needed (compound pendulum). The surface of fluid interface is no longer 90 degrees but is seen as being more curved, wetting behavior begins to occur. Mode behavior is similar to higher bode numbers but shifts are observed in modal frequency and damping[26][16].
- **Microgravity Slosh (Bo< 30)** This regime is highly nonlinear, analytical solutions are typically unavailable and CFD needs to be utilized to describe propellant settling. This regime is on the interface with capillary and inertia dominated (smaller scales capillary, larger scales inertia) [26]. Practically for fuel tanks it becomes difficult predicting where the propellant is within the tank.

The relative importance of inertia and gravity forces is indicated by the Froude number show in Equation 2.23. When Fr $>>$ 1, inertia forces are dominant compared to gravity. The Froude number is also equal to the ratio Fr $= \frac{\text{We}}{\text{Bo}}$. These boundaries between these individual flow regimes are shown in Figure 2.10. Capillary regime (Bo $<<$ 1) is when the surface tension is the dominant force, this happens typically in liquid interfaces confined to narrow geometries (think straws) or for space applications propellant management devices which rely on surface tensions forces to move propellant. Within the capillary regime, the contact angle between a fluid and a surface is key in determining how it will

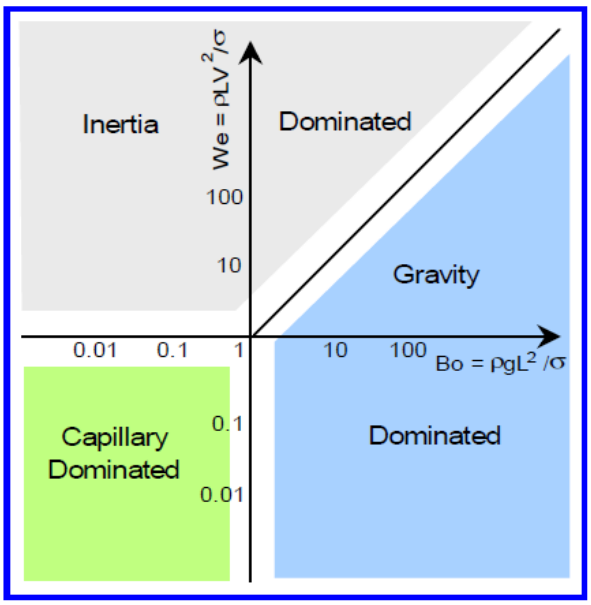

Figure 2.10: Hydrodynamic Regimes [16]

move. Inside a fuel tank capillary forces will manifest themselves in the form of the propellant wetting the inner walls of the tank and not clumping up in a ball.

$$\text{Fr} = \frac{\text{inertia}}{\text{gravity}} = \frac{V^2}{gL} \tag{2.23}$$

Regardless of the dominant hydrodynamic force be it inertial, gravitational or capillary, viscous forces remain, and need to be accounted for separately through the use of the Reynolds number, shown in Equation 2.24 where ρ is the fluid density, V is the characteristic velocity, L is the characteristic length and μ is the dynamic viscosity of the fluid.

$$\text{Re} = \frac{\rho V L}{\mu} \tag{2.24}$$

Additional bond numbers

Modifications to Bond numbers exist to better describe fluid in low g conditions. These additional Bond numbers are reported in [12] and can be found below:

- Bo_i = Inertial Bond Number, presented in Equation 2.25
- Bo_c = Centrifugal Bond Number, presented in Equation 2.26
- Bo_t = Translational Bond Number, presented in Equation 2.27

The Bo_i and Bo_c are used to characterize low-g sloshing in rotational motion which, as previously stated, is weakly nonlinear. The centrifugal bond number is found in [16]. A separate mechanical representation known as a ”ball model” is presented in [12]. Whereas the Bo_t is utilized during linear

acceleration, where the classical mass-spring and pendulum models can be utilized. Dr. Jens Levenhagen of Airbus Defense and space, who partially developed the ball model has been contacted to obtain additional information, however this request went unanswered.

$$Bo_i = \frac{\rho \cdot R_{\text{Tank}}^2 \cdot L \cdot \dot{\omega}}{\sigma} \tag{2.25}$$

$$Bo_c = \frac{\rho \cdot R_{\text{Tank}}^2 \cdot L \cdot \omega^2}{\sigma} \tag{2.26}$$

$$Bo_t = \frac{\rho \cdot R_{\text{Tank}}^2 \cdot a}{\sigma} \tag{2.27}$$

Notes on low-g rotational slosh

The maneuver types for low-g rotational slosh are large angle slews such as rest to rest slews, typical for science missions and by non-rest to non-rest slews which are typical for agile earth observation missions [26]. The agility of different types of AOCS actuators is defined by their rate and accelerations this is reported in Equation 7.2.2 taken from [26].

Fuel sloshing may also be exited depending on:

- Large angle skew profiles
- Applied acceleration rates (jerk)
- Tank position relative to Centre of Mass (CoM)
- Tank Fill Ratio

Agility Domain	**Rate [rad/s]**	**Acceleration [rad/s^2]**	**Preferred AOCS Actuators**
Low Agility	$< 2 \cdot 10^{-3}$	$< 5 \cdot 10^{-5}$	Magnetorquers, Reaction Wheels
Medium Agility	$2 \cdot 10^{-3}$ – $2 \cdot 10^{-2}$	$5 \cdot 10^{-5}$ – $5 \cdot 10^{-4}$	Reaction Wheels, Chemical Propulsion
High Agility	$> 2 \cdot 10^{-2}$	$> 5 \cdot 10^{-4}$	Control Moment Gyros, Chemical Propulsion

Table 2.2: Agility domains and corresponding rate, acceleration, and actuator recommendations for AOCS systems [26].

From [26] Figure 2.11 has been taken which classifies different missions based on the rates and accelerations experienced. Control Moment Gyroscope (CMG) stands for control moment gyro and Reaction Wheel (RW) stands for reaction wheel.

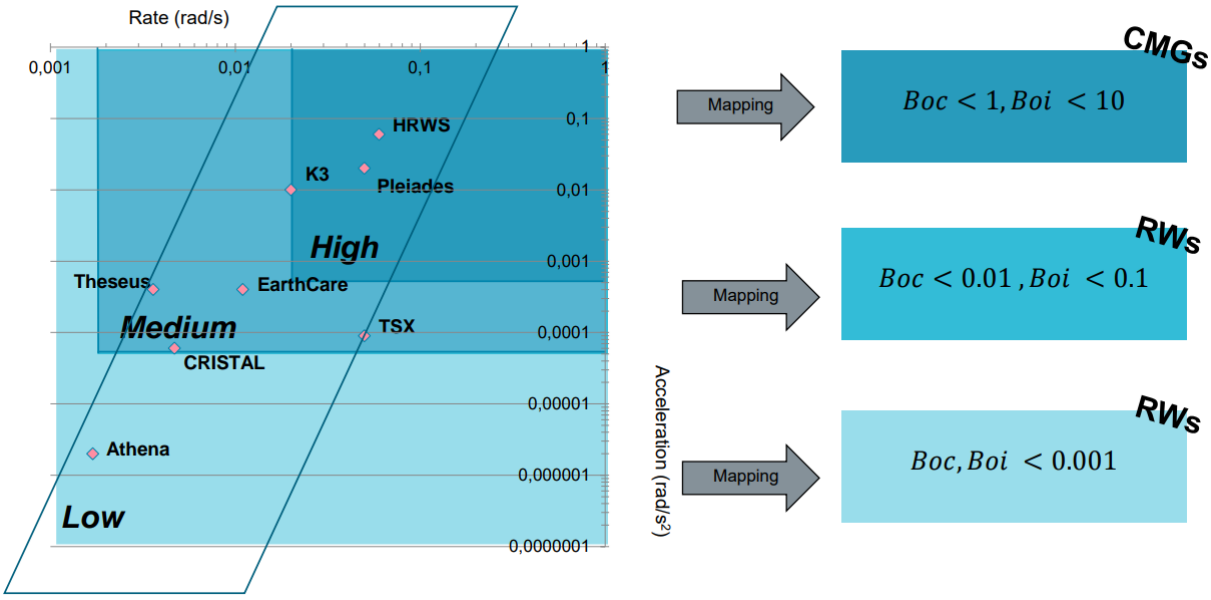

Figure 2.11: Spacecraft classification of sloshing and connection with Bond numbers [26]

Response time estimations

The system exhibits different dynamic responses depending on the hydrodynamic regime, with the natural slosh frequency ω_n varying accordingly: it is given by Equation 2.28 under high-g (gravity-dominated) conditions, and by Equation 2.29 in low-g (capillary-dominated) environments [16].

$$T = \sqrt{\frac{L}{g}} \text{gravity dominated regime} \tag{2.28}$$

$$T = \sqrt{\frac{\rho L^3}{\sigma}} \text{capillary dominated regime} \tag{2.29}$$

2.6. Scaling

Most of the literature relating to scaling relations for low-G slosh frequency and damping all point back to one single paper: ”Simulation and Scaling of Low-Gravity Slosh Frequencies and Damping” written by Clark, L. V., and Stephens, D. G. in September 1967 [10]. This source has thus far not been found online and an email has been sent to NASA archive team but no response has been received. In general the literature relating to scaling of sloshing phenomenon in low g is very scarce so literature relating to scaling of sloshing in all gravity conditions has been reported.

2.6.1. Bond Number Equivalency

A source produced after this main paper, directly citing it called: ”Simulated low-gravity sloshing in spherical tanks and cylindrical tanks with inverted ellipsoidal bottoms” [15] was investigated. From this paper it was reported that successful simulation of low Bond numbers (10 < Bo < 100) was done utilizing

small diameter tanks in earth gravity. By examining the Bond number (Equation 2.22), it becomes evident that sloshing behavior in different gravitational environments can be related through geometric scaling. Specifically, a small tank operating under Earth's gravity can have the same Bond number as a larger tank in microgravity, provided the ratio of gravitational to surface tension forces remains constant. This equivalence implies that when the Bond number is preserved, the relative influence of surface tension and gravity is maintained. As a result, small-scale sloshing experiments conducted on Earth can effectively replicate some aspects of fluid behavior expected in large space-bound tanks, offering a practical means of simulating microgravity conditions in terrestrial laboratories [15]. When changing scales the viscous forces of the sloshing liquid are highly dependent on the Reynolds number [18], therefore, it is important to verify Reynolds number equivalency at different scales when planning experiments. This approach was used in [37] in order to simulate different Bond numbers.

It was experimentally noted that the scaling of natural frequency was dependent on the tank shapes, as spherical tanks and cylindrical tanks exhibit different characteristics [15]. This will need to be taken into account when deciding what type of tank shape to utilize for experiments.

2.6.2. Froude Scaling

Froude scaling is a technique used in hydrodynamic model testing to ensure dynamic similarity between a physical model and its full-scale counterpart when gravitational and inertial forces dominate. Froude scaling us used mainly in marine systems involving sloshing, wave impacts and ship hydrodynamics, most sources treated Froude scaling in the context of shipping Liquefied Natural Gas (LNG) industry.

Froude scaling is based on two important factors geometrical and dynamic similarity between scale model and full system[44]. Geometric similarity is guaranteed by ensured that linear dimensions between the full size (F) and the scale model (M) have the same shape and must have the same scale ratio denoted by Equation 2.30 [44].

$$\lambda = \frac{L_F}{L_M} \tag{2.30}$$

Dynamic similarity is ensured by having ratios between different forces in full scale being the same in the model scale. For this the forces of interest are: Inertia Forces F_i, Viscous Forces F_v, Gravitational Forces F_g, Pressure Forces F_p, Elastic forces in fluid F_e and Surface Forces F_s[44].

These translate to well known ratios that where introduced in the previous section. Froude number; ratio between inertia and gravity, Reynolds number; ratio between inertia and viscous forces and Weber number; ratio between inertia and surface tension forces [44]. If the Froude numbers are equivalent similarity can be established via models between model (M) and full scale (F) as shown in Equation 2.31 and the gravity forces will be scaled correctly. Since surface waves (in most high g sloshing applications)

are gravity driven this will ensure that wave forces scale correctly.

$$Fr_M = Fr_F \quad \Rightarrow \quad \frac{U_M}{\sqrt{gL_M}} = \frac{U_F}{\sqrt{gL_F}} \tag{2.31}$$

Through the use of Froude equivalency several scaling relations can be found, Equation 2.32 demonstrates how the scaling relation for velocity is found. Table 2.3 reports the scaling factors for different important model parameters.

$$U_M = U_F \cdot \sqrt{\frac{L_M}{L_F}} = U_F \cdot \sqrt{\frac{1}{\lambda}} \quad \text{where } \lambda = \frac{L_F}{L_M} \tag{2.32}$$

Physical Parameter	**Unit**	**Multiplication factor**
Length	[m]	λ
Structural mass	[kg]	$\lambda^3 \cdot \rho_F/\rho_M$
Force	[N]	$\lambda^3 \cdot \rho_F/\rho_M$
Moment	[Nm]	$\lambda^4 \cdot \rho_F/\rho_M$
Acceleration	[m/s^2]	$a_F = a_M$
Time	[s]	$\sqrt{\lambda}$
Pressure	[Pa = N/m^2]	$\lambda \cdot \rho_F/\rho_M$

Table 2.3: Froude scaling multiplication factors for various physical parameters [44].

A notable limitation is that Froude scaling does not preserve compressibility effect such as gas liquid impacts (air entrapment during sloshing) [14]. Partial corrections for compressibility have been found in during the Sloshel project [13]. Furthermore, at small test scales surface tension and viscosity become disproportionately influential (low Bond number) violating the dynamic similarity between systems [23].

Froude scaling applied to a missile

A paper named ”Simulation of Fuel Sloshing Characteristics in Missile Tanks by Use of Small Models” [2] made use of Froude Scaling in the context of antisymmetric sloshing of fuel in a missile exited by translational or rotational accelerations. The study makes use of the small excitation assumption, rigid tank and existence of geometric similarity between model and full scale tank. It is assumed that surface tension forces are small compared with the inertial and viscous forces, and consequently any additional consideration of surface tension is omitted.

The relevant parameters where taken as:

$$
\begin{aligned}
a &= \text{longitudinal acceleration on tank, } LT^{-2} \\
d &= \text{tank diameter, } L \\
F &= \text{resultant liquid force on tank wall, } MLT^{-2} \\
h &= \text{depth of liquid in tank, } L \\
X_0 &= \text{excitation amplitude, } L \\
\mu &= \text{liquid viscosity, } ML^{-1}T^{-1} \\
\rho &= \text{liquid density, } ML^{-3} \\
\tau &= \text{excitation period, } T
\end{aligned}
$$

An equation relating these eight parameters analytically can be written in the general form seen in Equation 2.33 according to the Buckingham Pi theorem[2].

$$\varphi'(\pi_1, \pi_2, \pi_3, \ldots, \pi_{n-m}) = 0 \tag{2.33}$$

where

$$
\begin{aligned}
n &= \text{number of physical parameters involved} \\
m &= \text{number of fundamental dimensions (in this case } n - m = 8 - 3 = 5)
\end{aligned}
$$

The π's are dimensionless combinations of the parameters listed. Similitude theory yields expressions for the various dimensionless groups. The general solution of the form of Equation 2.33 may then be written in terms of the π's as Equation 2.34 [2].

$$\frac{F}{\rho d^3(d/\tau^2)} = \varphi\left(\frac{a\tau^2}{d}, \frac{h}{d}, \frac{X_0}{d}, \frac{\rho d(d/\tau)}{\mu}\right) \tag{2.34}$$

We note that all linear dimensions are scaled in the same ratio as the diameter, that the group $a\tau^2/d$ is equivalent to Froude's number, and that the group $\rho d(d/\tau)/\mu$ is equivalent to Reynolds' number. The excitation in displacement can be substituted for force P or acceleration with the appropriate group becoming $P/[(\rho d^3)(d/\tau^2)]$

For rotational excitement the general parameters remain the same but the excitation is decomposed in the angular rotation θ_0 and the location of the rotational axis b. Since small excitation are considered $b\theta_0 \approx X_0$, therefore, Equation 2.34 applies for both excitations. The moment $M = Pd$ would result in $P/[(\rho d^3)(d/\tau^2)]$ being multiplied by ratio b/d [2].

The study concludes by stating: "This important result shows that the geometrical scale is determined by the acceleration, liquid density and liquid viscosity ratios. If it is desired to test models so as to cover

a range of prototype accelerations, we may either fix the model diameter and vary the liquid properties, or fix the model liquid and vary the model size. Since the range of liquid properties is very restricted, a combination of these courses maybe chosen."[2]. This is the same methodology as presented in the section "Bond Number Equivalency".

Validation of these relations was done by comparing the results of a 2-3.5 foot diameter scale model test to those of a 9 foot diameter full scale ballistic missile courtesy of Army Ballistic Missile Agency (ABMA). The resulting tests demonstrated that the scale tanks could accurately reproduce the frequency and general character of the sloshing response [2]. When the Reynolds number was matched the measured damping and peak forces closely agreed the known full scale forces. Unfortunately the study does highlight that if gravity is not the dominant force the second term of Equation 2.34 becomes critical and Froude scaling breaks down [2], reconfirming that the Froude scaling method is not suitable for extrapolating results of tanks operating in drastically different gravity regimes.

2.7. Past Experiments

There have been a number of past experiments done on sloshing, both in space and on earth. Some of the most important ones are reported below.

Sloshsat-FLEVO (Facility for Liquid Experimentation and Verification in Orbit) was a dedicated microsatellite launched by ESA in 2005 to investigate the dynamics of liquid sloshing in microgravity [52]. Designed as a free-flying laboratory, it carried an internal tank filled with 33.5 liters of water, equipped with a suite of sensors including pressure transducers, capacitive fluid sensors, thermistors, and accelerometers. The mission's primary objectives were to study how liquid motion affects spacecraft attitude control, to validate CFD models of sloshing, and to investigate the coupling between fluid movement and the spacecraft's dynamic response in a low-gravity environment. Despite the promise of a comprehensive dataset, the quality and quantity of scientific data returned were limited, largely due to technical issues encountered post-launch, including telemetry losses and sensor saturation [52]. As a result, Sloshsat-FLEVO's experimental data proved insufficient for rigorous validation of slosh models, and many of its objectives remained only partially fulfilled. Nevertheless, the mission provided important insights into the challenges of fluid dynamics experimentation in space.

Several missions on the ISS have flown and produced useful data to validate existing low-g modeling methods. FLUIDICS, Slosh4AOCS was an ESA, Airbus Centre National d'études Spatiales (CNES) mission flown on ISS in 2019/2021 [33]. They had the purpose of conducting CFD based investigations of low-g single axis rotations at Bond numbers similar to those found in agile spacecraft. The result of this was that the ball in ball model [26] could be applicable for low Bond numbers in an unlocked free flying spherical tank [33]. These experiments made use of the Bond number equivalency scaling technique previously mentioned, with a large tank on earth and a small tank in space.

0g Aircraft flights and drop towers are also utilized to validate sloshing models, however they are limited

due to having inherently short experiment time in microgravity of maximum 2 minutes [26].This time restriction limits the available data for experiments involving tanks whose sloshing modes have long natural periods. Sounding rockets have also been utilized to conduct microgravity sloshing experiments; however they where found to be limited with approximately 20 seconds of microgravity achievable [11]. This time was found to be insufficient for sloshing dynamics examination as it is not enough time for the fluid to settle allowing for a comparative measurement[11].

2.7.1. Excitation profiles

Different excitation profiles have been tested throughout experiments found in literature. These excitation profiles are reported in the following section.

Bang-Stop-Bang

The bang-stop-bang profile is a motion trajectory commonly used in spacecraft maneuvers to deliberately induce or study sloshing behavior it has been widely used in SloshSat [52] and in the planning for the SPICEsat mission experiments [24]. It consists of three distinct phases: an initial “bang” acceleration, where the vehicle or tank is rapidly accelerated to a set velocity; a “stop” phase, during which the system coasts at constant velocity or remains stationary to allow the sloshing fluid to evolve freely; and a final “bang” deceleration, where an equal and opposite acceleration is applied to bring the system to rest. This profile can be completed with a RW by spinning up, stopping and then spinning up in opposite direction until the desired change of angle is reached before stopping once more[24].

This profile is ideal for sloshing studies because it mimics typical impulsive maneuvers in space (such as thruster firings) and excites the fluid’s natural modes without continuous forcing. The resulting fluid motion, especially the free oscillations during the coasting phase, provides valuable data for identifying slosh frequencies, damping behavior, and impact dynamics. It is widely used in both experimental and simulation contexts to validate models and observe the interaction between fluid motion and spacecraft dynamics[18].

Step in Acceleration

RW have also been used to produce a step input in acceleration, this is done by commanding a linear ramp in velocity which results in a square step in acceleration. This excites all sloshing modes and is a similar excitation as the one to enter barbecue mode, where a stage or spacecraft slowly rotates in space in order to obtain an even temperature distribution under solar radiation[18].

Ramp in Frequency

A ramp in frequency can be created by applying a sinusoidal wave in torque of constant amplitude but decreasing period. This results in the frequency of the torque being applied to the platform increasing, this input mode also called a chirp is useful for discovering and characterizing flexible modes in a structure. It is used in normal IOANT testing but can also be utilized for the propellant tank, important to note is that the increase in frequency needs to happen gradually and slowly in order to allow for the

flexible modes to develop[42]. If the ramp in frequency is too steep the modes may be skipped over [42].

2.8. Measurement Techniques

A variety of sensing methods have been employed in experimental and operational settings to characterize the sloshing phenomena within propellant tanks. The measurement techniques are split into two broad categories; direct slosh measurements from fluid and sensing effects that sloshing imparts on a given structure such as resulting forces and torques. Direct sensing techniques are Video Cameras and Pressure sensors whereas indirect measurement techniques are IMU's, Accelerometers, Force & Torque sensors.

2.8.1. Video Cameras

Video cameras, either external or embedded with transparent walled tanks, are used for qualitative and quantitative visualization of free surface dynamics [57]. In a study titled "Experimental and Numerical Investigation of Liquid Slosh Behavior Using Ground-Based Platforms" cameras where rigidly mounted to a sloshing tank recording directly the wavefront movement. The wavefront movement recording coupled with computer vision software was utilized to validate code predicting wavefront in tanks [57][26]. The test setup was a structure mounted on rails exited by a linear periodic acceleration, a rectangular tank which was pinned to the top of the structure allowing the tank to pivot back and fourth. A camera was rigidly placed on the tank to record the liquid movement and IMU's where placed on the tank to record the position of the container. The view of the camera is similar to Figure 2.12 although it is not the same experiment.

An interesting insight from this paper is the progressive form of testing, first a "frozen" equivalent mass was tested, followed by it being replaced with sloshing and finally with the tank itself being unpinned and the sloshing being free to couple with tank movement[57].

Cameras have also been widely used in several missions that have flown such as FLUIDICS [12], SPHERES [33] and the planned mission SPICEsat [24]. The most common application of video cameras was as input for neural networks or machine learning algorithms to predict sloshing forces generated by fluid [18]. The second most common application was to utilize direct video camera measurements to validate existing equivalent mechanical models for sloshing [18].

Video cameras have also been mounted inside full propellant tanks during actual rocket flights, notably on Saturn IVB Fuel and Hydrogen tanks and SpaceX CR4 Fuel tank, these recordings served to gain insight on fuel behavior during transition phases of flight such as engine cutoff.

2.8.2. Pressure Sensors

Pressure sensing inside of fluid tanks seeks to capture the transient load variations due to fluid motion, offering localized insight into wave impacts. This approach largely used capacitative liquid sensing

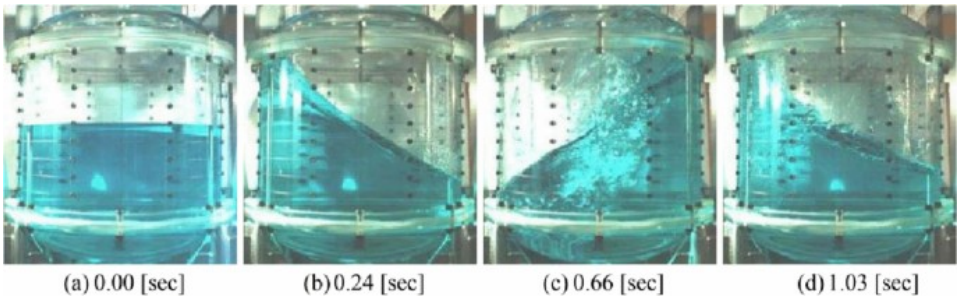

Figure 2.12: Image of fluid sloshing in a cylindrical tank during experiment as seen by rigidly mounted camera[58]

systems such as those found on SloshSat[52] and the planned SPICEsat [24]. Capacitive pressure pads function by measuring changes in capacitance caused by mechanical deformation of the sensor due to applied pressure. Each pad typically consists of two conductive plates separated by a dielectric layer; when an external force (such as from fluid impact) compresses the sensor, the distance between the plates decreases, altering the capacitance [24][18]. In the design of the SPICEsat mission 8 individual sensor strips each consisting of 16 discrete pressure pads where placed radially on the inside of the tank, this allowed for the creation of a pressure map of fluid-walled interactions[24]. Coupled with camera vision data this allowed to detect the location and magnitude of sloshing-induced forces.

2.8.3. IMU's Accelerometers

IMU's and Accelerometers are the most utilized sensors being often placed on the tank. They have been used in all major slosh missions and ground experiments [12][24][52][10][1].

Inertial Measurement Units (IMUs), which typically integrate high-precision gyroscopes and accelerometers, detect the dynamic response of a spacecraft or tank to internal fluid motion [18]. In the context of sloshing, as the liquid mass shifts inside the tank, it imparts forces and torques on the container walls, leading to small but measurable changes in the satellite's linear and angular motion. Accelerometers detect these variations as changes in translational acceleration, while gyroscopes record rotational rates caused by the unbalanced fluid mass [24][18]. When the sloshing liquid impacts the walls, it produces transient impulses that the IMU captures as disturbances superimposed on the satellite's baseline motion. In the SPICEsat mission [24], for instance, these measurements are sampled at high frequency ($\geq$100 Hz) to resolve low-frequency sloshing events (typically $\approx$ 1Hz) and isolate the sloshing-induced accelerations, which are predicted to be as small as $25\mu g$. By comparing the IMU output to known control inputs (e.g., from reaction wheels), it is possible to infer the contribution of sloshing torques to the overall system dynamics, enabling both model validation and real-time disturbance rejection in the spacecraft's attitude control algorithm [24]. In ground experiments IMU's have been used for the same purpose, to confirm the size of the of the inputs and the resulting forces coming from sloshing[57].

The main benefit of IMU's is their compactness, low price and ease of installation onto existing platforms. They do suffer from bias and drift which is an effect that gets progressively worse with time and needs to be compensated for.

2.8.4. Force Torque

Force and torque sensors mounted at the tank structure interface yield direct measurements of the reaction loads induced by sloshing, used for validating mechanical models as done with ESA hexapod [26] and have also been used during the FLUIDICS mission [12].

Force and torque sensors are used in sloshing detection to directly measure the mechanical loads imparted by the moving fluid on the tank structure. These sensors are typically mounted at key structural interfaces such as the base of the tank or between the tank and the satellite chassis to capture the net forces and moments generated during fluid motion. Fluid sloshing can induce asymmetric impacts that result in measurable torques on a satellites CoM, by recording these dynamic loads, force and torque sensors provide high-fidelity data that can be used to characterize slosh behavior, validate computational models.

3

Problem Statement

The objective of this thesis is to test the capabilities of the TRACTOR platform to investigate sloshing sloshing and to verify the platforms suitability to produce satellite or launcher design recommendations. In order to systematically achieve this goal research questions have been created along with an experimentation plan to answer the research questions. A plan diving up the available weeks to complete the thesis in the form of a Gannt chart is found in Appendix B.

The experimental methodology in this thesis follows a V-model framework (Figure 3.1) inspired by systems engineering, which ensures systematic traceability from conceptual modeling to real-world application. At the top level, the study is motivated by the need to understand fluid sloshing behavior in space environments and improve spacecraft design. On the left side of the V, the focus is on model development, where a surrogate slosh model is constructed and used to inform the experimental design. This design is then integrated into the TRACTOR test platform, leading to the practical implementation of the experiment at the base of the V. The right side then ascends through validation activities: testing the integration, analyzing experimental results, and drawing conclusions to refine the model. Each colored layer in the diagram represents a different level of depth, from theoretical context to implementation details, illustrating how the model's assumptions are verified experimentally and translated into actionable insights for spacecraft design.

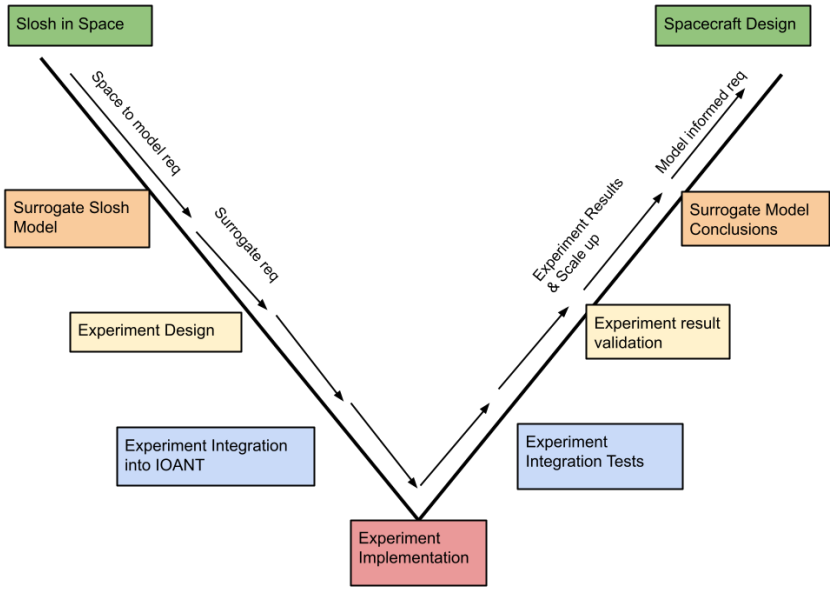

Figure 3.1: V-diagram indicating thesis plan

The Figure 3.1 led to the creation of research questions aimed at exploring the capabilities and limits of the testbed platform.

3.1. Research Questions

RQ1 – Platform Capability

To what extent can a on-ground test platform replicate and characterize relevant sloshing regimes for spacecraft in microgravity and launch vehicles in high-g regimes?

a. Which gravity regimes expected in S/C or launcher are not reproducible and why?

b. Which distinct sloshing regimes (linear, non-linear, rotary) can be reliably induced and observed on the platform?

   b.i. Can the linear and rotary sloshing motion be decoupled in a 1 DOF testing platform?

c. What test conditions (excitation, frequency, amplitude, fill level, tank size & placement) are required to trigger each identified regime in 1g?

RQ2 – Model Validation and Real-World Modeling Implications

How accurately do existing sloshing models (linear and nonlinear) predict the behavior observed on the test platform?

a. How well does the linear model match data in the low excitation amplitude regime?

b. When and how do nonlinear models improve agreement with measurements at higher amplitudes?

c. What are the limitations in model-data agreement and what are implications for real world modeling?

   c.i. Under what conditions is a linear model (spring mass) sufficient and when is a high-fidelity model warranted (conical pendulum, CFD) for capturing sloshing behavior?

   c.ii. What practical design or simulation guidelines can be derived for slosh modeling in real spacecraft or launcher applications?

3.2. Experimental Planning

In order to appropriately address the research questions, a series of controlled experiments involving the rotary hub and various sloshing tank configurations will be conducted, as outlined in Table 3.1. The experimental strategy follows an incremental approach. Initially, the focus will be on operating the platform within the linear sloshing regime to assess whether the system can reliably produce planar, harmonic sloshing in response to small-amplitude angular excitations mimicking lateral only excitation. Exploring the linear regime is targeted in tests T1/T2/T3, key parameters such as fill level, tank positioning relative to the axis of rotation, tank geometry, and input amplitude will be systematically varied to assess sensitivity and compared with analytical linear slosh models. Once confidence is established in the baseline regime, the excitation amplitude will be gradually increased to induce transitions into nonlinear and rotary sloshing regimes, these are specifically T4, T5 and T6. These higher energy states will allow exploration of more complex fluid behaviors, enabling a comparison with nonlinear models and evaluating the platform's capability to capture dynamic effects relevant to spacecraft and launcher applications. The final result will be a comprehensive overview of the sloshing testing capabilities of the platform and what useful design recommendations can result from tests with the platform. The bond number design space is one between 30 and 1000 which has been identified as the low-g slosh region in chapter 2.

Test ID	Objective	Input Variables	Excitation Type	Measurement Focus	Expected Sloshing Regime	Linked Research Questions
T1	Resonance Identification	Fill 50%, small amplitude motion	Frequency Sweep (decreasing period)	IMU: angular velocity peak; frequency identification	Linear (possibly rotary)	RQ1.a, RQ1.b, RQ1.c, RQ2.a, RQ2.b
T2	Structure mass variation	Change structure mass, same slosh tank	Frequency Sweep	Shift in resonance frequency based on mass ratio	Linear (possibly rotary)	RQ1.c, RQ2.a, RQ2.c
T3	Tank Diameter variation	Tank diameter	Frequency Sweep	Camera: wave period; IMU: angular velocity	Linear	RQ1.c, RQ2.a, RQ2.c
T4	Tank distance from center variation	Tank distance from axis	Frequency Sweep	Camera & IMU: velocity, wave period	Linear	RQ1.c, RQ2.a, RQ2.c
T5	Near-resonant sloshing, observe onset of nonlinearity	Fill ∼50%, Amplitude ± 3–$5°$, Frequency $\sim f_n$	Sinusoidal constant amplitude	Camera: wave growth/symmetry; IMU: angular rate	Slightly nonlinear	RQ1.b, RQ1.c, RQ2.a, RQ2.b
T6	High-amplitude resonance to induce nonlinear/rotary slosh	Fill ∼50%, Amplitude ± 8–$10°$, Frequency $\sim f_n$	Sinusoidal	Camera: swirl extremes; IMU: actual vs control	Highly nonlinear, rotary	RQ1.b, RQ1.c, RQ2.a, RQ2.b, RQ2.c
T7	Isolate rotary slosh (tank on rotation axis)	Fill ∼50%, Amplitude $\pm 5°$, Frequency $\sim f_n$	Sinusoidal	Camera & IMU: wave pattern, angular rate	Nonlinear (no lateral forcing)	RQ1.b, RQ1.c, RQ2.a, RQ2.c

Table 3.1: Experimental Planning Table

4

Modeling

A linearized classical pendulum model of a cylindrical tank undergoing forced sloshing has been implemented in order to be able to predict the responses of the fluid and for comparison with experiments. The derivation will follow a pendulum model was given for its adaptability to different levels of gravity in order to compare it to space in future experiments.

4.1. Single EoM, Force and Statespace

In this section generalized EoM for a linear pendulum system inside a moving tank will be found. These EoM will be linearized and the output force of the system derived. Following this the state space matrices will be constructed to allow for system analysis.

4.1.1. Generalized EoM derivation

Derivation of equations of motion for a single pendulum with mass system for a non damped scenario. The general assumptions for this scenario are presented below:

- Rigid massless rod of length l with tip point mass m
- Pendulum system is subjected to lateral acceleration $\ddot{x}_{\text{tank}}$
- The rod rotates about a pivot point
- All system parameters are constant with respect to time
- Values of system parameters are known without uncertainties

The assumption that the system parameters are constant with respect to means that the tank is being modeled at a single constant fill level. It is not being emptied as it would be during thruster firing in a S/C propellant tank.

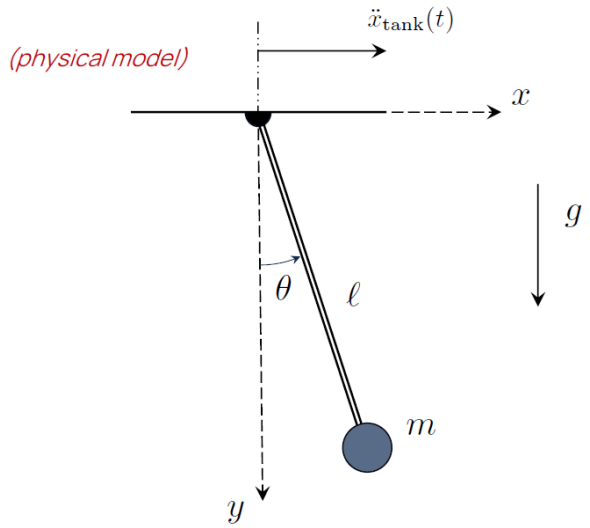

Figure 4.1: Undamped Pendulum System

We define the coordinate of point mass m in terms of generalized coordinate θ:

$$\begin{aligned} x_m &= \ell \sin\theta \\ y_m &= \ell \cos\theta \\ \dot{x}_m &= \ell \cos\theta\, \dot{\theta} \\ \dot{y}_m &= -\ell \sin\theta\, \dot{\theta} \end{aligned}$$

The Kinetic energy of the system can be defined as Equation 4.1 while the potential energy is Equation 4.2.

$$T = \frac{1}{2} m \left(\dot{x}_m^2 + \dot{y}_m^2\right) = \frac{1}{2} m \left(\ell^2 \cos^2\theta\, \dot{\theta}^2 + \ell^2 \sin^2\theta\, \dot{\theta}^2\right) = \frac{1}{2} m \ell^2 \dot{\theta}^2 \tag{4.1}$$

$$V = -mg\ell\cos\theta \tag{4.2}$$

These two can be subtracted one from the other to find the Lagrangian Equation 4.3.

$$\mathcal{L} = T - V = \frac{1}{2} m \ell^2 \dot{\theta}^2 - mg\ell\cos\theta \tag{4.3}$$

The virtual work done by the horizontal tank motion is Equation 4.4.

$$\delta \mathcal{W}_{nc} = -\delta x_m \cdot m \ddot{x}_{\text{tank}} = -m\ell\cos\theta\, \delta\theta \cdot \ddot{x}_{\text{tank}} \Rightarrow Q_\theta = -m\ell\cos\theta \cdot \ddot{x}_{\text{tank}} \tag{4.4}$$

Next we apply the Euler-Lagrange equation Equation 4.5.

$$\frac{d}{dt}\left(\frac{\partial \mathcal{L}}{\partial \dot{\theta}}\right) - \frac{\partial \mathcal{L}}{\partial \theta} = Q_\theta \tag{4.5}$$

$$\frac{\partial \mathcal{L}}{\partial \dot{\theta}} = m\ell^2\dot{\theta} \quad \Rightarrow \quad \frac{d}{dt}\left(\frac{\partial \mathcal{L}}{\partial \dot{\theta}}\right) = m\ell^2\ddot{\theta} \tag{4.6}$$

$$\frac{\partial \mathcal{L}}{\partial \theta} = mg\ell\sin\theta \tag{4.7}$$

$$m\ell^2\ddot{\theta} + mg\ell\sin\theta = -m\ell\cos\theta\,\ddot{x}_{\text{tank}} \tag{4.8}$$

This finally yields the simplified equation of motion for the pendulum in the moving tank Equation 4.9. This equation is w.r.t. time (it had not been shown before for clarity. This equations is the general nonlinear Lagrangian form of sloshing pendulum.

$$\ddot{\theta}(t) + \frac{g}{\ell}\sin\theta(t) = -\frac{1}{\ell}\ddot{x}_{\text{tank}}(t)\cos\theta(t) \tag{4.9}$$

- $\ddot{\theta}(t)$ is the acceleration of the pendulum, this is the inertial term, representing the pendulums resistance to changing motion.
- $\frac{g}{\ell}\sin\theta(t)$ is the restoring torque due to gravity working to align the pendulum parallel to the gravity field.
- $-\frac{1}{\ell}\ddot{x}_{\text{tank}}(t)\cos\theta(t)$ is the horizontal acceleration of the tank, as the tank accelerates the pendulum feels an inertial force in the opposite direction creating a torque around the pivot.

Damping can be introduced with the addition of the term $2\gamma\omega\dot{\theta}(t)$, this is opposes angular motion and models the energy dissipation due to viscous forces with tank boundaries and internal shear forces. This yields the general nonlinear damped Lagrangian for a sloshing pendulum of Equation 4.10.

$$\ddot{\theta}(t) + 2\gamma\omega\dot{\theta}(t) + \frac{g}{\ell}\sin\theta(t) = -\frac{1}{\ell}\ddot{x}_{\text{tank}}(t)\cos\theta(t) \tag{4.10}$$

4.1.2. Linearization

The equations shown thus far where nonlinear, however in order to conduct modal analysis and build state space models it is useful to linearize the EoM. The equations can be linearized around the equilibrium point Figure 4.2 as seen in Equation 4.11, this point represents where the pendulum is hanging straight down. In this equation the subscript i has been introduced to signify that this can occur for i amount of pendulums being represented.

$$\theta = 0, \quad \dot{\theta} = 0, \quad \sin\theta_i \approx \theta_i, \quad \cos\theta_i \approx 1 \tag{4.11}$$

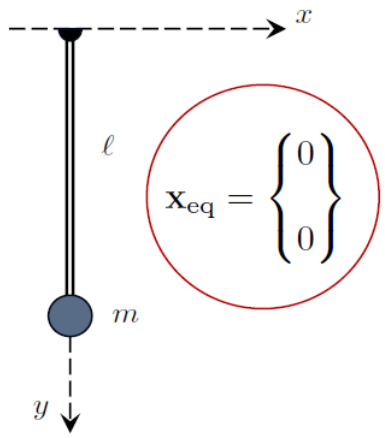

Figure 4.2: Linearization point for Equation 4.11

The undamped linearized EoM Equation 4.12

$$\ddot{\theta}_i = -\frac{g}{\ell_i}\theta_i - \frac{1}{\ell_i}\ddot{x}_{\text{tank}} \tag{4.12}$$

The damped linearized EoM Equation 4.13

$$\ddot{\theta}_i + 2\gamma_i\omega_i\dot{\theta}_i + \omega_i^2\theta_i = -\frac{1}{\ell_i}\ddot{x}_{\text{tank}}(t) \tag{4.13}$$

where $\theta_i(t)$ is the angular displacement, $\omega_i = \sqrt{g/\ell_i}$ is the natural frequency of the i-th pendulum, γ_i is the damping ratio, and $\ddot{x}_{\text{tank}}(t)$ is the horizontal acceleration input of the tank. Equation 4.13 will be the EoM considered in the following force derivations.

4.1.3. Derivation of the Force $F_x(t)$

We want to express the net horizontal force exerted by the damped system fixed mass + mobile masses as seen in Figure 4.3. The principle of linear momentum to the system of pendulums can be applied:

- The fixed mass m_0 accelerates with $u(t) = \ddot{x}_{\text{tank}}$
- To find the horizontal acceleration of each pendulum mass, we study the kinematics:

The position of mass m_i in the tank-fixed reference frame is:

$$x_{m_i}(t) = \ell_i \sin\theta_i(t)$$

Taking two derivatives with respect to time:

$$\dot{x}_{m_i}(t) = \ell_i \cos\theta_i(t) \cdot \dot{\theta}_i(t)$$

$$\ddot{x}_{m_i}(t) = \ell_i \left[-\sin\theta_i(t) \cdot \dot{\theta}_i^2(t) + \cos\theta_i(t) \cdot \ddot{\theta}_i(t) \right]$$

In the case of small oscillations ($\theta_i \approx 0$), we get:

$$\ddot{x}_{m_i}(t) \approx \ell_i \cdot \ddot{\theta}_i(t)$$

The net horizontal force exerted by the fluid on the tank is:

$$F_x(t) = -m_0 \ddot{x}_{\text{tank}}(t) - \sum_{i=1}^{10} m_i \ell_i \ddot{\theta}_i(t)$$

Substituting the damped equation of motion:

$$\ddot{\theta}_i = -2\gamma_i \omega_i \dot{\theta}_i - \omega_i^2 \theta_i - \frac{1}{\ell_i} u(t)$$

$$m_i \ell_i \ddot{\theta}_i = -2m_i \gamma_i \omega_i \ell_i \dot{\theta}_i - m_i g \theta_i - m_i u(t)$$

Therefore:

$$F_x(t) = -m_0 u(t) - \sum_{i=1}^{N} \left(-2m_i \gamma_i \omega_i \ell_i \dot{\theta}_i - m_i g \theta_i - m_i u(t) \right)$$

$$F_x(t) = -m_0 u(t) + \sum_{i=1}^{N} m_i g \theta_i + \sum_{i=1}^{N} 2m_i \gamma_i \omega_i \ell_i \dot{\theta}_i + \sum_{i=1}^{N} m_i u(t)$$

$$F_x(t) = \left(\sum m_i - m_0 \right) u(t) + \sum_{i=1}^{N} m_i g \theta_i + \sum_{i=1}^{N} 2m_i \gamma_i \omega_i \ell_i \dot{\theta}_i \tag{4.14}$$

4.1.4. State-Space Formulation of the Damped Multi-Pendulum Model

To simulate the dynamics of a sloshing tank modeled as a multi-pendulum system, we begin by transforming the second-order differential equations of motion into first-order state-space form. This allows for efficient numerical integration and system analysis using matrix-based techniques.

We consider the linearized, damped equation of motion for the i-th pendulum derived earlier in Equation 4.13. We define the state variables for each pendulum mode as follows:

$$x_{2i-1} = \theta_i, \quad x_{2i} = \dot{\theta}_i \tag{4.15}$$

This allows us to write the dynamics of each pendulum in first-order form:

$$\begin{bmatrix} \dot{x}_{2i-1} \\ \dot{x}_{2i} \end{bmatrix} = \begin{bmatrix} 0 & 1 \\ -\omega_i^2 & -2\gamma_i \omega_i \end{bmatrix} \begin{bmatrix} x_{2i-1} \\ x_{2i} \end{bmatrix} + \begin{bmatrix} 0 \\ -\frac{1}{\ell_i} \end{bmatrix} u(t) \tag{4.16}$$

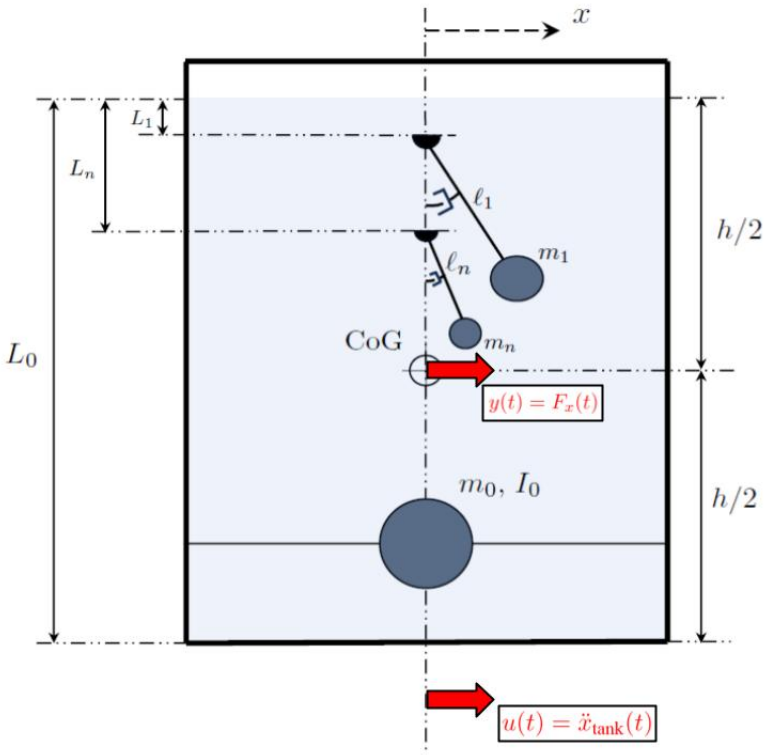

Figure 4.3: Damped System of pendulums

Stacking the state equations for $i = 1, 2, \ldots, N$, we obtain the global state-space system:

$$\dot{x}(t) = Ax(t) + Bu(t) \tag{4.17}$$

where $x(t) \in \mathbb{R}^{2N}$ is the global state vector, and the system matrices are:

$$A = \text{blkdiag}\left(\begin{bmatrix} 0 & 1 \\ -\omega_1^2 & -2\gamma_1\omega_1 \end{bmatrix}, \ldots, \begin{bmatrix} 0 & 1 \\ -\omega_N^2 & -2\gamma_N\omega_N \end{bmatrix}\right) \tag{4.18}$$

$$B = \begin{bmatrix} 0 \\ -\frac{1}{\ell_1} \\ \vdots \\ 0 \\ -\frac{1}{\ell_N} \end{bmatrix} \in \mathbb{R}^{2N\times 1} \tag{4.19}$$

The output of interest is the total horizontal force $F_x(t)$ exerted by the fluid on the tank, derived earlier in Equation 4.14.This can be expressed in the standard form.

$$y(t) = Cx(t) + Du(t) \tag{4.20}$$

where the output matrix $C \in \mathbb{R}^{1\times 2N}$ and scalar D are defined by:

$$C = \begin{bmatrix} m_1 g & 2m_1\gamma_1\omega_1\ell_1 & \cdots & m_N g & 2m_N\gamma_N\omega_N\ell_N \end{bmatrix} \tag{4.21}$$

$$D = \sum_{i=1}^{N} m_i - m_0 \tag{4.22}$$

This completes the derivation of the full state-space representation for the damped, linearized multi-pendulum sloshing model.

4.2. System Response

Utilizing the linearized state space model of the tank created the sloshing can be analyzed in different input conditions. The implemented model is the pendulum model for a cylindrical tank from Dodge [16], the parameters describing the model are found in Table 4.1. The test scenario is a 0.11m diameter cylindrical tank with a fill level of 0.1m, this is of a similar size to a tank being tested with.

Table 4.1: Model Parameters for a Cylindrical Tank [16]

Parameter	**Expression**
Slosh mass, m_n	$m_{\text{liq}} \left[\frac{d \tanh\left(\frac{2\xi_n h}{d}\right)}{\xi_n(\xi_n^2-1)h} \right]$
Pendulum length, L_n	$\frac{d}{2\xi_n \tanh\left(\frac{2\xi_n h}{d}\right)}$
Pendulum hinge location, H_n	$\frac{h}{2} - \frac{d}{2\xi_n}\left[\tanh\left(\frac{\xi_n h}{d}\right) - \frac{1}{\sinh\left(\frac{2\xi_n h}{d}\right)}\right]$
Rigidly attached mass, m_0	$m_{\text{liq}} - \sum m_n \approx m_{\text{liq}}\left[1 - \frac{d\tanh\left(\frac{2\xi_n h}{d}\right)}{\xi_n(\xi_n^2-1)h}\right]$
Rigidly attached mass location, H_0	$\frac{\sum m_n(H_n - L_n)}{m_0}$

Note: $m_{\text{liq}} = \frac{\pi}{4}\rho d^2 h \qquad \xi_1 = 1.841,\ \xi_2 = 5.329,\ \xi_3 = 8.531,\ \xi_n \approx \xi_{n-1} + \pi$

The first result from this is the frequencies and parameters for different modes. Calculations have been done up to the 10th mode in Table 4.2. As can be seen the majority of the sloshing mass in movement during resonance is found in the first mode, the second mode is a full two orders of magnitude smaller than the mass in movement in the first mode.

Table 4.2: Multi-Pendulum Model Tank d=0.11m h = 0.1m Parameters

n	m_n **[kg]**	L_n **[m]**	H_n **[m]**	ω_n **[rad/s]**	f_n **[Hz]**
1	0.23707	0.029949	0.02426	18.098	2.8805
2	0.0071598	0.010321	0.039682	30.83	4.9068
3	0.0017072	0.0064471	0.043553	39.000	6.2083
4	0.00066216	0.0047119	0.045828	45.629	7.262
5	0.00032301	0.0037127	0.046287	51.403	8.1811
6	0.00018114	0.0030631	0.046937	56.592	9.0609
7	0.00011157	0.0026067	0.047393	61.343	9.7631
8	7.353e-05	0.0022691	0.047731	65.752	10.465
9	5.0994e-05	0.0020087	0.047991	69.883	11.124
10	3.6803e-05	0.001802	0.048198	73.784	11.743

4.2.1. Error Analysis for Reduced-Order Pendulum Models

To evaluate the impact of model order on simulation accuracy, a relative error analysis is conducted by comparing the impulse response of the full 10-pendulum system (taken as the reference model) with reduced-order models consisting of $N = 1$ to $N = 10$ pendulums. The results of this analysis can be seen in Figure 4.4.

For each reduced model, the corresponding dynamic matrices A_n, B_n, and C_n are assembled by including only the first n modes. The output force response $F_x^n(t)$ is then computed analytically [35] using the matrix exponential:

$$F_x^n(t) = C_n e^{A_n t} B_n \tag{4.23}$$

This is compared against the reference response $F_x^{10}(t)$ generated using all ten pendulums. The relative error is computed as:

$$\varepsilon_n = \frac{\max_t |F_x^n(t) - F_x^{10}(t)|}{\max_t |F_x^{10}(t)|} \tag{4.24}$$

This error metric allows for the identification of the minimum number of pendulum modes required to stay within acceptable accuracy thresholds. Tolerance levels such as 5% and 1% are used to guide the selection. This trade-off analysis is particularly important when seeking a balance between computational efficiency and model fidelity in real-time simulation, control design, or slosh mitigation strategies.

The results from this error analysis is that a system of 4 pendulums already offers significant precision deviating less that 1% from the impulse response of a 10 pendulum system. Therefore multi-pendulum systems of the order n=4 provide a sufficient level of accuracy.

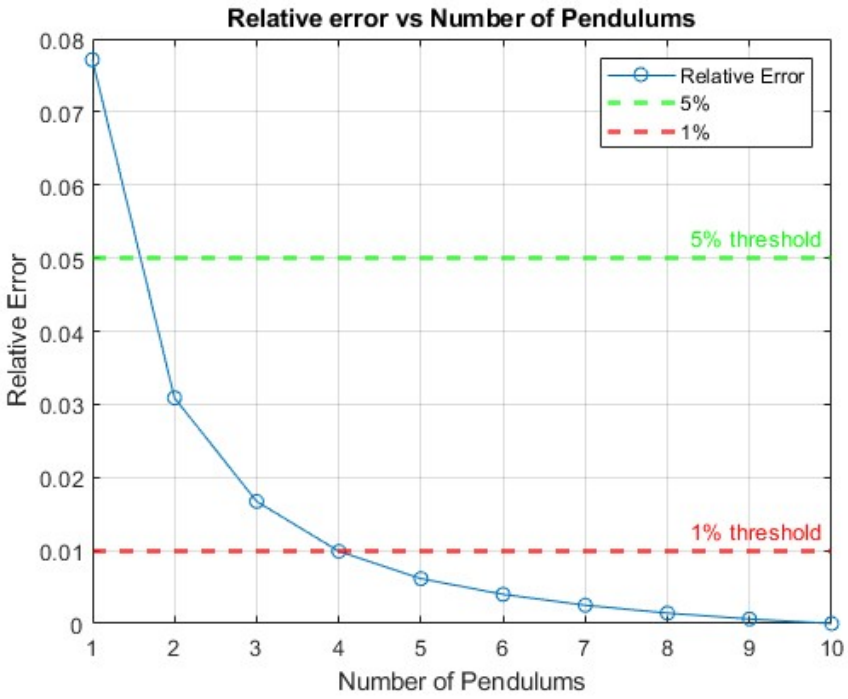

Figure 4.4: Relative Error of multi-pendulum model

4.3. Frequency

To find the Transfer Function (TF) of the system the laplace transform of the Ordinary Differential Equation (ODE) converting to frequency domain. The TF then is the ratio of Force outputted from the sloshing liquid to the input which is the acceleration of the tank. The TF is used in characterizing the system's frequency response and dynamic behavior in terms of poles, zeros, and damping.

$$\begin{cases} \dot{x}(t) = A\mathbf{x}(t) + Bu(t) \\ y(t) = C\mathbf{x}(t) + Du(t) \end{cases}$$

Laplace transform application

$$\begin{cases} sX(s) = AX(s) + BU(s) \\ Y(s) = CX(s) + DU(s) \end{cases}$$

Solving the first equation for $X(s)$

$$(sI - A)X(s) = BU(s) \quad \Rightarrow \quad X(s) = (sI - A)^{-1}BU(s)$$

Substituting $X(s)$ into the second equation

$$Y(s) = CX(s) + DU(s) = C(sI - A)^{-1}BU(s) + DU(s)$$

System transfer function in Equation 4.25:

$$G(s) = \frac{Y(s)}{U(s)} = C(sI - A)^{-1}B + D \tag{4.25}$$

It is very useful to compare the system to the frozen liquid to highlight the effect of sloshing.

$$F_x = M_{\text{liq}}\ddot{x}$$

In the Laplace domain:

$$F_x(s) = M_{\text{liq}}s^2X(s)$$

The transfer function becomes:

$$H(s) = \frac{Y(s)}{X(s)} = M_{\text{liq}}s^2$$

and its frequency response is plotted together with the systems frequency response can be found in Figure 4.5. The frequency of the modes found matches that found in Table 4.2. Figure 4.5 clearly shows the difference between the response of the frozen system vs the sloshing component of the system. Frequency analysis as presented will be of use in the analysis of the experimental results.

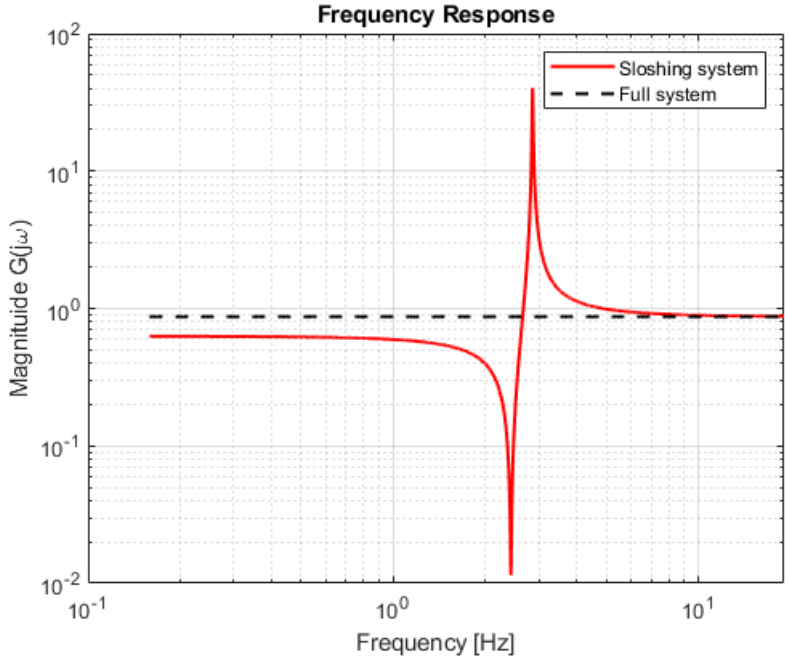

Figure 4.5: Frequency Response to step acceleration for N=1 system

4.4. Coupled EoM sloshing and platform

The experimental platform consists of a rigid hub rotating about the global z-axis with angular position $\theta(t)$. A partially filled liquid tank is mounted at a fixed radial offset

$$\mathbf{r} = [\, r,\, 0,\, 0\,],.$$

The dominant linear liquid motion is lateral sloshing in the $\hat{\mathbf{y}}$-direction. The lateral acceleration transmitted to the fluid by the platform is produced by the Euler (tangential) acceleration component. The centripetal term $\boldsymbol{\omega} \times (\boldsymbol{\omega} \times \mathbf{r})$ acts along $\pm\hat{\mathbf{x}}$ and therefore does not excite the lateral sloshing mode; it is neglected in the linearized model.

The resulting lateral base acceleration experienced by the fluid is Equation 4.4

$$a_{\text{lat}} = (\dot{\boldsymbol{\omega}} \times \mathbf{r}) \cdot \hat{\mathbf{y}} = r\,\ddot{\theta}. \tag{4.26}$$

The lateral sloshing motion is represented using an equivalent pendulum model developed in Equation 4.13.

Let $\alpha(t)$ denote the slosh angle relative to the tank, ℓ the effective pendulum length, and ζ the modal damping ratio. The natural frequency is $\omega_n = \sqrt{g/\ell}$. The equation of motion for the sloshing mode is

$$\ddot{\alpha} + 2\zeta\omega_n\dot{\alpha} + \omega_n^2\alpha = -\frac{a_{\text{lat}}}{\ell} = -\frac{r}{\ell}\ddot{\theta}. \tag{4.27}$$

The total liquid mass m_{liq} is decomposed into a frozen (impulsive) component m_0 and a sloshing (convective) component m_s. The lateral reaction force exerted by the liquid on the tank is

$$F_y = m_0 a_{\text{lat}} + m_s g\,\alpha + 2m_s\zeta\omega_n\ell\,\dot{\alpha}. \tag{4.28}$$

The first term represents the rigid-body contribution, whereas the remaining terms correspond to the dynamic sloshing forces. Introducing the mapping $x = \ell\alpha$, these terms correspond to the familiar mass-spring-damper representation.

Let I_{dry} denote the dry structural inertia about z. Including viscous hub damping b and the commanded actuator torque τ_{cmd}, the fluid torque acting on the hub is

$$\tau_{\text{fluid}} = rF_y.$$

The hub damping is simply represented by viscous damping term associated with the angular velocity of the platform, further on this will be expanded to full nonlinear friction but an initial simpler representation is used.

Moving the frozen-mass term $m_0 a_{\text{lat}} = m_0 r\ddot{\theta}$ to the left-hand side via the parallel-axis theorem yields the coupled hub equation of motion Equation 4.4.

$$\left(I_{\text{dry}} + m_0 r^2\right)\ddot{\theta} + b\,\dot{\theta} + r\left(m_s g\,\alpha + 2m_s\zeta\omega_n\ell\,\dot{\alpha}\right) = \tau_{\text{cmd}}. \tag{4.29}$$

This equation shows the coupling between the hub dynamics and the sloshing motion. When the slosh angle α oscillates near its natural frequency ω_n, the fluid torque term modulates the hub response and produces the envelope behavior observed experimentally. A state space representation of the Equation 4.4 can be created as previously shown for the tank only state space derivation.

5

Platform Description and Characterization

5.1. Platform Description

The following subsections describe the TRACTOR platform [51] as used during the identification experiments, the sloshing tank, actuator and excitation input methods along with characterization and identification techniques that where utilized.

5.1.1. Platform

The TRACTOR platform is in its sloshing configuration is composed of two parts, the top rotating assembly and the bottom static assembly connected together through a thrust bearing as seen in Figure 5.1. The top rotating assembly contains the electronics (not represented), sensors, battery, reaction wheel and the fluid tank. The bottom assembly is static and serves as an anchor for the rotating assembly, it is composed of a large mass held by 3 feet allowing for leveling of the platform by means of adjusting the extension of the feet. A problem encountered through multiple iterations of the platform was the rotating assembly becoming unbalanced due to uneven load. This was mitigated by lead counterweights and a specially developed bearing and anchor system. A vertical steel rod anchored to the static assembly mass protrudes into the rotating assembly and is constrained side to side by two radial bearing. These allow the top assembly to rotate around z axis while constraining movement in the x and y axes as seen in Figure 5.2 and Figure 5.3. The states of the platform are $\theta, \dot{\theta}, \ddot{\theta}$ respectively angular position, velocity and acceleration. The platform receives its commands wireless via WiFi over to a Raspberry Pi and Arduino, the power is provided from an onboard 24V battery (represented in blue in Figure 5.1) this allows the platform to be as frictionless as possible, with the only sources of friction coming from the bearing and the aerodynamic drag of the platform. The friction of the bearing will be addressed later on

while the aerodynamics will be ignored as the platform spends a lot of time at low velocities and since aerodynamic drag increases with the square of velocity it was not considered significant.

The platform integrates a compact onboard electronics architecture centered on a Raspberry Pi 4 Model B, which serves as the primary processing unit. The Raspberry Pi handles real-time execution of the control algorithms, sensor acquisition, and actuator command generation. It interfaces with the hub mounted LSM6DS3 IMU via I^2C for the angular rate and linear acceleration measurements, and communicates with the reaction wheel unit over a dedicated UART serial link [46]. An image of the IMU is found in Figure 5.4, the IMU records angular velocity in 3 axes and linear acceleration in the same axes, angular acceleration or tilt is not available. The IMU is set with its axes in aligned with the axis system seen in Figure 5.2, the X axis goes from the tank to the RW, the Y axis goes across the electronics and the Z axis is vertical, the origin of this axis system is aligned with the central rod.

The broad set of available interfaces (GPIO, UART, I²C, Ethernet, and Wi-Fi) allows the platform to accommodate a range of sensors and auxiliary modules, making the system flexible and straightforward to extend. A phone camera will be utilized to record the individual runs and may be used to identify the wave height during sloshing resonance. By placing the camera perpendicular to the liquid level and adding a ruler to the side of the tank an estimation of the wave height can be made.

A high-level control interface running on an external host computer complements the onboard electronics. Using a model-based workflow, control algorithms can be developed in Simulink and automatically deployed to the Raspberry Pi through Embedded Coder. External Mode provides a live bidirectional link between the host and the platform, enabling real time parameter tuning, execution monitoring, and safe iteration of different control strategies without interrupting operation. Communication is handled through a stable XCP link, allowing deterministic data streaming and command exchange.

The system also incorporates an efficient and highly configurable data-logging pipeline. Any internal signal such as IMU measurements, actuator commands, controller states, or telemetry can be selected for logging and streamed back to MATLAB during experiments. This ensures synchronized, high resolution recording of all relevant variables without requiring manual data handling or custom scripts. The combination of robust onboard computation, flexible interfacing, and structured logging makes the platform a versatile experimental tool for controlled motion studies and control-system development.

5.1.2. Sloshing Tank

The sloshing tank itself is a large plastic jug that was bought from a local shop, its characteristics are found in Table 5.1. The tank is then secured to the top part of the of the rotating assembly through zip ties. The virtual pendulum that exists within the tank is represented in Figure 5.2 as a pendulum sloshing in the Y axis. A notable challenge is that the tank does not have a flat bottom as seen in Figure 5.5. This is an important difference since theory dictates that tanks have flat bottoms, however this tank has an upwards convex bottom (for structural reasons) this is not accounted for in the literature found. This convex structure is 1.4 cm in height, in order to smooth it out several solutions where proposed such as

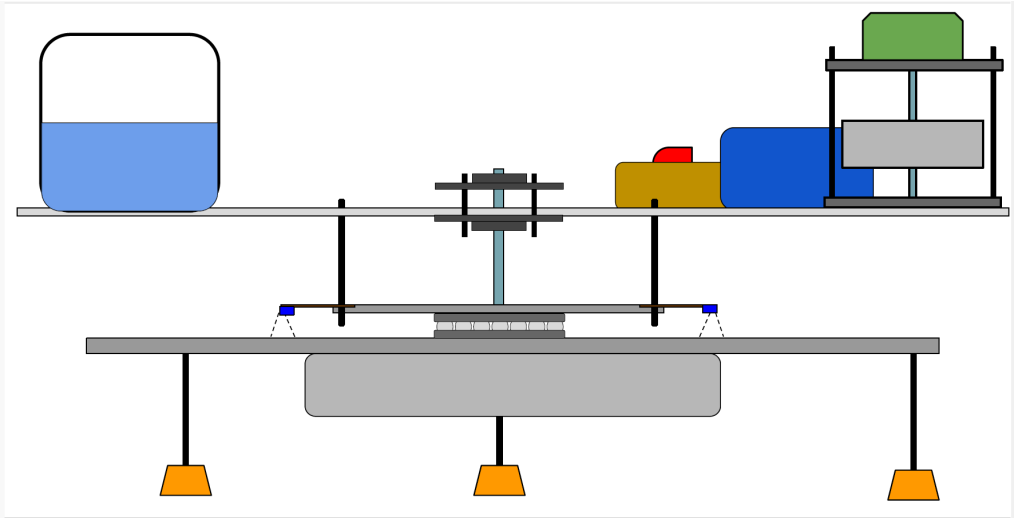

Figure 5.1: Diagram of TRACTOR Platform in sloshing configuration

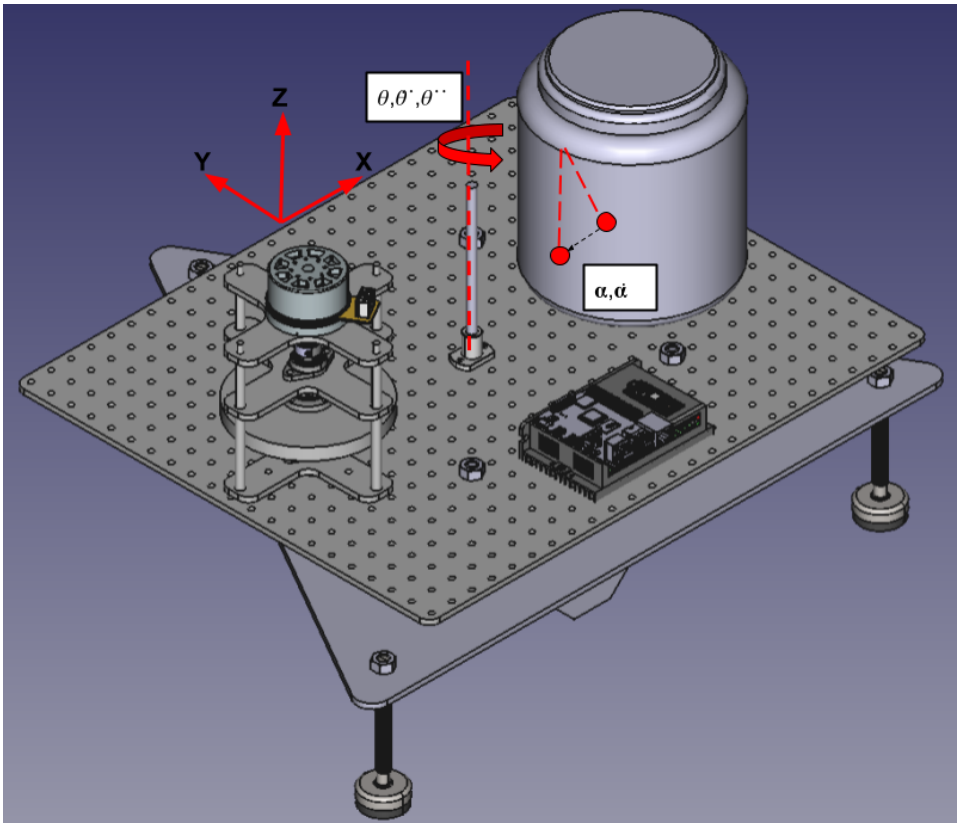

Figure 5.2: Three quarter view CAD platform and tank with axes

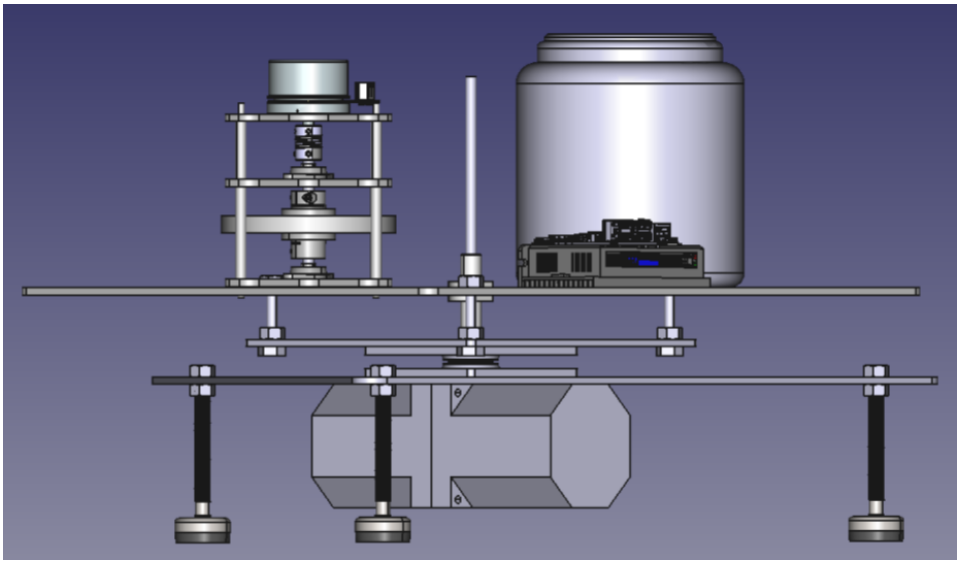

Figure 5.3: Side view CAD platform and tank with axes

Mass:	0.231 kg
Diameter:	0.163 m
Height (bottom to top of cap)	0.225 m
Height to tank shoulder	0.16 m
Distance center of tank to platform center of rotation	0.225 m

Table 5.1: Sloshing tank characteristics

filling the bottom with epoxy or sand, however ultimately none where attempted and the solution used was to set the 0 fill level of the tank at a liquid level where the convex part of the tank was covered. This is in hope of replicating the flat floor assumption found in literature for linear sloshing. The lowest fill level planned for the experiments will be 5cm, which will be measured from the top of the convex dome at the bottom of the tank.

The bond number that can be replicated with the tank is a function of its diameter, fluid density and viscosity, the gravity gradient and any additional accelerations the tank may be subjected to as seen in the bond number equations Equation 2.22. Under the assumption of water having a density of 997 kg/m^3 [17] and having a viscosity of 0.072 N/m at a temperature of 25 degrees Celsius [48], with standard sea level gravity of 9.81 m/s^2 this yields a bond number of 902.3. This is within the range of low-g sloshing, however it does find itself on the higher end of the scale found in chapter 2. The bond number indeed becomes smaller with decrease in the diameter of the tank, this relationship has been illustrated in Table 5.6. The figure is marked with final tank iteration with a diameter of 0.163m has been shown along with a tank used in testing that had diameter of 0.111m, the smaller tank would have yielded a bond number of 420, however was too loosely coupled and with the structure. This was due to the small amount of liquid in the tank relative to the structure, therefore for the final tests it was

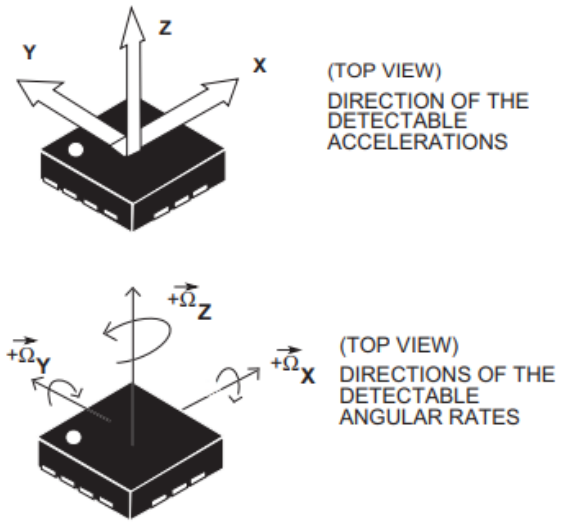

Figure 5.4: LSM6DS3 IMU [46]

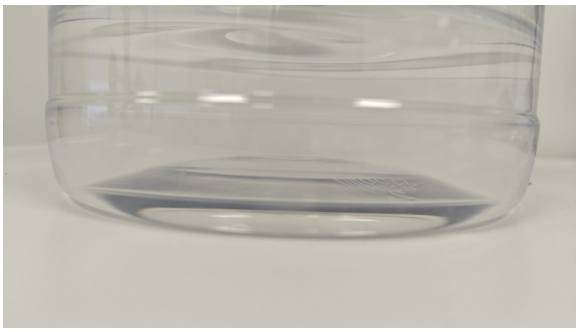

Figure 5.5: Zoomed in tank bottom

chosen to use a larger tank so that the coupled platform tank movements where clearly detectable by the IMU while retaining a bond number in the low g regime.

Table 5.2: Sweep characteristics

Parameter	Value
f_0	1.25 Hz
f_1	3.5 Hz
s_r	$\frac{1}{1200}$ Hz/s

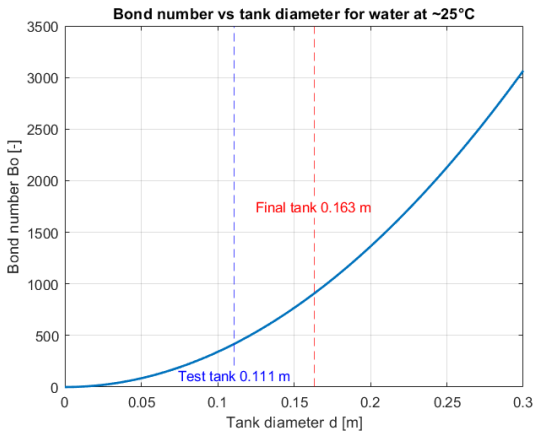

Figure 5.6: Change in bond number with decreasing tank height for water at 25°C

5.1.3. Actuator

The actuator used to input torques onto the platform is a reaction wheel, it has been build in-house within GMV and is of a design of the author. The design and testing of the RW is not treated in depth as it was part of the internship work and for the purposes of the thesis it is a ready made part that exists as part of the structure. The reaction wheel as seen in Figure 5.7 is made up of a commercially available motor, motor driver (represented as the electronics block in Figure 5.2) and bearings, the cage and flywheel have been specially produced for IOANT. The characteristics of the flywheel are reported in Table 5.4 The electronics come from Maxxon, the motor is a EC60 flat with characteristics reported in Table 5.3

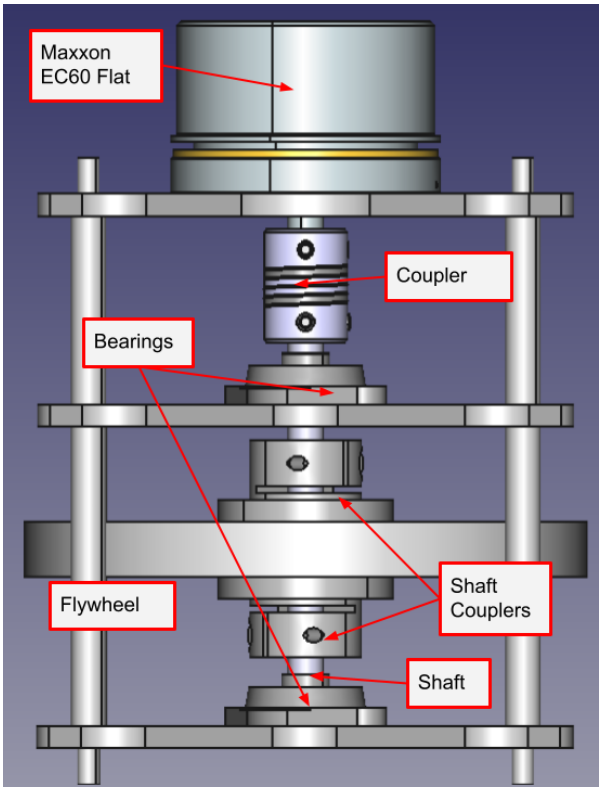

Figure 5.7: Reaction wheel with annotated CAD

and the motor driver is an ESCON 50/5 servo controller with a max continuous output current of 5A and 15A burst [32]. Due to current limitations by the driver the maximum continuous operating torque for IOANT and adjacent experiments was set at 0.26 Nm. The operating envelope of the actuator is from 200 rpm to 3000 rpm, in order to avoid zero crossings the wheel is operated at a nominal speed of 1600 rpm and torques are produced by varying $\pm 1400 rpm$. Due to these limitations in torque the following discrete torque levels are chosen for the varying amplitude inputs, these torque values are 0.0125, 0.025, 0.05, 0.075, 0.10, 0.125, 0.15, 0.175, 0.20, 0.225 and 0.25 Nm. This represents an increment of 0.025 Nm with a finer increment at the smallest amplitudes to identify linear sloshing.

Table 5.3: Maxon EC 60 Flat 150 W Motor [31]

Characteristic:	**Value**
Max. sustained torque	381 mNm
Max continuous current	12.1 A
Motor torque constant (k_m)	30.0 mNm/A
Max. speed	6000 rpm
Weight	390 g
Sensor type	3 Hall sensors

Table 5.4: Reaction Wheel Flywheel Characteristics

Characteristic:	**Value**
Mass	1.119 kg
Radius (flywheel)	125 mm
Height (flywheel)	12 mm
Moment of inertia	2.25 kg m^2

5.1.4. Excitation Method

A sweep excitation was selected as the primary method for exciting the platform, as it provides a controlled and repeatable means of stimulating the structure across the desired frequency range. A sweep (or chirp) signal is constructed by allowing the instantaneous excitation frequency to vary continuously with time [45]. It may be expressed in the general form:

$$x(t) = A\sin\big(\phi(t)\big),$$

where A is the excitation amplitude and $\phi(t)$ is the phase. The instantaneous angular frequency is obtained from

$$\omega(t) = \frac{d\phi(t)}{dt}.$$

Both in the thesis and in general IOANT experiments, an exponential sweep is generated by prescribing a frequency law of the form

$$\omega(t) = \omega_0\ \exp\big(\alpha t\big),$$

where ω_0 is the starting angular frequency and α is determined from the desired sweep rate expressed directly in $\mathrm{Hz/s}$. Given a start frequency f_0, an end frequency f_1, and a linear sweep rate $s_r = \mathrm{d}f/\mathrm{d}t$, the total sweep duration is simply

$$T_{\mathrm{sweep}} = \frac{f_1 - f_0}{s_r},$$

and the parameters of the chirp follow straightforwardly. The final sweep characteristics used in this study are summarized in Table Table 5.2.

A fundamental requirement for the successful application of sweep excitation is that the sweep be sufficiently slow so that the system's response at each instantaneous frequency may be treated as quasi-stationary. If the frequency is varied too rapidly, lightly damped or low-frequency modes cannot reach steady-state before the excitation frequency changes appreciably. This causes distortions such as broadened or asymmetric modal peaks and biased estimates of resonance frequency and damping. To avoid these transient effects, the final sweep rate of $1/1200\,\mathrm{Hz/s}$ Table 5.2 was selected to ensure that the measured response represents the true steady-state behavior of the system rather than transient tracking artifacts [45]. This choice of sweep rate results in rather slow sweeps lasting 45 minutes each.

Broadband excitation, such as white or Coloured noise, is often preferable for modal identification because it excites all frequencies within a band simultaneously, reduces measurement time, and improves statistical robustness. However, broadband inputs require the actuator to deliver rapidly varying torque with sufficient amplitude across the entire frequency range of interest. In the present setup, the reaction wheel did not possess the necessary torque bandwidth to support such excitation, and the introduction of colored noise inputs resulted in additional spectral shaping that could not be compensated using the available hardware. Consequently, the slow, well-controlled sweep described above represented the only practically viable excitation method for reliably characterizing the coupled sloshing–hub dynamics of the platform.

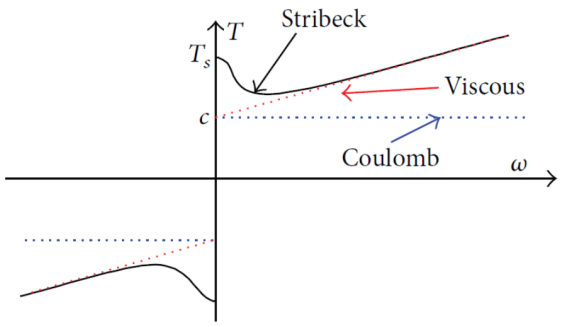

Figure 5.8: Nonlinear friction τ_f vs ω [8]

5.2. Nonlinear Friction Modeling and Parameter Identification

Accurate modeling of bearing friction is critical for achieving high-fidelity attitude dynamics in the single-axis platform. The friction torque acting on the hub is dominated by nonlinear effects arising from viscous shear, boundary-lubrication contact, and the Stribeck transition region, as commonly reported in the bearing-friction literature [8, 43]. In this section, a nonlinear friction model is introduced together with a time-domain identification strategy. Unlike typical approaches, the estimator developed in this work also determines the aggregate rotational inertia of the platform jointly with the friction parameters. This improves estimation accuracy and produces an inertia value that can later be used for independent verification steps in the modeling pipeline.

5.2.1. Nonlinear Friction Model

The bearing torque is represented using a standard three-component model, capturing viscous, Coulomb, and Stribeck effects. The internal expression used within the estimator is

$$\tau_f(\omega) = -\left[b\,\omega + \mathrm{sgn}(\omega)\,\left(c + d\,\exp\!\left(-(\omega/\omega_s)^2\right)\right)\right], \tag{5.1}$$

where b is the viscous coefficient, c the Coulomb level, d the additional static component above Coulomb friction, and ω_s a characteristic Stribeck speed. The parameter vector estimated from experimental data is

$$\mathbf{p} = [\,b,\ c,\ d,\ \omega_s,\ I\,]^{\mathsf{T}},$$

where I is the total rotational inertia of the hub, bearing, wheel, and attached hardware. Equation 5.1 can be plotted as seen in Figure 5.8.

5.2.2. Identification Strategy

The rotational dynamics of the platform are described by

$$I\,\dot{\omega} = \tau_c md - \tau_f(\omega), \tag{5.2}$$

where τ_{cmd} is the reaction-wheel torque, computed from the commanded motor current using the torque constant. Because the friction model is nonlinear in its parameters, the identification problem is formulated directly in the time domain. The raw data from multiple test runs (torque ramps, steps, and sine

sweeps) are first bias-corrected, delay-aligned, and trimmed before being combined into a unified estimation dataset.

To reduce noise sensitivity, the estimator employs the interior finite difference of successive angular rates,

$$y_k = \frac{\omega_{k+1} - \omega_k}{\Delta t_{k+1} + \Delta t_k}, \tag{5.3}$$

where $\Delta t_k = t_k - t_{k-1}$. This expression is more numerically stable than a single-step forward difference and better preserves high-frequency information.

Substituting (5.3) into the discrete dynamics yields

$$I\, y_k = \tau_k + \tau_f(\omega_k), \tag{5.4}$$

which forms the basis of the least-squares formulation.

A key advantage of rewriting the equation with the inertia I multiplying y_k is improved numerical conditioning. In this form, the strong correlation that typically appears between I and the viscous coefficient b is significantly reduced, leading to more reliable joint estimation.

5.2.3. Nonlinear Least-Squares Formulation

The identification procedure minimizes the discrepancy between the measured acceleration y_k and the model prediction (5.4). Run-aware, optional time-weighted residuals are used to balance the contributions of different experiments and to ensure that long-duration sweeps do not dominate short manoeuvres.

Let w_k denote the weight assigned to the k-th sample, depending on the chosen strategy (uniform, time-weighted, per-run normalized, or a combination). Cross-run boundaries are suppressed by setting $w_k = 0$ when samples k and $k+1$ originate from different experimental runs.

The weighted residual used in the solver is therefore

$$\tilde{r}_k(\mathbf{p}) = \sqrt{w_k}\left[I\, y_k - \tau_k - \tau_f(\omega_k;\, b, c, d, \omega_s)\right]. \tag{5.5}$$

The nonlinear least-squares problem solved by `lsqnonlin` is

$$\mathbf{p}^\star = \arg\min_{\mathbf{p}} \sum_k w_k \left(I\, y_k - \tau_k - \tau_f(\omega_k; \mathbf{p})\right)^2, \tag{5.6}$$

subject to lower and upper parameter bounds consistent with physical limits.

5.2.4. Joint Estimation of Inertia

Including the inertia I directly in the parameter vector is a central feature of the proposed methodology. Estimating I jointly with the friction parameters yields two key benefits:

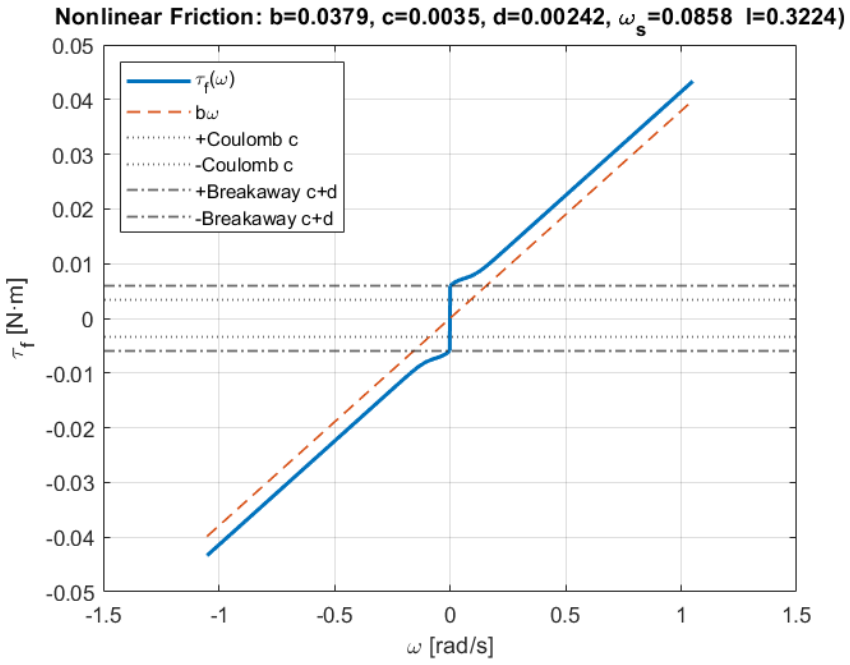

Figure 5.9: Estimated friction parameters and aggregate inertia from the joint NLLS

1. **Improved friction estimation accuracy.** The residual formulation (5.5) reduces parameter coupling, especially between I and the viscous term b, leading to a significantly better-conditioned Jacobian and more reliable fits. This is confirmed numerically by the condition-number and parameter correlation diagnostics computed by the solver.
2. **Independent verification of inertial properties.** The resulting inertia estimate reflects the *aggregate* inertia of the wheel, hub, and attached components as seen through the bearing interface. This value can later be compared against an analytical estimation of inertia as a useful validation step.

Table 5.5: Estimated friction parameters and aggregate inertia from the joint NLLS fit.

Parameter	Estimated Value
b (viscous term)	$0.03793\ \mathrm{N\,m\,s/rad}$
c (Coulomb level)	$0.003498\ \mathrm{N\,m}$
d (Stribeck amplitude)	$0.002423\ \mathrm{N\,m}$
ω_s (Stribeck speed)	$0.08581\ \mathrm{rad/s}$
I (estimated inertia)	$0.32241\ \mathrm{kg\,m^2}$

The joint fit produced a low overall error, with an RMSE of $0.276\ \mathrm{rad/s^2}$, which means the model matches the measured angular acceleration reasonably well across all runs. The Jacobian condition number, $\mathrm{cond}_2(J) = 241$, is moderate and indicates that the optimization problem is not overly sensitive or ill-conditioned. The solver also reported full rank (5/5), showing that all parameters including the inertia were independently identifiable from the dataset.

The maximum parameter correlation (about 0.88) is relatively high but still acceptable for this type of nonlinear friction model, where some coupling between the viscous term and inertia is expected. Overall, the optimization behaved well and converged cleanly, giving a consistent set of friction parameters together with a realistic estimate of the platform's aggregate inertia which will be verified against analytical inertia calculations.

5.3. Analytical Bottom-Up Inertia Estimation

To complement the experimentally estimated inertia obtained from the nonlinear least-squares friction model, a separate analytical "bottom-up" inertia calculation was carried out. Each structural component of the hub assembly was modeled individually using standard geometric inertia expressions, together with simplifying assumptions tailored to each part (e.g. idealized plate thickness, uniform density approximations, neglecting minor features). The individual contributions were then summed to obtain the analytical estimate of the total inertia. Table 5.6 summaries the modeling assumptions and resulting inertia.

Table 5.6: Bottom-up analytical estimation of the hub and structure inertia.

Part	**Assumptions / Notes**	**Inertia [kg m^2]**
Bearing Plate	Height treated separately from thickness; mass computed from CAD	0.001170
Bottom Plate	Height not equal to plate thickness; mass adjusted accordingly	0.000166
Top Plate	Height not equal to physical thickness; simplified geometry used	0.0936
Battery	Standard block approximation with measured mass	0.0180
Electronics / Switches	Treated as lumped mass elements	0.00355
Counterweights (pos. and neg. y)	Modeled as point masses at measured offsets	0.0972
Electronics Block	Lumped solid block with uniform density	0.0277
Reaction Wheel Assembly	Includes flywheel, support rods, plates, and motor	0.07876
Bolts, Screws, Washers	Small masses; off-axis distances neglected for balance hardware	0.01095
Water Jug	Modelled as axisymmetric empty container with measured fill level	0.01322
Total Inertia	sum of above	**0.343**

The analytical bottom-up procedure yields a total inertia of $I_{\text{total, ana}} = 0.343268\ \text{kg}\,\text{m}^2$. This value is close to the inertia estimated from the joint nonlinear least-squares friction fit, which returned $I_{\text{total, est}} =$

$0.322414\ \mathrm{kg\,m^2}$. The relative difference between both estimates is approximately

$$\frac{I_{\text{total, ana}} - I_{\text{total, est}}}{I_{\text{total, ana}}} \approx 6\%.$$

Given the nonlinear nature of the friction fit and the simplified geometric assumptions required for the analytical approach, this level of agreement is considered good and supports the consistency of the overall model.

The remaining discrepancy can be attributed to several practical factors. First, the analytical estimate relies on idealized geometries and uniform density assumptions for each component, and minor features such as wiring, connectors, small brackets, and local cut-outs are either neglected or only approximately captured. Second, the real mass distribution may differ slightly from CAD-based values due to manufacturing tolerances and assembly choices. Finally, the experimental inertia emerges as an aggregate effective inertia seen through the bearing and drivetrain, meaning that unmodeled compliance, small misalignment's, or residual friction nonlinearities can bias the fitted inertia slightly. Overall, the two estimates are in agreement: the bottom-up inertia provides a physics-based baseline, while the joint fit provides an experimentally grounded inertia that can be used for future simulations.

5.4. Preferential direction

During assembly and operations of the platform, especially under high load, it was noticed that the platform exhibited a "preferential direction". As this caused concern since it is an unmodeled disturbance a characterization test was defined. To the platform with an empty tank a square–wave impulse in both clockwise (CW) and counterclockwise (CCW) directions is applied. Following each impulse, the platform was allowed to freely decay while the body–frame angular rate $\omega_Z(t)$ was recorded using the IMU, together with angular displacement θ and wheel/motor telemetry used to exclude intervals with any non-negligible applied torque. The angular displacement was obtained utilizing an optical encoder that became available on the platform towards the end of the thesis.

To plot the decay rate against the angular position the angular acceleration was obtained from the IMU rate measurement using a central finite-difference approximation,

$$\alpha_Z(k) \;\approx\; \frac{\omega_Z(k{+}1) - \omega_Z(k{-}1)}{2\,\Delta t},$$

where Δt is the sampling period. Free decay segments were isolated by selecting intervals in which the sign and magnitude of ω_Z were consistent with purely passive CW or CCW motion and in which the estimated drive torque was effectively zero.

To evaluate whether the braking acceleration depends on angle and whether it differs between CW and CCW motion, a smooth periodic model to the raw (θ, α) data for each direction. The model takes the form

$$\alpha(\theta) \;\approx\; \beta_0 \;+\; \sum_{h=1}^{H} \Big[\beta_h^{(s)} \sin(h\theta) + \beta_h^{(c)} \cos(h\theta)\Big],$$

with a small number of harmonics H sufficient to capture periodic structure in the braking profile while remaining robust to sensor noise. The coefficients were estimated using ordinary least squares. The CW and CCW data where separated allowing any directional asymmetry to be revealed directly. The results for this raw plotting and fitting are shown in Figure 5.10.

Model quality was assessed using the root-mean-square error (RMSE) in physical units of rad/s^2 and the coefficient of determination R^2, computed relative to the instantaneous variance of the raw acceleration samples. Because the raw IMU data include measurement noise and short transients, the resulting R^2 values are intentionally conservative; nonetheless, clear separation between the fitted CW and CCW curves provides strong evidence of genuine directional preference. The asymmetrical decay rate is shown in Figure 5.12 which is a polar representation of the fitted braking profiles $\alpha_{\mathrm{CW}}(\theta)$ and $\alpha_{\mathrm{CCW}}(\theta)$ and tha directional asymmetry curve $\Delta\alpha(\theta) = \alpha_{\mathrm{CCW}}(\theta) - \alpha_{\mathrm{CW}}(\theta)$ plotted in Figure 5.11, which directly quantifies the angle-dependent preferential behavior.

The analysis shows that indeed there is a preferential direction in the Clockwise Direction, this is seen in Figure 5.11 which has a positive magnitude over the whole revolution. This means that for a given position the CCW motion experiences stronger breaking than the CW motion. Therefore the platform ”prefers” to rotate in the clockwise direction since it offers less resistance. The deceleration is stronger at $\pm\pi$, since the encoder is not absolute but is relative this suggest that in an entire rotation half of the rotation the platform experiences larger deceleration than in the other half. This effect is nicely visualized in Figure 5.12 providing a birds eye view on the deceleration of the platform..

Overall this preferential direction is thought to occur due to misalignment in construction and due to unbalances within the platform. A strong point towards unbalancing is the fact that this effect is most visually noticeable when the long flexible beam with a mass towards the end is mounted on the platform (for IOANT experiments). Unfortunately, while this effect has been identified and somewhat characteristic it was not corrected for in the model fitting due to time constraints within the thesis.

5.5. Allan Variance Test

To characterize the stochastic properties of the IMU, z–axis rate signal for noise identification the IMU was left turned on to record during the course of a night as seen in Figure 5.13. The raw data was detrended to remove any constant bias, and expressed with absolute clock time to confirm continuity. A representative stationary window from 01:30 am to 05:00 am was then selected by cropping a long interval of near-zero mean rotation, ensuring that the data used for noise analysis corresponded to a steady operating condition.To ensure that the IMU data used for the Allan variance identification were sufficiently stationary and well-behaved, several diagnostic checks were performed.

Normality was evaluated using both a Q–Q plot (Figure 5.14) and a histogram with a standard normal overlay (Figure 5.15). While the Kolmogorov Smirnov test formally rejects Gaussianity, the empirical distribution follows the bell-shaped curve closely. The deviation is largely explained by strong quanti-

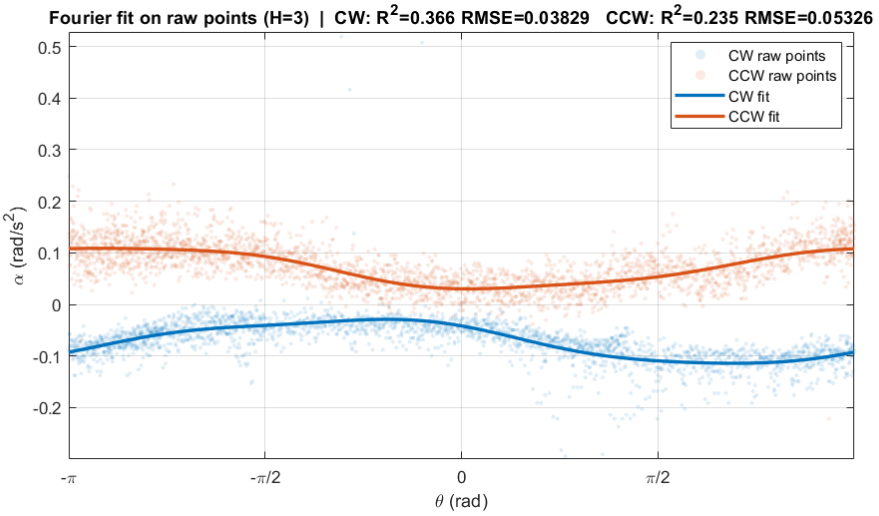

Figure 5.10: Raw scatter plot of clockwise and anticlockwise data

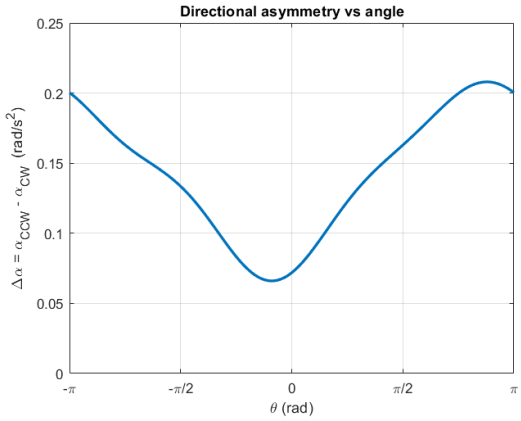

Figure 5.11: Directional asymmetry vs angle

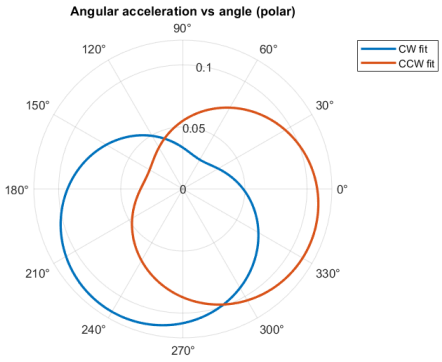

Figure 5.12: Preferential direction polar plot

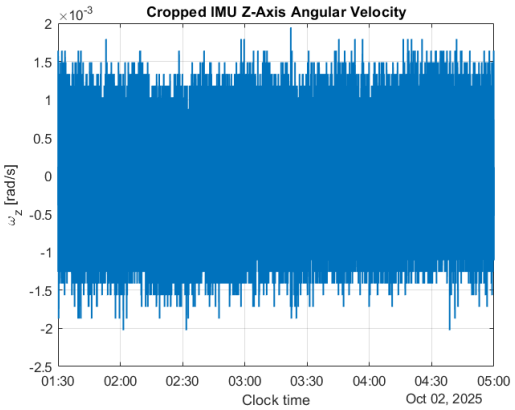

Figure 5.13: Raw IMU z-axis data from night run

zation, which was quantified at a very high level (QNR ≈ 831), indicating that discrete output levels dominate the fine-scale structure of the noise.

To verify temporal stability, the data were divided into fourteen consecutive 15-minute chunks. The chunked means (Figure 5.16) remain very close to zero and show no systematic drift, and the chunked variances (Figure 5.17) remain tightly grouped with only small-scale fluctuations. Together these results indicate that the underlying noise level is essentially constant over the entire dataset.

The normalized autocorrelation function (Figure 5.18) shows no significant correlation beyond lag zero, with all side-lobes remaining small and non-persistent. This supports the interpretation that the detrended residuals can be treated as effectively white for the purposes of Allan-variance-based noise identification.

Finally, the Allan deviation itself (Figure 5.19) reflects these observations. The fitted Angle Random Walk level, $N \approx 5.75 \times 10^{-5}\,\mathrm{rad/s}/\sqrt{\mathrm{Hz}}$, matches the short-term slope of the measured curve, while the identified bias-instability plateau, $B \approx 5.21 \times 10^{-5}\,\mathrm{rad/s}$, is consistent with the mid-range flattening. The noise level recorded during the experiment is

Overall, despite the presence of strong quantization, the chunked statistics, autocorrelation structure, and histogram collectively indicate that the IMU residuals behave sufficiently like white noise for the Allan variance analysis to yield meaningful and interpretable parameters.

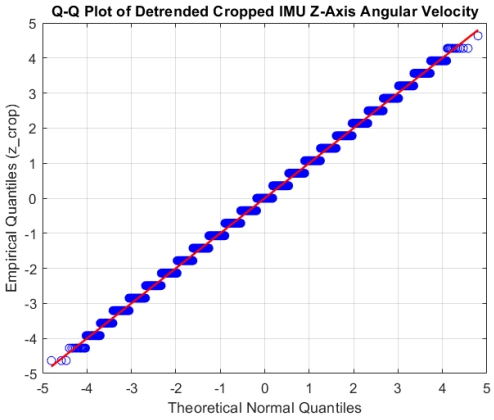

Figure 5.14: Q-Q allen variance plot

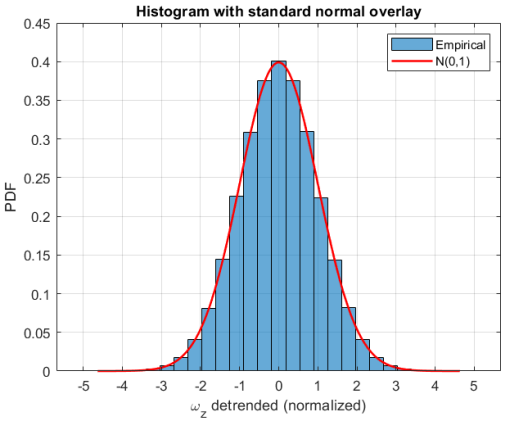

Figure 5.15: Allen Variance data histogram vs normal curve

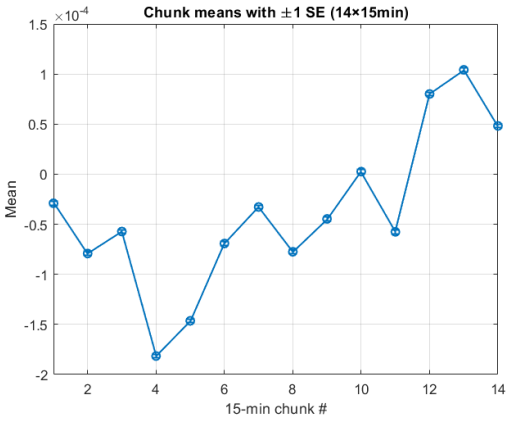

Figure 5.16: Allen variance chunked mean distribution plot

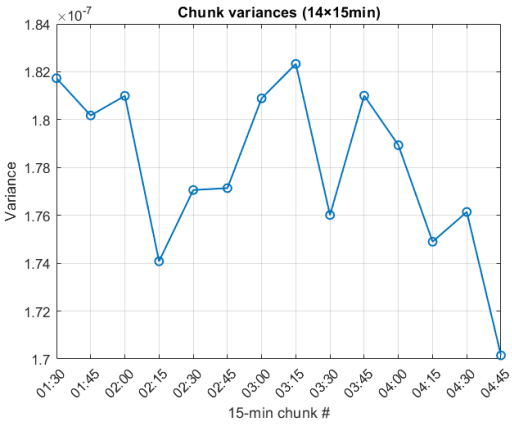

Figure 5.17: Allen Variance chunked variance plot

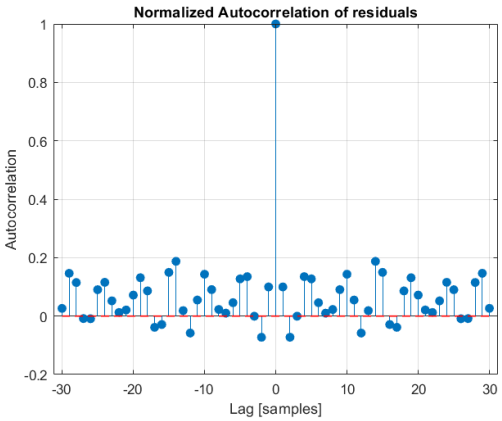

Figure 5.18: Allen Variance test autocorrelation plot

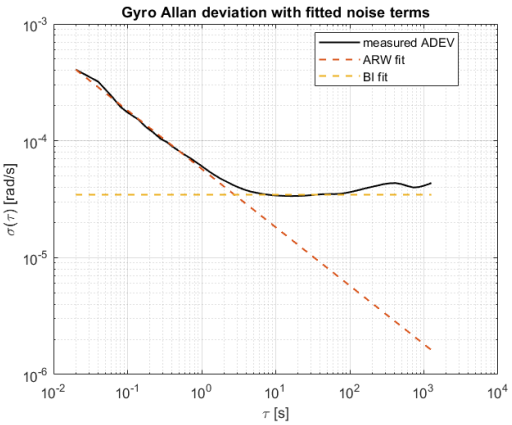

Figure 5.19: Gyroscope Deviation Allen Variance

6

Model Matching Methodology

In this chapter model matching techniques that where explored during the thesis are presented along with the final analysis methodology employed and a presentation of results. Description of the synthetic data generation setup that was used as a baseline to compare experimental data has also been included.

6.1. Model matching techniques

During the thesis two main model matching techniques where utilized, the first time domain matching, had a significant amount of time invested into it but unfortunately yielded little results due to not being robust. For time domain matching two techniques where utilized, nonlinear least squares and matlabs grayest function. The second method explored which is then the method utilized to estimate the results is frequency matching through the use of the tfest function, a guiding diagram for convenience is found in Figure 6.1. These method have been taken and inspired by similar methods found in [27] book.

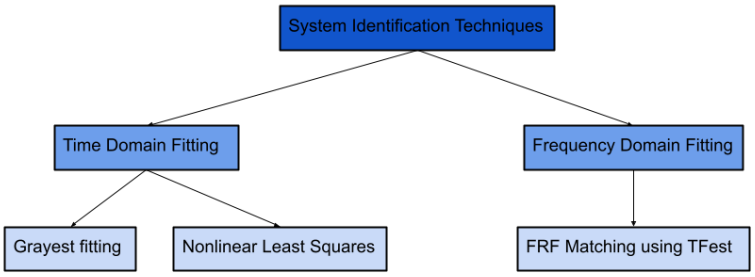

Figure 6.1: Outline of system identification techniques attempted during the thesis

6.1.1. Nonlinear Least-Squares Identification Procedure

A NLLS estimator was used to identify the tank geometry parameters (d, h) directly from the measured hub-rate $\theta_z(t)$. The model is the linearized hub sloshing system, which predicts $\hat{\theta}_z(t)$ given an applied torque input. This was done first with the friction represented by the term "b" as shown in equations of motion that where derived in section 4.4, and the equations where expanded to include the identified nonlinear friction using the same technique previously explained $\tau_{\text{act}}(t) = \tau_{\text{cmd}}(t) + \tau_{\text{fric}}(t)$.

To include nonlinear friction while preserving the liner structure, the commanded wheel torque signal was first augmented with the estimated nonlinear friction model. The instantaneous (experimental) hub-rate measurement $\omega_z(t)$ was used to evaluate a Stribeck-type friction law[8],

$$\tau_{\text{fric}}(t) = -\Big(b\,\omega_z(t) + \text{sign}(\omega_z(t))\Big[c + d\,e^{-(|\omega_z(t)|/w_s)^2}\Big]\Big) \tag{6.1}$$

which incorporates viscous drag (b), Coulomb friction (c), and a breakaway term, the precise values of this where estimated utilizing a nonlinear LS from the platform. The values of which where previously estimated utilizing a separate NLLS. This torque opposes motion and is added directly to the command input, yielding an "effective" actuation signal

$$\tau_{\text{act}}(t) = \tau_{\text{cmd}}(t) + \tau_{\text{fric}}(t),$$

which captures the dominant nonlinearities known to affect the hub. The resulting excitation more faithfully represents the torque delivered to the fluid–structure system.

The initial idea was to estimate the d (diameter) and h fill level of the tank being tested, the rationale being that if the estimated tank diameter and fluid fill level fit the experimentally measured tank diameter it would be indicative that the model matching had been successful. It was expected that the matching between d and h grow worse as the experimental results become more nonlinear and that those nonlinearities could be detected in the residuals.

The unknown parameters d and h were estimated by simulating the model response $\hat{\theta}_z(t)$ under $\tau_{\text{act}}(t)$ and minimizing the time-domain error between simulated and measured rates. To improve numerical conditioning, the optimization was performed in a transformed parameter space using two invariant combinations of (d, h), while enforcing simple bounds that map back to physically reasonable tank sizes.

At each iteration, the model is rebuilt using the candidate parameters, the hub-rate response is simulated, and the residuals

$$r_i = \hat{\theta}_z(t_i) - \theta_z(t_i)$$

are passed to the `lsqnonlin` solver. This routine adjusts the parameters to minimise the squared residuals and returns the best-fit values along with the Jacobian, which is used to assess parameter uncertainty and correlation. `lsqnonlin` is a verified function present in MATLAB 2025b.

The nonlinear LS showed promising results when applied initially to the equations of motion with only viscous friction. It demonstrated itself to be moderately resistant to initial guesses, as illustrated by a short sensitivity analysis in Figure 6.2 and Figure 6.3, and to noise, being able to reliably reconstruct tank diameter and fill level from noisy synthetic data.

A simple one-at-a-time sensitivity sweep was carried out to assess how the estimator responds to different initial guesses. First, the diameter d was fixed while the initial height h_0 was varied (Figure 6.3), and then the height h was fixed while the initial diameter d_0 was swept (Figure 6.2). For each run, the fit quality, Jacobian conditioning, parameter correlation, and recovered parameter values were recorded.

The results of the sensitivity analysis (Figure 6.2, Figure 6.3) shows a clear asymmetry: the height h is easy to identify, with good fits and stable conditioning across a wide range of initial guesses. In contrast, the diameter d is much more sensitive, and only reasonable initial guesses lead to stable convergence. This indicates that, while the method can reliably recover the liquid height even from poor starting points, the diameter requires a closer initial approximation to avoid ill-conditioning and parameter drift.

The NLLS yielded decent results for the simple viscous friction, however when the nonlinear friction was introduced its robustness sharply declined and the NLLS no longer could accurately recreate the tank characteristic dimensions d and h. This was due to the instabilities introduced by the nonlinear friction calculated from ω_z. The specific reasons for these instabilities will be further explored in the following section subsection 6.1.2.

6.1.2. Grey-Box Model Matching

Time-domain model matching was performed using MATLAB's `greyest` framework which is a validated tool part of MATLAB 2025b [30]. A continuous-time grey-box model was constructed from the analytical equations of motion, resulting in a four-state system

$$\dot{x}(t) = A(\theta)\, x(t) + B(\theta)\, \tau_{\mathrm{act}}(t), \qquad y(t) = C(\theta)\, x(t),$$

where $x = [\theta,\, \alpha,\, \dot{\theta},\, \dot{\alpha}]^{\top}$, and θ denotes the vector of parameters to be estimated. The model captures the coupled hub–sloshing dynamics with a single slosh mode, including the effective inertia I_{eff} and damping ratio ζ. In the identification procedure, physically known parameters (e.g. hub inertia I_{hub}) were held fixed, while selected parameters such as the slosh damping ζ and the input gain g_τ were marked as free. Optional gains (e.g. output scale g_y) were fixed to unity when sensor calibration was trusted.

The `greyest` routine performs prediction-error minimization against the measured time-series data $\{\tau_{\mathrm{act}}(t), \omega_z(t)\}$ [30]. An initial state is estimated automatically, and a continuous-time parameter update is carried out under stability constraints. Because the model structure is derived directly from the governing equations, the identified parameters preserve physical interpretability while ensuring that the simulated output $\hat{\omega}_z(t)$ matches the measured signal as closely as possible under the enforced dynamics.

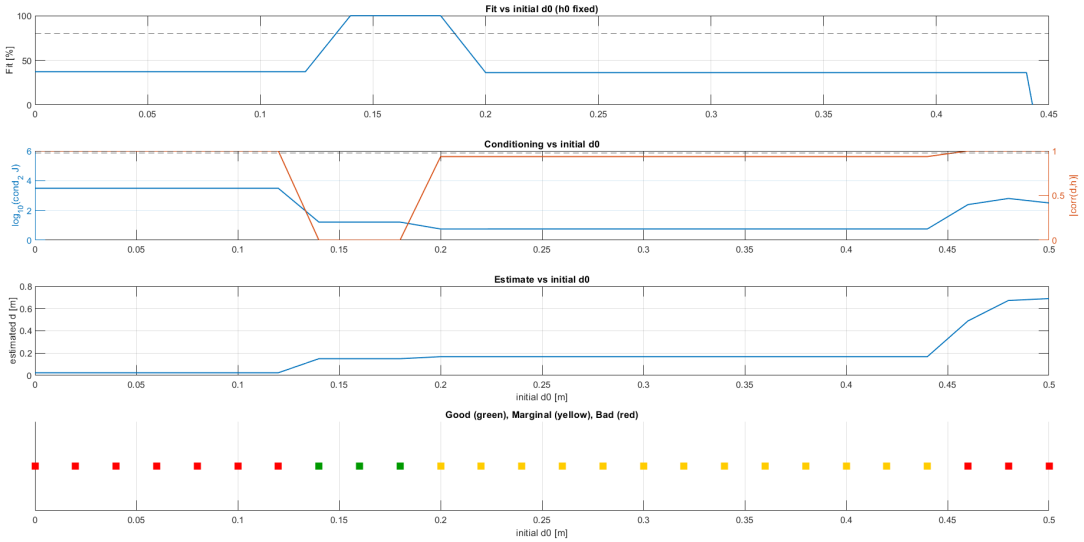

Figure 6.2: Sensitivity analysis sweep over d with simple viscous friction NLLS

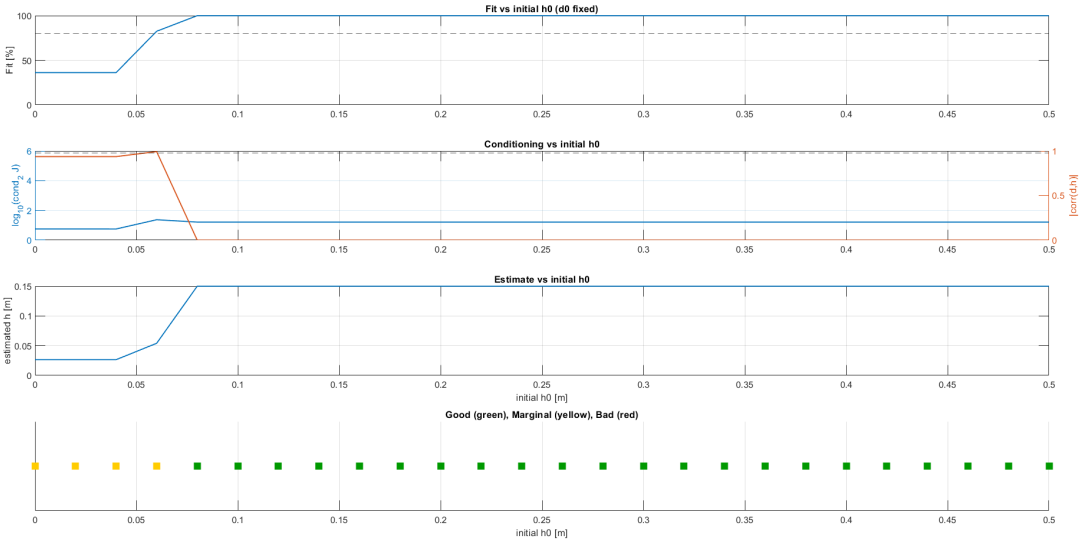

Figure 6.3: Sensitivity analysis sweep over h with simple viscous friction NLLS

The grayest time domain matching was incrementally tested by allowing it to match synthetic clean, noisy and experimental data. This is primarily done to check the robustness of introducing nonlinear friction through u_{actual} in the platform. Matching of clean synthetic data yields a 71.1% match, noisy synthetic yields a 46.28% match and unfortunately experimental data yields a match of -520.9%. The equivalent bode plot resulting from the matches transfer function are shown for the noisy synthetic data Figure 6.4 and for experimental data Figure 6.5, as can be seen in those figures the matching of the resonance and anti-resonance in the experimental magnitude plot is weak, missing both the peak and the dip, the same thing can be seen in the phase plot Figure 6.5.

The decrease in fit % is to be expected, as the nonlinear friction is dependent on ω_z any noise associated with the angular position is dragged into the estimation, this becomes a particular problem given the formulation of Equation 6.1, it contains a sign operator, when the angular velocity is at very low speeds this constantly flips between positive and negative rendering the soltuion unstable. Secondly any bias that is left over from ω_z measurement will be dragged into the estimation causing it to accumulate over time. This can be seen when plotting the fitted function over the original experimental plot, in the beginning matching is quite good but it decreases further on in the experiment.

Several techniques where tried to improve the matching of results utilizing grayest, a dead band to the nonlinear friction was included (excluding low speed results) and a 2nd order butters-worth lop pass filter was also added, however while both of these solutions improved the stability of the solution it still matched at several hundreds of negative % points for the experimental cases, which resulted in time domain matching unfortunately not being a realistic possibility.

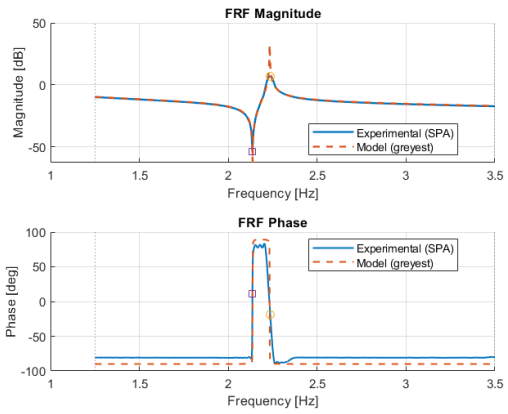

Figure 6.4: Bode plot overlaying matched noisy synthetic data with FRF

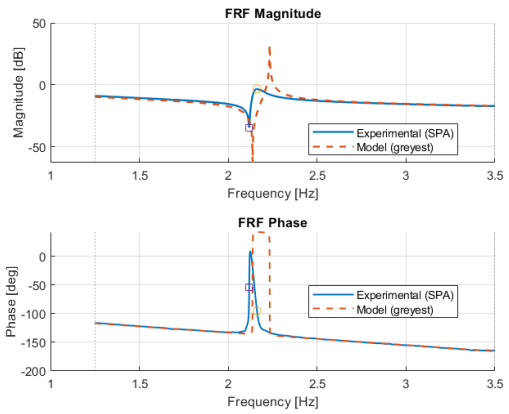

Figure 6.5: Bode plot overlaying matched experimental data with FRF

Given these results, the most reasonable next step would have been to formulate a fully nonlinear ODE model incorporating the friction law directly and perform nonlinear time-domain parameter estimation. This approach was attempted, but the resulting optimisation problem proved to be prohibitively computationally expensive for repeated identification over multiple runs as single runs took upwards of 4-5 hours, this is due to the large amount of points necessary to match, at an IMU sampling rate of 50Hz

this results in a single timestep of 0.02s, with experiments lasting 2750 seconds this yields 137500 individual points to be matched. The linear time domain methodology exploiting state space representation was preferred as it allowed for much more rapid data matching.

6.1.3. Frequency Domain matching

To characterize the hub sloshing dynamics in a compact and repeatable way, the input–output behavior was analyses directly in the frequency domain. The commanded wheel torque $\tau_{\mathrm{cmd}}(t)$ served as the input, and the debased hub angular rate $\omega_z(t)$ was taken as the output. After bias-removal and trimming to the active portion of the swept-sine experiment, the data were placed into an `iddata` object and a nonparametric frequency-response estimate was obtained using the `spa` method [49]. This produced a complex FRF Equation 6.2 evaluated on a logarithmic grid spanning 1.25–$3.5\,\mathrm{Hz}$.

$$H_{\mathrm{exp}}(j\omega) = \frac{\Omega_z(j\omega)}{_{\mathrm{cmd}}(j\omega)} \tag{6.2}$$

From the FRF, the principal dynamical features the resonance peak f_{res}, the notch or anti-resonance frequency f_{dip}, and the associated notch depth were extracted directly from the magnitude curve. These quantities give an immediate indication of the amplitude dependent behavior of the sloshing mode and are used later to interpret model variations.

To obtain a compact parametric representation suitable for simulation and comparison, the measured FRF was matched to a rational transfer function using MATLAB's `tfest` routine [50]. The `tfest` algorithm performs a frequency-domain prediction-error optimization: given a specified model order, it searches for the transfer function whose frequency response best fits the nonparametric FRF in a weighted least-squares sense [50]. The method internally constructs an initial estimate via subspace-based linear regression and then refines the pole zero parameters using a nonlinear optimization step. In this work a model with three poles and two zeros (plus an optional input–output delay T_d) was enforced, consistent with the structure implied by the final equations of motion [50]. A distinct advantage of utilizing tfest is that it is validated as a math works tool in MATLAB version 2025b.

The resulting model $H_{\mathrm{mod}}(s)$ was evaluated on the same frequency grid as $H_{\mathrm{exp}}(j\omega)$ to enable point wise comparison of magnitude and phase. This provided a concise and physically interpretable representation of the system dynamics, while ensuring that the fitted poles, zeros, and delay remained consistent with the experimentally observed frequency domain behavior.

Rationale for a Three-Pole, Two-Zero Model

The selected $(3, 2)$ structure follows directly from the linearized coupled equations of motion of the hub sloshing system. Using the pendulum form slosh model and hub torque balance derived in section 4.4, the governing equations are

$$\ddot{\alpha} + 2\zeta\omega_n\dot{\alpha} + \omega_n^2\alpha = -\frac{r}{\ell}\ddot{\theta}, \tag{6.3}$$

$$I_{\text{eff}}\ddot{\theta} + b\dot{\theta} + r\Big(m_s g\,\alpha + 2m_s\zeta\omega_n\ell\,\dot{\alpha}\Big) = \tau_{\text{cmd}}, \tag{6.4}$$

where $I_{\text{eff}} = I_{\text{dry}} + m_0 r^2$ is the rigid inertia seen at the hub axis.

Taking Laplace transforms with zero initial conditions gives

$$\big(s^2 + 2\zeta\omega_n s + \omega_n^2\big)(s) = -\frac{r}{\ell}s^2\Theta(s), \tag{6.5}$$

$$\big(I_{\text{eff}}s^2 + bs\big)\Theta(s) + r\big(m_s g + 2m_s\zeta\omega_n\ell\,s\big)(s) =_{\text{cmd}} (s). \tag{6.6}$$

Solving (6.5) for (s) and substituting into (6.6) yields a single input output relation in $\Theta(s)$:

$$\Theta(s)\left[I_{\text{eff}}s^2 + bs - \frac{r^2}{\ell}s^2\frac{m_s g + 2m_s\zeta\omega_n\ell\,s}{s^2 + 2\zeta\omega_n s + \omega_n^2}\right] =_{\text{cmd}} (s).$$

Multiplying through by the slosh denominator produces a third-order polynomial in the hub coordinate:

$$\Theta(s)\left(a_3s^3 + a_2s^2 + a_1s + a_0\right) =_{\text{cmd}} (s)\left(s^2 + 2\zeta\omega_n s + \omega_n^2\right),$$

where the coefficients a_i are determined by I_{eff}, b, m_s, r, ℓ, ζ, and ω_n. Differentiating to form the measured output $\Omega_z(s) = s\Theta(s)$ gives

$$H(s) \triangleq \frac{\Omega_z(s)}{\text{cmd}(s)} = \frac{s\big(s^2 + 2\zeta\omega_n s + \omega_n^2\big)}{a_3s^3 + a_2s^2 + a_1s + a_0}. \tag{6.7}$$

Equation (6.7) is explicitly a three pole, two zero transfer function: the denominator is cubic due to the coupled hub sloshing second order mode plus hub inertia, while the numerator is quadratic from the sloshing mode dynamics, with an additional factor of s introduced by the rate output. This structure therefore matches the physics of the final equations of motion and motivates the use of a $(3, 2)$ model order in the frequency domain identification. The anti-resonance (initial dip in the data) is given by the zeros of the equations, the poles are the associated with resonance (peak in the FRF).

6.2. Synthetic Dynamics Model and Data Generation Procedure

In order to verify that the model matching is working as intended a synthetic data generator was created. This generator utilizes the linear coupled equations of motions that where previously derived along with the inclusion of the previously estimated nonlinear friction and inertia to produce results for a simulated platform. This simulated platform can necessarily only produce linear results as it has been constructed with a linear model.

This section describes the mathematical formulation and numerical procedure used to generate the synthetic hub–liquid motion dataset. The synthetic data are produced by integrating a coupled nonlinear ODE that includes rigid-body hub dynamics, a first sloshing mode of the liquid payload, and a nonlinear Stribeck-type bearing friction model.

6.2.1. Dynamic (synthetic) Model

The system state is

$$x = \begin{bmatrix} \theta \\ \alpha \\ \dot{\theta} \\ \dot{\alpha} \end{bmatrix},$$

where θ is the hub angular position, $\dot{\theta}$ is the angular velocity, α is the internal sloshing pendulum angle and $\dot{\alpha}$ is the slosh pendulum angular velocity. The rigid-body inertia of the hub is fixed to the identified value $I_{\text{hub}} = 0.322414\ \text{kg}\,\text{m}^2$.

Slosh-mode dynamics

The liquid dynamics follow the standard linearised single-mode model of a partially filled cylindrical tank. The effective modal mass m_s, frozen mass m_{frozen}, and coupling parameter γ are computed directly from the tank geometry and the first antisymmetric root $\xi = 1.841$. The mode length and natural frequency are

$$l = \frac{d}{2\xi \tanh(2\xi h/d)}, \qquad \omega_n = \sqrt{\frac{g}{l}},$$

where d is the tank diameter and h is the fill height. Viscous damping ζ is computed using the Reynolds-number-based expression appropriate for shallow fills. The slosh mode contributes both a restoring torque and a velocity-dependent coupling term to the hub dynamics.

Hub dynamics and effective inertia

The effective rotational inertia seen by the hub is

$$I_{\text{eff}} = I_{\text{hub}} + m_{\text{frozen}} r^2,$$

where r is the radial distance from the hub centre to the tank. The linear plant matrices for the coupled system are

$$\dot{x} = Ax + B\tau_{\text{net}},$$

where A and B contain the slosh stiffness, damping, and hub–slosh coupling terms.

6.2.2. Nonlinear Bearing Friction Model

The net torque acting on the hub is the commanded torque plus the nonlinear friction torque,

$$\tau_{\text{net}}(t) = \tau_{\text{cmd}}(t) - \Big(b\,\dot{\theta} + \text{sgn}(\dot{\theta})\big(c + d\,e^{-(|\dot{\theta}|/w_s)^2}\big)\Big),$$

with parameters (b, c, d, w_s) set to the experimentally identified values. A hard or smoothed sign function is used depending on solver behaviour:

$$\text{sgn}_\varepsilon(\omega) = \tanh\Big(\frac{\omega}{\varepsilon}\Big).$$

6.2.3. Numerical Integration and Resampling

The synthetic data generation proceeds as follows:

1. The experimental torque command $\tau_{\mathrm{cmd}}(t)$ is trimmed to the desired time window and converted into a continuous function using a `griddedInterpolant`.
2. The full nonlinear ODE
$$\dot{x}(t) = f\big(x(t), \tau_{\mathrm{cmd}}(t)\big)$$
is integrated once over the entire time horizon using `ode45` with moderately strict tolerances (`RelTol = 1e-5`, `AbsTol = 1e-7`).
3. The continuous-time solution $(t_{\mathrm{sol}}, x(t))$ is resampled onto the exact experimental time grid T using shape-preserving cubic interpolation (`pchip`) to ensure that the synthetic data can be used directly in the parameter-estimation framework.

6.2.4. Optional Measurement Noise Injection

To emulate a realistic IMU, white rate noise may be added to the angular-rate channel after integration. The per-sample noise level is derived from the measured angle-random-walk density (approximately $3.3\ \mathrm{mdps}/\sqrt{\mathrm{Hz}}$). The final outputs written to file are:

$$\{\, t,\ \tau_{\mathrm{cmd}},\ \dot{\theta},\ \alpha,\ \dot{\alpha}\,\}.$$

This procedure yields a complete synthetic dataset that is dynamically consistent, includes nonlinear friction and fluid coupling, and is sampled exactly like the real experiment.

6.3. Data Analysis techniques employed

In the previous two sections the methods for model matching and synthetic data generation where shown. In this section the different tests and techniques applied to both the raw data and the matched functions in order to determine if the nonlinearities are present in the movement of the fluid. The data to be analyzed from this section comes form the IMU mounted to the platform. Primarily sloshing is measured only through the angular velocity reading around the Z axis. While the platform is constrained around this axis angular velocity data is still available around the X and Y axes of rotation. Qualitative data is also recorded for each run with notes taken on the visual liquid behavior during the runs as well as video material being available.

6.3.1. FRF Feature Extraction: f_{res}, f_{dip}, Δf, and Notch Depth

The identification of the key frequency-domain features was performed directly on the nonparametric FRF obtained using the Spectral Analysis with Averaging (spa) estimator [49]. The spa method was applied to the trimmed and debiased input output data using a logarithmically spaced frequency grid covering the excitation range of interest. Throughout this work, the analysis band corresponds to the

sweep range 1.25–3.5 Hz, and the FRF is windowed to this interval prior to feature extraction. FRF of sloshing modes has been utilized in other sources such as [4] in the identification of resonant and anti resonant frequencies from time domain data.

The complex FRF is converted to a magnitude spectrum in decibels using

$$M(f) = 20\log_{10}(|H(j2\pi f)|)\,, \tag{6.8}$$

where $H(j\omega)$ is the estimated FRF.

Within the in-band magnitude spectrum, the resonance frequency is identified as

$$f_{\text{res}} = \underset{f\,\in\,[f_{\min},\,f_{\max}]}{\arg\max}\; M(f), \tag{6.9}$$

and the anti-resonance (or notch) frequency is defined as

$$f_{\text{dip}} = \underset{f\,\in\,[f_{\min},\,f_{\max}]}{\arg\min}\; M(f). \tag{6.10}$$

The frequency spacing between the two features is

$$\Delta f = f_{\text{res}} - f_{\text{dip}}, \tag{6.11}$$

which serves as a sensitive indicator of amplitude-dependent nonlinearities. For a linear system, Δf remains constant across input amplitudes. In contrast, fluid sloshing introduces an amplitude-dependent effective stiffness, producing measurable shifts in f_{res}, f_{dip}, and therefore Δf. The identified f_{res} and f_{dip} are shown on in Figure 6.6 in both the magnitude and bode plot.

The notch depth quantifies the strength of modal cancellation between the rigid-body mode and the sloshing mode:

$$D_{\text{notch}} = M(f_{\text{res}}) - M(f_{\text{dip}}), \tag{6.12}$$

expressed in decibels. A deeper notch corresponds to stronger coupling between the dominant modes, while a shallower notch at higher amplitudes indicates detuning effects typical of nonlinear fluid–structure interactions.

6.3.2. Model Fit Metrics in the Time and Frequency Domains

The agreement between the identified linear transfer function and the measured system response is quantified using two complementary fit metrics: a time-domain fit percentage and a frequency-domain fit percentage.

Let $y(t)$ denote the measured angular rate, and $\hat{y}(t)$ the model output produced by simulating the identified transfer function using the same input signal. The time-domain residual is

$$e(t) = y(t) - \hat{y}(t). \tag{6.13}$$

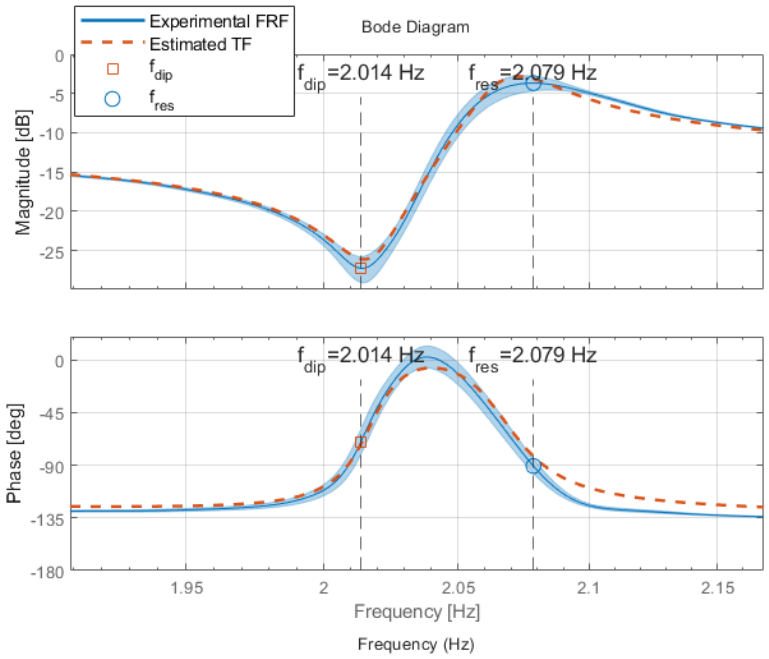

Figure 6.6: FRF with f_{res} and f_{dip} identified

The time-domain fit percentage is defined using a normalised root-mean-square error (NRMSE):

$$\mathrm{Fit}_{\mathrm{time}} = 100\left(1 - \frac{\|e(t)\|_2}{\|y(t) - \overline{y}\|_2}\right), \tag{6.14}$$

where $\overline{y}$ is the sample mean of the measured output.

A second metric compares the complex FRF produced by the identified model to the nonparametric SPA estimate. Let $H_{\mathrm{meas}}(j\omega_k)$ and $H_{\mathrm{mod}}(j\omega_k)$ denote the measured and model FRFs evaluated at identical frequency points. The frequency-domain fit is then computed as

$$\mathrm{Fit}_{\mathrm{freq}} = 100\left(1 - \frac{\|H_{\mathrm{meas}} - H_{\mathrm{mod}}\|_2}{\|H_{\mathrm{meas}} - \overline{H}_{\mathrm{meas}}\|_2}\right), \tag{6.15}$$

where $\overline{H}_{\mathrm{meas}}$ is the complex mean of the in-band FRF.

A reduction in either metric with increasing amplitude indicates that the linear model no longer captures the dominant dynamics, signaling the presence of amplitude-dependent nonlinearities induced by the fluid motion.

6.3.3. Residual Input Coherence Estimation

The coherence between the model residual and the input torque provides insight into how much of the remaining output measurement is linearly correlated with the input after model removal. It is defined in the frequency domain as

$$\gamma^2_{eu}(f) = \frac{|S_{eu}(f)|^2}{S_{ee}(f)\, S_{uu}(f)}, \tag{6.16}$$

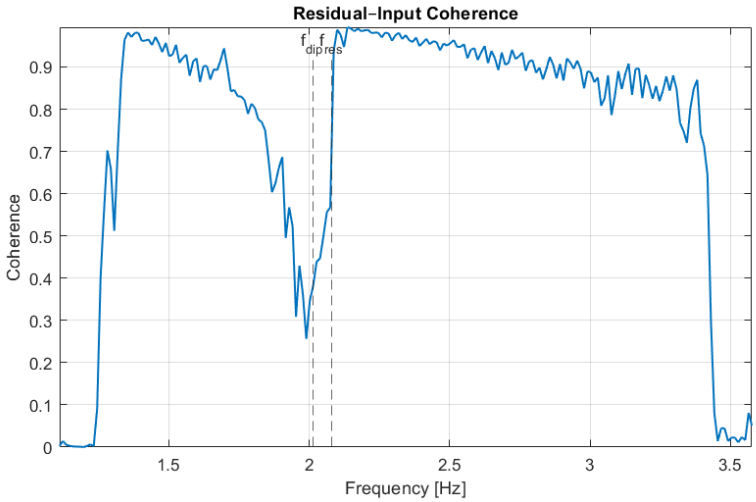

Figure 6.7: Residual - Input Coherence plot for 10cm sweep 0.05Nm amplitude

where $S_{eu}(f)$ is the cross-power spectral density (CPSD) of the residual $e(t)$ and the input $u(t)$, and $S_{ee}(f)$ and $S_{uu}(f)$ are their respective power spectral densities. An example of what the residual-input coherence plot looks like for the example case with fill level 10cm under an excitation of 0.05Nm Figure 6.7. Coherence has been used in other works such as "Experimental modal analysis of a water-filled circular cylindrical tank" [4] where coherence was used to support the identification of sloshing modes under excitation.

The spectral quantities are estimated using Welch's method with Hamming windows and 50% overlap. To summarise coherence within the dynamically relevant region between f_{res} and f_{dip}, a band-averaged quantity is computed as

$$\overline{\gamma}^2_{eu} = \frac{1}{N_b} \sum_{f \in [f_{\text{lo}},\, f_{\text{hi}}]} \gamma^2_{eu}(f), \tag{6.17}$$

where N_b is the number of frequency bins in the interval.

In this work, the coherence is computed between the model residual $e(t)$ and $u(t)$. Coherence between residuals and inputs has been used in other works (not strictly sloshing related) such as [39]. Because the residual represents the portion of the measurement not captured by the linear model, low coherence implies that the residual contains only noise like components that are uncorrelated with the input. This situation should occur predominantly at low excitation amplitudes, where the system behaves linearly and the identified model explains nearly all of the input–output dynamics.

As the excitation amplitude increases, the fluid motion is expected to become increasingly nonlinear and the linear model fails to capture a growing portion of the dynamics. The residual then contains input-related structure, and the residual–input coherence correspondingly increases. Thus, rising coherence with amplitude is interpreted as a signature of nonlinear, amplitude-dependent fluid behavior that cannot be represented within a linear time-invariant model.

6.3.4. Signal-to-Noise Ratio Estimation

An equivalent signal-to-noise ratio (SNR) may be inferred directly from the magnitude-squared coherence under the assumption of additive, uncorrelated noise in the output measurement which was demonstrated thanks to the allen variance tests on IMU noise. The relationship between coherence and Signal to noise ratio (SNR) is

$$\gamma^2(f) = \frac{\mathrm{SNR}(f)}{1 + \mathrm{SNR}(f)}, \tag{6.18}$$

which can be inverted to yield

$$\mathrm{SNR}_{\mathrm{dB}}(f) = 10 \log_{10} \left(\frac{\gamma^2(f)}{1 - \gamma^2(f)} \right). \tag{6.19}$$

This expression is evaluated at the resonance and dip frequencies, providing

$$\mathrm{SNR}_{\mathrm{res}} = \mathrm{SNR}_{\mathrm{dB}}(f_{\mathrm{res}}), \qquad \mathrm{SNR}_{\mathrm{dip}} = \mathrm{SNR}_{\mathrm{dB}}(f_{\mathrm{dip}}). \tag{6.20}$$

A decreasing SNR with amplitude indicates that nonlinear or noise-like components dominate the measurement. Conversely, an increasing SNR suggests stronger deterministic dynamics driven by the input.

6.3.5. Skewness and Kurtosis of the Residual Distribution

Higher-order statistical moments of the model residual are used to detect deviations from Gaussian behavior, which may indicate nonlinearities arising from fluid sloshing, intermittent wave breaking, or asymmetric free-surface motion.

Let the residual be standardized as

$$z(t) = \frac{e(t) - \mu}{\sigma}, \tag{6.21}$$

where μ and σ are the sample mean and standard deviation. The skewness is computed as

$$\mathrm{Skew} = \frac{1}{N} \sum_{t=1}^{N} z(t)^3, \tag{6.22}$$

and measures asymmetry of the residual distribution.

The kurtosis is

$$\mathrm{Kurt} = \frac{1}{N} \sum_{t=1}^{N} z(t)^4, \tag{6.23}$$

where a Gaussian distribution satisfies $\mathrm{Kurt} = 3$. Values exceeding three indicate heavy-tailed behavior and impulsive events, both characteristic of nonlinear fluid behavior.

Non-zero skewness or excess kurtosis therefore provide strong evidence that the residual is not explained by a linear model with Gaussian noise, reinforcing the presence of nonlinear fluid structure coupling.

6.3.6. Cross-axis energy fraction and frequency-domain leakage

To quantify how much of the platform motion departs from pure rotation about the intended control axis, two complementary metrics are used: the Cross-axis Energy Fraction (CEF)) and the frequency-domain leakage ratio. These measures provide insight into how the fluid induced dynamics redistribute energy away from the commanded axis of rotation in both the time and frequency domains.

The cross-axis energy fraction evaluates the proportion of kinetic energy that appears in the off-axis rotational components. It is defined from the instantaneous angular rates as

$$\mathrm{CEF}(t) = \frac{\omega_x^2(t) + \omega_y^2(t)}{\omega_x^2(t) + \omega_y^2(t) + \omega_z^2(t)},$$

which takes values between zero and one. A value close to zero indicates that the motion is dominated by the commanded z-axis rotation, while higher values indicate increasing amounts of wobble or unwanted off-axis motion. For each run, the CEF is summarised using its median value over the in-band sweep region, providing a single representative number.

The second metric, the frequency-domain leakage ratio $L(f)$, assesses the off-axis motion directly from the frequency response functions. It is defined as

$$L(f) = \frac{\sqrt{|H_x(f)|^2 + |H_y(f)|^2}}{|H_z(f)|},$$

which combines the off-axis gains H_x and H_y into a single measure relative to the main-axis gain H_z. A value of zero corresponds to perfectly aligned motion in the frequency domain, while larger values indicate stronger contributions in the off-axis channels. For analysis, $L(f)$ is condensed into an in-band RMS value over the 1.25 to 3.5 Hz sweep region.

Together, the CEF and leakage ratio provide a compact description of off-axis behavior. The CEF captures how off-axis energy evolves during the time-domain sweep, while the leakage ratio quantifies the degree to which this off-axis content manifests in the frequency domain. The trends observed in Figure 7.15 and Figure 7.16 therefore form the primary outputs of the time-domain cross-axis analysis.

In the absence of fluid motion, the orthogonal-axis signals contain only noise, leading to small values of R_{XZ} and R_{YZ}. However, a moving free surface introduces additional restoring torques that couple energy from the primary mode into the lateral axes, especially on the rotating platform. Increases in these ratios around resonance can show how energy is being dispersed into other axes outside of the preferred Z axis.

6.3.7. Qualitative fluid observations

Qualitative observations where recorded for each excitation amplitude and fill level. The number of characteristics recorded is presented in subsection 6.3.7, the complete table of observations is found in Appendix A. An example of linear fluid sloshing is found in Figure 6.8 and an example of rotary fluid sloshing is found in Figure 6.9. At higher excitation levels and especially at larger fill levels the platform

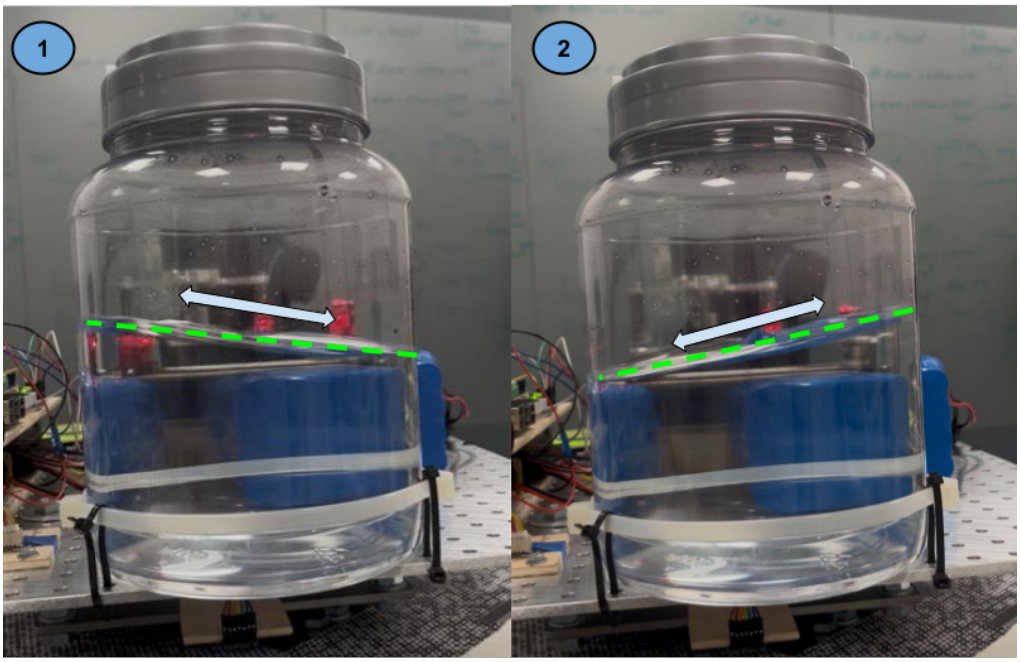

Figure 6.8: Linear Slosh wave sweep amplitude 0.05Nm at 10cm fill level

was observed moving along the x and y rotation axes due to the large static and dynamic unbalancing of the fluid in stable rotary cycles.

- Pendulum behavior, side to side fluid movement
- Rotary sloshing, fluid rotates on itself either stable or unstable
- Fluid surface breaking
- On - Off sloshing behavioral entering and exiting an excited state
- Platform movements and and vibrations or observations of platform movement in other axes

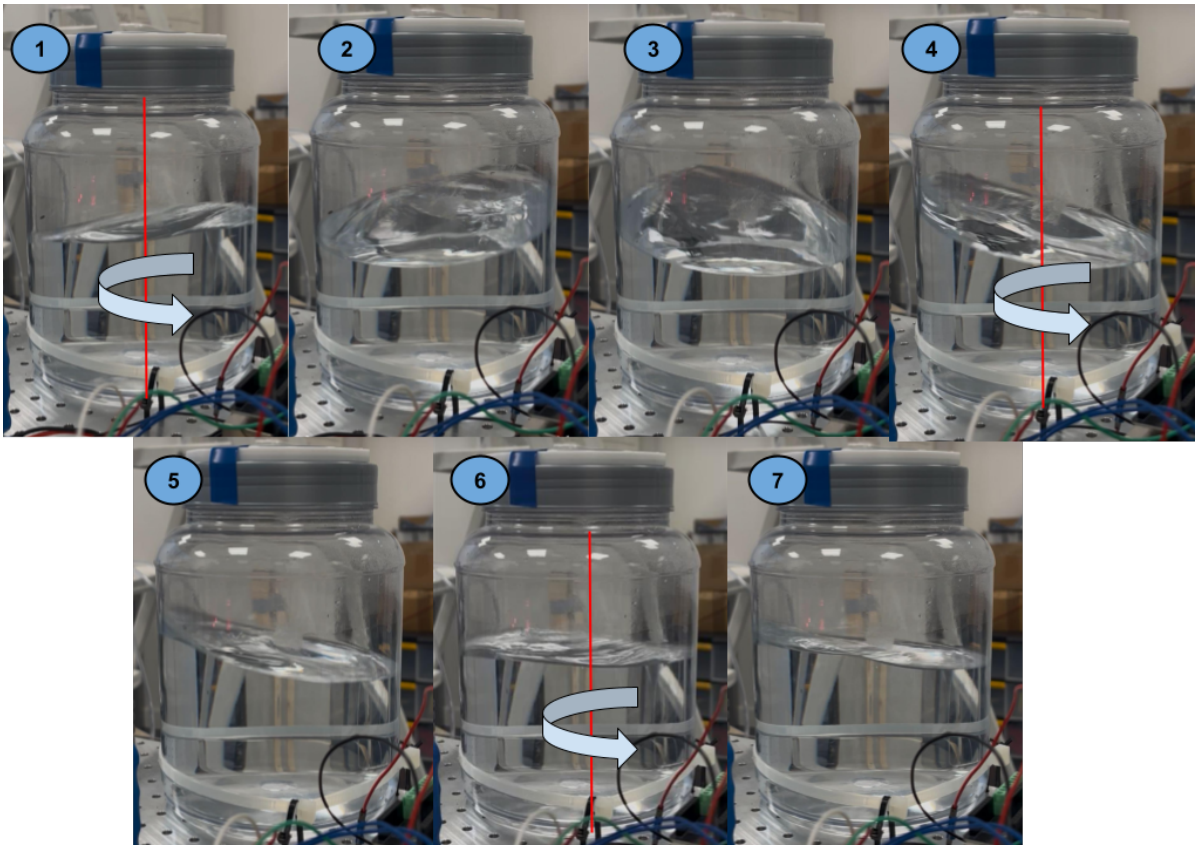

Figure 6.9: Rotary Sloshing wave at sweep amplitude 0.25Nm at 10cm fill level

7

Results

In this chapter the results of experimental and synthetic data are analyzed using metrics presented in the previous chapter. In this chapter the frequency response analysis, model fitting accuracy in time and frequency domains, signal coherence, signal-to-noise ratios, cross-axis energy effects, and Bond number equivalency comparisons between the testbed and space conditions are presented.

7.1. Final Results

The aim of the experiments was to subject a circular vertical tank at two fill heights with sweeps of increasing amplitude with the objective to observe the transition between linear and nonlinear sloshing. The two fill levels chosen where 5 cm and 10 cm while the sweep amplitudes in torque where 0.0125, 0.025, 0.05, 0.075, 0.10, 0.125, 0.15, 0.175, 0.20, 0.225 and 0.25 Nm. As the sweeps need to be very slow to accurately show transitions in the coupled platform-sloshing behavior, the sweep rate is 1200 sec/Hz. All runs where swept between 1.25 and 3.5 Hz and therefore took 45 minutes each to complete.

7.1.1. FRF interpretation

The evolution of the resonance and dip frequencies is shown for the experimental results in Figure 7.1 and for the synthetic dataset in Figure 7.2. In the experimental case, both f_{res} and f_{dip} vary noticeably with excitation amplitude for the 5 cm and 10 cm fill heights. As the input torque increases, the resonance and dip frequencies separate more clearly, which leads to an increasing frequency offset $\Delta f = f_{\text{res}} - f_{\text{dip}}$. Such amplitude dependent shifts are a classical indication of nonlinear behavior, reported in subsection 2.3.3 since the apparent natural frequency of the system is no longer independent of the excitation level. In contrast, the synthetic results show almost no variation of f_{res} or f_{dip} with amplitude, which is consistent with the underlying linear model.

There is nevertheless a generally good agreement between the experimental and synthetic values of both f_{res} and f_{dip} across the full amplitude range. For both fill levels, the synthetic model predicts resonance and dip frequencies that lie close to the experimentally identified values at moderate and high amplitudes, where the signal quality is highest as shown later on in subsection 6.3.4. This agreement indicates that the synthetic model captures the main linear characteristics of the system, and that the deviations observed at low amplitudes are more likely linked to measurement limitations than to differences in underlying dynamics.

In both the experimental and synthetic data, the values of f_{res} start off higher at the lowest excitation amplitudes and then dip. Because this feature is also present in the synthetic dataset, where nonlinear fluid effects are absent, it is likely associated with the reduced signal to noise ratio at very small inputs rather than with a physical change in the system. The synthetic data also shows a small initial change in Δf, after which Δf remains essentially constant for all higher amplitudes. This behavior is compatible with a linear and amplitude invariant system, and the initial deviation is most likely related to the frequency matching procedure being more sensitive to noise at low input levels.

The notch depth behavior, shown in the right panels of Figure 7.1 and Figure 7.2, highlights an additional difference between the experimental and synthetic responses. In the experimental measurements, the notch depth generally decreases as the excitation amplitude increases. This indicates that the resonance feature in the frequency domain becomes less pronounced at higher amplitudes, which suggests that the energy associated with the main resonance is reduced or redistributed as the response becomes more nonlinear. The experimental notch depths are also substantially higher in magnitude than the synthetic ones, particularly at low amplitudes, which reflects the stronger in band amplification and sharper resonance observed in the real system.

In the synthetic results, the opposite trend is observed. Here, the notch depth increases with excitation amplitude. This is the expected behavior for a linear system, where an increase in input energy produces a proportional increase in output energy. As the input amplitude is raised, the resonance signature simply scales, leading to a deeper and more clearly defined notch. The synthetic notch depths remain significantly smaller in absolute terms when compared with the experimental ones, which is consistent with the reduced energy content and idealized dynamics of the linear model. The contrast between the decreasing experimental notch depths and the increasing synthetic notch depths therefore supports the interpretation that the real system exhibits nonlinear dynamics, while the synthetic model behaves in a linear and amplitude invariant manner.

7.1.2. Fitting

The fitting percentage of experimental and synthetic data in both time domain and frequency domain is presented in the following subsection.

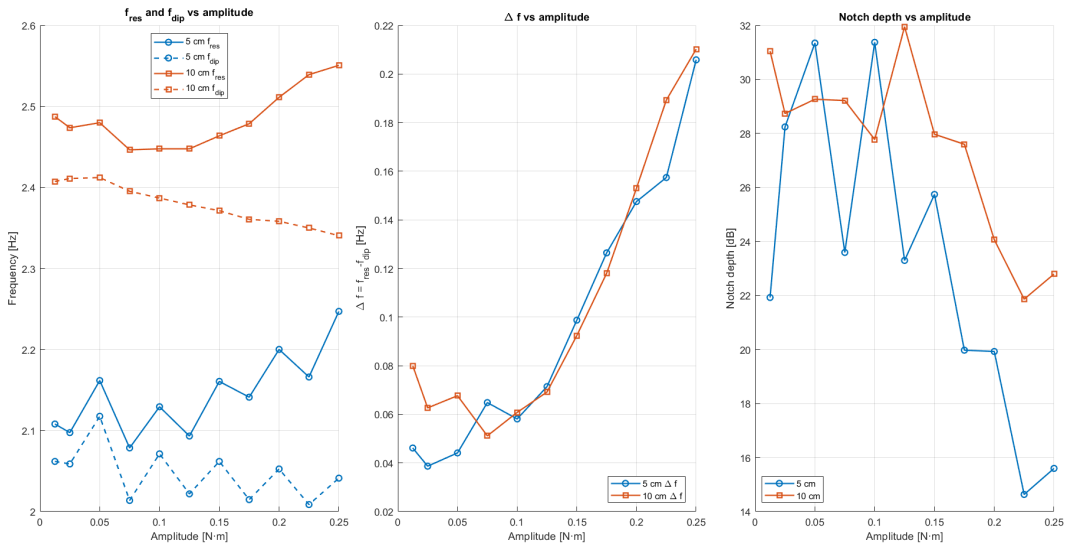

Figure 7.1: FRF features vs amplitude experimental

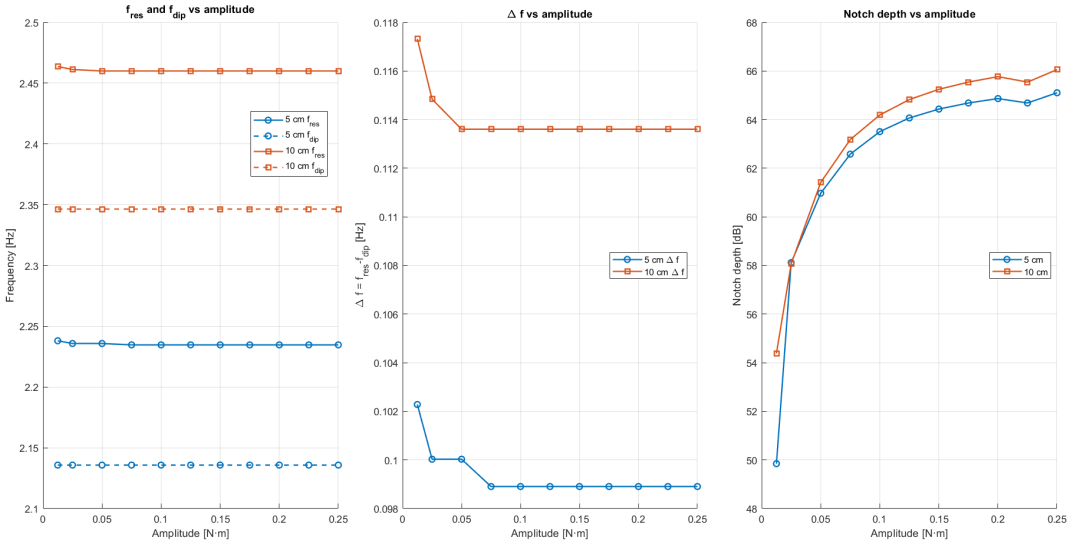

Figure 7.2: FRF features vs amplitude synthetic

Time Domain Fit

The time domain Fit percent behavior is shown for the experimental data in Figure 7.3 and for the synthetic dataset in Figure 7.4. Inspection of experimental results exhibit an inverted U shaped trend for both fill heights in Figure 7.3. The Fit percent is modest at very low amplitudes, increases to its highest values around $0.1\,\mathrm{N}\cdot\mathrm{m}$, and then gradually decreases again. This suggests that the region near $0.1\,\mathrm{N}\cdot\mathrm{m}$ may correspond to the most linear operating range. Even at the lowest point, the Fit percent remains close to 60 percent, indicating that the identified model reproduces the measured behavior relatively well across all tested amplitudes.

The Fit percentage is obtained by re-propagating the identified transfer function through the measured input. Because this process does not include the nonlinear friction (section 5.2) present on the real platform, differences between the measured and predicted signals appear, especially at operating points where friction has a stronger influence. This unmodeled effect contributes to the variation and inverted U shape observed in the experimental curve.

The synthetic dataset shows a different trend: although it begins at a similar fit percent, the value decreases steadily with increasing amplitude and stabilizes near 20 percent at higher excitation levels. This behavior possibly reflects differences in fluid damping and platform coupling in the simplified synthetic model. These effects are not captured by the frequency domain identification performed with *tfest* [50] (seen in subsection 6.1.3), which explains the growing mismatch when the model is evaluated in the time domain.

In summary, the experimental time domain match shows good predictive accuracy for all amplitudes, while the synthetic model diverges as amplitude increases. This contrast is indicative with the presence of unmodeled nonlinearities in the real platform and the simplified damping representation used to generate the synthetic data.

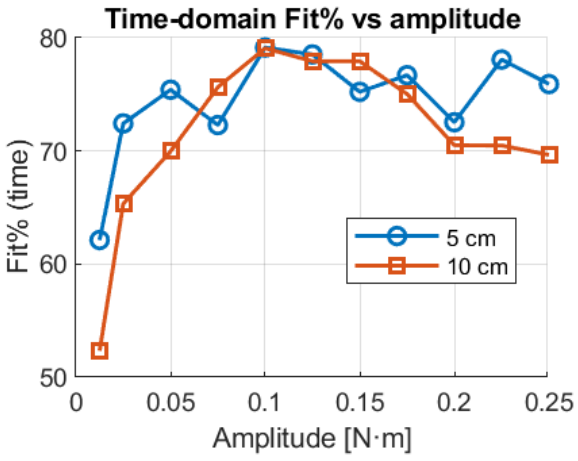

Figure 7.3: Time Domain Fitting of experimental data

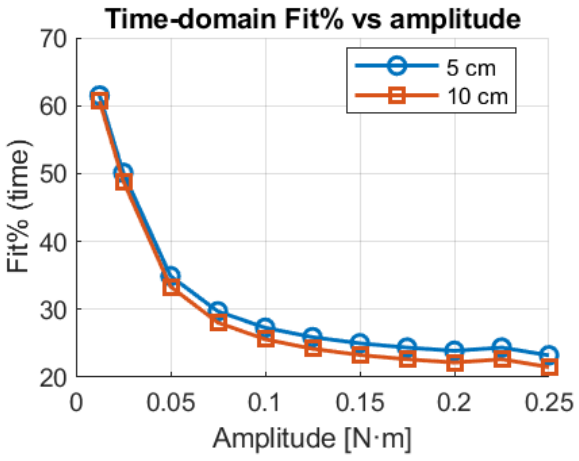

Figure 7.4: Time domain fitting on synthetic data

Frequency Domain fit

The frequency domain Fit percent for the experimental data in Figure 7.7 shows a downward trend with increasing amplitude for both fill heights. The highest Fit percent values occur at the lowest excitation levels, after which the fit quality steadily degrades. This behavior is consistent with the progressive appearance of nonlinear effects in the fluid response, which were observed earlier in the FRF characteristics. As these nonlinearities strengthen with amplitude, the ability of a transfer function represent the system diminishes, resulting in a lower frequency domain Fit percent. This is because transfer functions are only applicable to linear systems, therefore a transfer function representation of a nonlinear system is not possible. A clear example of this is seen in Figure 7.5 and Figure 7.6 where the clear difference in FRF shape can be seen between a 5cm fill level run subjected to 0.0125 Nm and 0.25 Nm amplitude. Clearly at higher amplitudes nonlinear behavior is also visually evident as extra ”squiggles” present in the FRF.

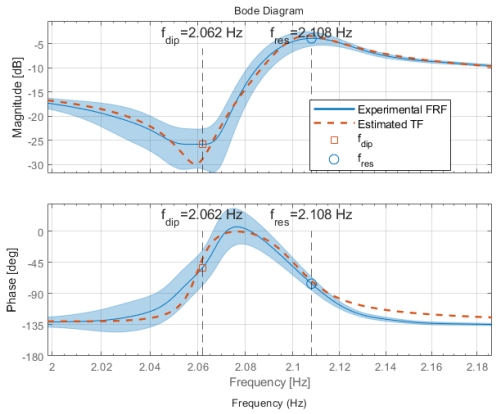

Figure 7.5: FRF 0.0125 Nm amplitude

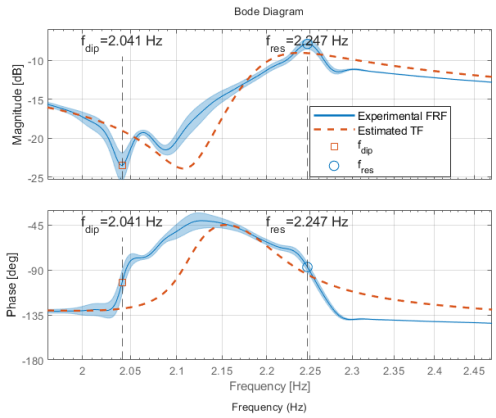

Figure 7.6: FRF 0.25 Nm amplitude

The synthetic results in Figure 7.8 display a different pattern. The Fit percent is lowest for the smallest amplitude and improves for all higher amplitudes. This initial reduction is likely caused by the low signal to noise ratio at very small input levels, where the platform motion is minimal and the estimated FRF is therefore more sensitive to measurement noise. Once the excitation is sufficiently large, the synthetic Fit percent remains relatively stable, which is expected for a linear model without amplitude dependent effects.

It is also worth noting that the highest experimental Fit percent aligns with the highest synthetic fit percentage. This agreement suggests that at the lowest amplitudes, where the fluid motion is weaker and the system behaves more linearly, the synthetic model provides a close representation of the dominant dynamics captured in the experiment. As the amplitude increases, the synthetic fit percentage remains stable while the experimental fit percentage decreases, highlighting the growing influence of nonlinear fluid behavior in the real system.

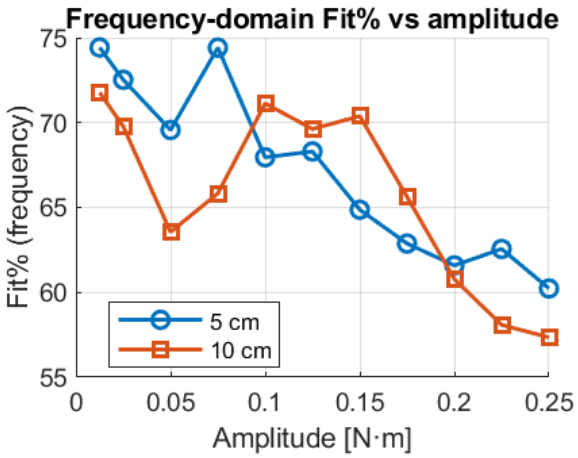

Figure 7.7: Frequency Domain Fitting experimental model

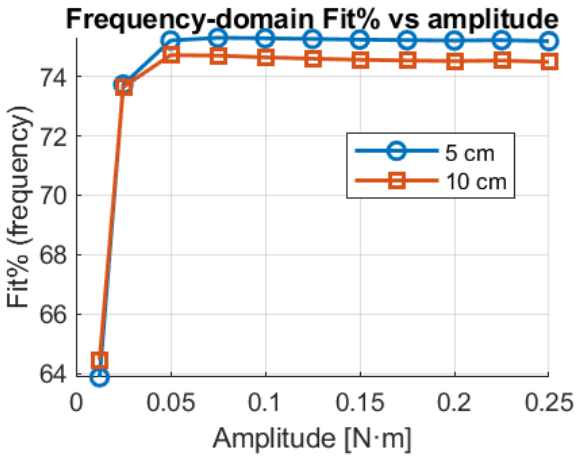

Figure 7.8: Frequency domain fitting synthetic model

7.1.3. Coherence

The residual to input mean coherence between the model residual $e(t)$ and the input torque $u(t)$ is shown for the experimental data in Figure 7.9 and for the synthetic dataset in Figure 7.10. The coherence value reported is the average over the frequency band between the identified f_{res} and f_{dip}, so it reflects how well the fitted model removes linearly explainable structure around the main resonance. A low mean coherence indicates that the identified transfer function has captured most of the linear input to output relation in this band, whereas a high coherence implies that a significant fraction of the response remains linearly correlated with the input and is therefore attributed to unmodeled dynamics or nonlinear behavior.

In the synthetic dataset, the mean residual to input coherence starts at relatively high values for the smallest amplitudes and then decreases steadily as the excitation increases, before settling on a lower plateau. At higher amplitudes the synthetic coherence typically falls between 0.25 and 0.35, indicating that the linear three pole two zero model explains most of the input correlated behavior in this band once the signal to noise ratio is sufficient. The initially higher coherence values at small amplitudes are consistent with the poorer signal to noise ratio in that region, where the residuals appear more correlated with the input simply because the platform motion is very small.

The experimental dataset shows the opposite trend. Here the mean coherence increases from low initial values and then levels off above approximately $0.05\,\text{N}\cdot\text{m}$. Across the mid and high amplitude range the coherence generally lies between 0.45 and 0.65 depending on fill height. These higher values indicate that a significant amount of structure remains in the residuals and that this structure is still correlated with the input. This behavior is consistent with the presence of nonlinear or unmodeled fluid effects in the frequency band between f_{res} and f_{dip}. Although the coherence does not grow without bound, the elevated plateau across amplitudes shows that the linear model is unable to fully remove the input correlated component of the response once the fluid motion becomes more energetic.

Overall, the absolute coherence values highlight the difference between the two systems. The synthetic

model settles into a low coherence range that indicates good linear predictability once noise is overcome, while the experimental system exhibits noticeably higher coherence levels that point to persistent nonlinear or unmodeled dynamics in the relevant frequency band.

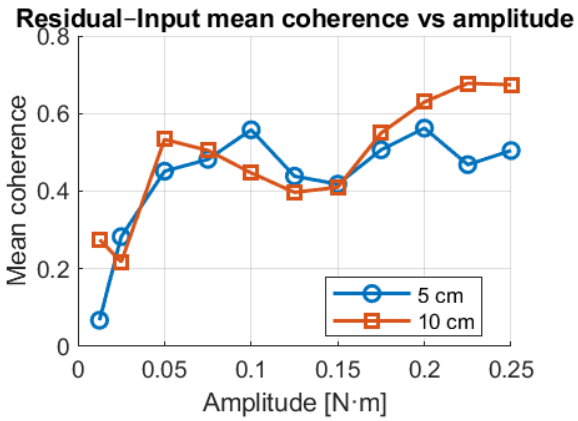

Figure 7.9: Coherence vs amplituide experimental

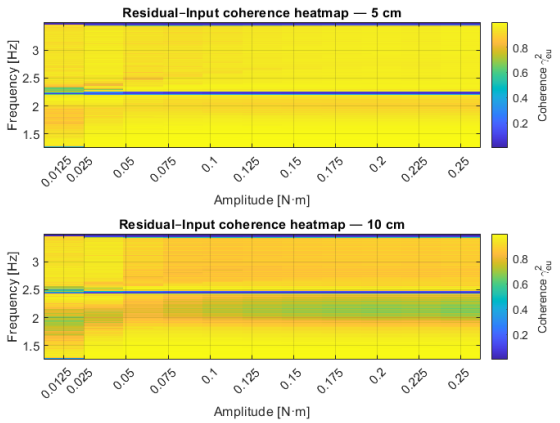

Figure 7.10: Coherence vs amplitude synthetic

Coherance Heatmap

The residual to input coherence heatmaps shown in Figure 7.11 and Figure 7.12 illustrate how the coherence varies across the full frequency range swept for different excitation amplitudes. At low amplitudes, both fill heights display regions of reduced coherence, which is most pronounced near the primary resonance band. This behavior arises because the platform motion is smallest at these amplitudes, resulting in a low signal to noise ratio and a reduced correlation between the residual and the input.

As the excitation amplitude increases, the coherence structure changes. In the experimental heatmaps, broad regions of lower coherence emerge around the resonance frequency for intermediate and higher amplitudes. This gradual reduction in coherence indicates that an increasing portion of the output cannot be captured by a linear model. The expansion of these low coherence bands with amplitude is therefore consistent with the onset and growth of nonlinear fluid behavior identified in the earlier frequency response analysis.

The synthetic heatmaps in Figure 7.12 exhibit a different pattern. Apart from the lowest amplitudes, the coherence remains high and well structured across the entire frequency range. This is expected for a linear model, where the residual should be largely uncorrelated with the input once the signal to noise ratio is adequate. The absence of low coherence regions observed in the experimental coherence plot (Figure 7.11) is an indicator of fundamental differences between the experimental and synthetic data, including how they should be represented.

Overall, these coherence heatmaps show how the predictability of the output from the input varies with both frequency and amplitude, and they further emphasize the contrast between the nonlinear behavior of the real platform and the linear nature of the synthetic model.

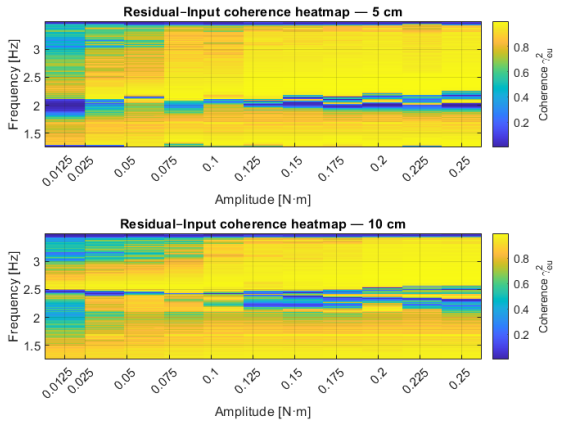

Figure 7.11: Coherence Heatmap experimental

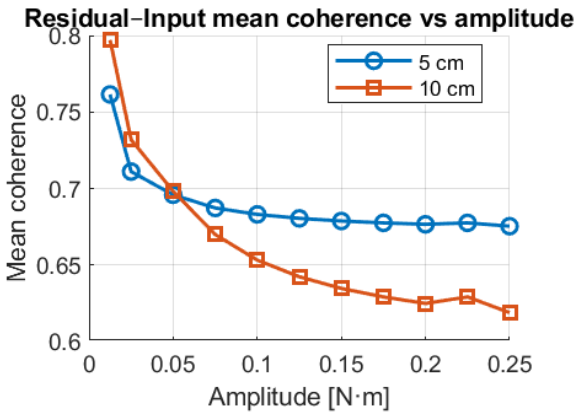

Figure 7.12: Coherence Heatmap synthetic

7.1.4. Signal to Noise Ratio

The SNR heatmaps presented in Figure 7.13 and Figure 7.14 show how the signal to noise ratio varies across frequency for different excitation amplitudes. In the experimental data, the SNR is lowest at the smallest amplitudes for both fill heights. This is expected, since the platform motion is minimal and the measured response contains a larger relative noise contribution. Once the amplitude increases, the SNR rapidly improves and remains relatively stable across most of the frequency range. The strongest SNR is consistently observed around the main resonance band, which reflects the higher energy content of the response in this region.

As the excitation amplitude grows further, the experimental SNR field becomes slightly more irregular, with small variations appearing across the resonance region. These changes remain modest but suggest that nonlinearities in the fluid and platform dynamics redistribute energy more broadly across the spectrum. This behavior is consistent with the earlier observations of amplitude dependent frequency shifts and reduced model coherence, both of which indicate departures from purely linear motion at higher input levels.

The synthetic SNR heatmaps in Figure 7.14 exhibit a more uniform pattern. Aside from the very lowest amplitudes, where the SNR is again reduced due to limited motion, the synthetic SNR remains stable and highly structured across all frequencies and amplitudes. This behavior is characteristic of a linear and noise limited system, where increased excitation simply scales the output without introducing new spectral features. The absence of the small irregular variations seen in the experimental heatmaps further highlights the lack of nonlinear energy redistribution in the synthetic model.

Overall, the SNR results confirm that low amplitude tests are limited by measurement noise, while higher amplitude tests reveal subtle but consistent signs of nonlinear behavior in the experimental platform. The synthetic model, by contrast, maintains a clean and amplitude invariant SNR structure, as expected from its linear formulation.

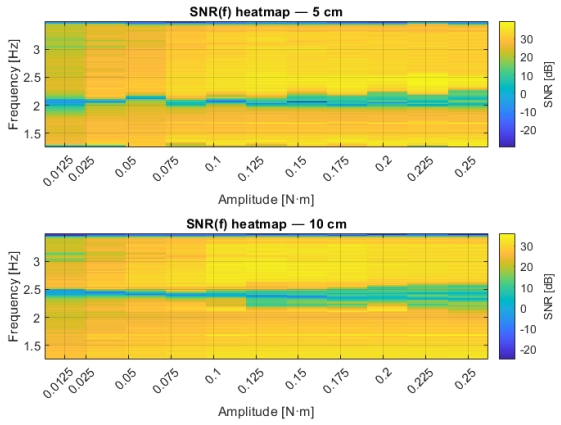

Figure 7.13: SNR Heatmap experimental

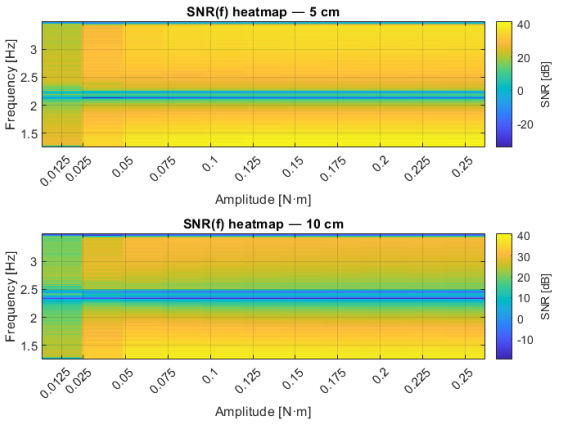

Figure 7.14: SNR Heatmap synthetic

7.1.5. Cross axis energy fractions and leakage ratios

The cross axis energy fraction and the frequency domain leakage trends are shown in Figure 7.15, with the corresponding leakage heatmaps presented in Figure 7.16. The CEF plot shows that at the lowest excitation amplitudes the ratio of off axis to on axis energy is close to one for both fill heights. At these amplitudes the platform motion is extremely small and the noise floor dominates the measured angular rates, so the apparent off axis energy is larger than the true platform rotation. As the excitation increases, the CEF drops rapidly and settles to values near zero for amplitudes above approximately $0.1\,\mathrm{N}\cdot\mathrm{m}$. This indicates that, once the input torque is sufficiently large, the platform motion becomes increasingly aligned with the intended rotation axis and little energy is redistributed into the other axes.

The frequency domain leakage ratio shows a complementary picture. For both fill heights the leakage starts at high values at the smallest amplitudes, again due to the low signal to noise ratio. As the amplitude increases, a clear reduction in leakage is observed and the curves settle onto a relatively flat plateau. Beyond this point, however, the leakage begins to rise again, particularly for the 10 cm fill height, which consistently exhibits higher leakage levels than the 5 cm case. This upward trend at higher amplitudes indicates that a portion of the motion is redistributed into the off axis directions as the fluid response becomes more energetic. This redistribution of energy is consistent with the decreasing notch depth observed in the experimental FRF data, where energy that would otherwise appear in the primary resonance peak is instead spread into additional modes and axes.

The leakage heatmaps in Figure 7.16 further illustrate this behavior across frequency. The leakage is concentrated almost exclusively in the main resonance band, with only noise present outside of this region. At low amplitudes small amounts of off axis activity are visible across multiple frequencies, but these diminish as the signal becomes stronger. At higher amplitudes a clear band of increased leakage emerges around the resonance frequency, and this band is more pronounced for the 10 cm fill height. This indicates that the off axis coupling is not broadband in nature but is tightly linked to the fluid mode excited by the sweep. The stronger leakage for larger fill heights suggests that the a larger amount of fluid in motion results in a more pronounced coupling between axes.

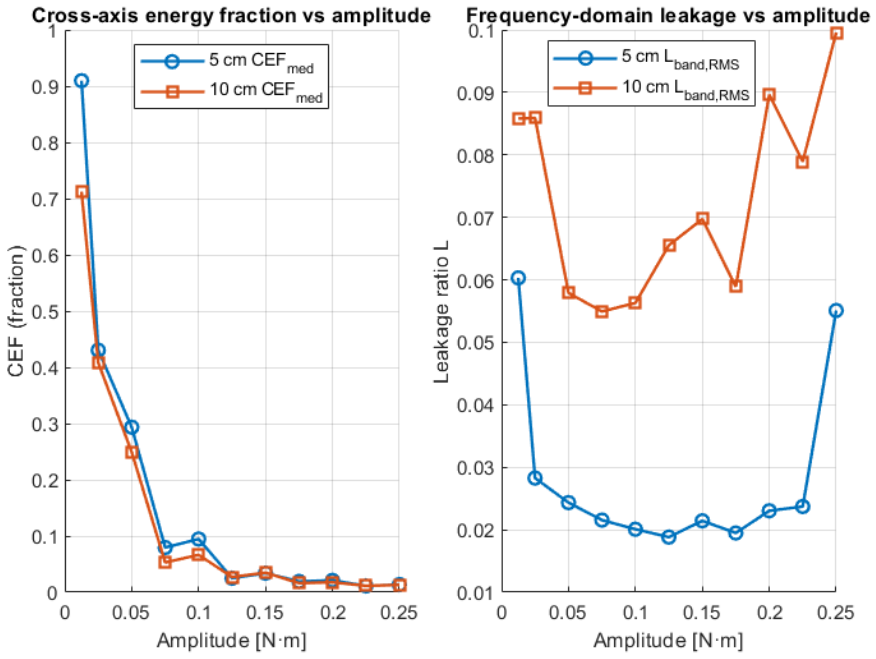

Figure 7.15: Plot showing Cross-axis Energy Fraction (time domain) and frequency domain leakage ratio (frequency domain)

Overall, the CEF and leakage results show that energy is increasingly redistributed into the off axis directions as the excitation amplitude grows, and that this redistribution is stronger for larger fill levels. These observations are consistent with the reduced notch depth in the experimental FRF's and provide further evidence that nonlinear fluid dynamics lead to a broadening and redistribution of energy that cannot be captured by the linear model.

7.2. Bond Number equivalency from testbed to space

In this section the scalability and how representative the testing platform is investigated via Bond number equivalency to find what scale tank in space would have the equivalent classical and rational bond numbers and relevant examples.

7.2.1. Classical Bond number

The classical Bond number is found using Equation 7.1 where $\rho = 997kg/m^3$ [17] and $\sigma = 0.072$ [48] for water at 25 degrees Celsius. The characteristic length is the radius of the tank (8.15cm) and g is the gravity field that the platform, $9.81ms^{-2}$ at sea level.

$$B_o = \frac{\rho g L^2}{\sigma} \tag{7.1}$$

As previously reported, the Bond number simulated in the tank at the gravity level found in the lab is 902.3 which corresponds to the upper range of low-g Bond numbers as identified in chapter 2. Bond

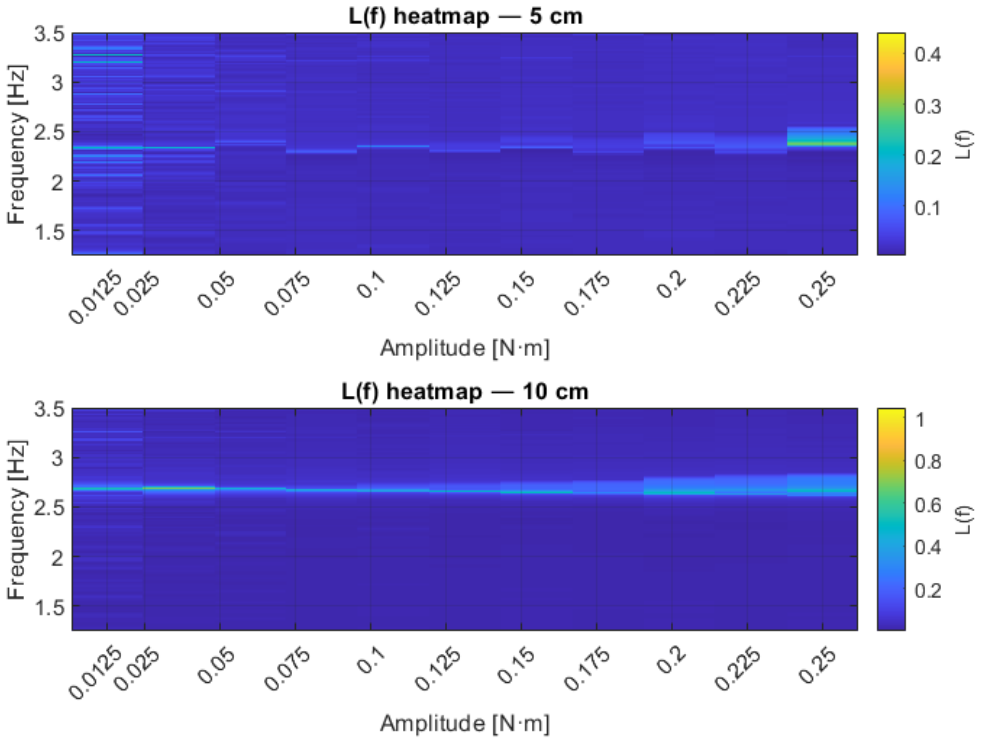

Figure 7.16: Heat map of leakage with increasing sweep amplitude

number equivalency can be conducted to find to which tank radius and acceleration level this corresponds to in a space setting. In order to do this Equation 7.1 is inverted in the form of Equation 7.2.

$$L = \sqrt{\frac{B_o \sigma}{g \rho}} \tag{7.2}$$

By sweeping over different values of accelerations g, a plot can be constructed representing what combinations of tank radius and acceleration produce a Bond number of 902.3, then they can be compared with existing launch vehicles to see if the scenarios outlined are realistic.

The target of comparison will be a well known and well documented upper stage: the Centaur designed by Lockheed Martin. It has a wet mass of 18800 kg, propellant mass of 16700kg [25]. A length of 9m a diameter of 4.3m and a main engine thrust of 147kN [25]. The Centaur upper stage is also equipped with a Reaction Control System (RCS), it is composed of 12 individual hydrazine thrusters each emitting 4.4N of thrust [40]. The thrusters are disposed in 2 groups of 2 and 2 groups of 4. The propellant for the main engine (and of interest for sloshing) is LOX and LH2 [25] and for the purposes of this analysis only the LOX tank will be focused on. The density of LOX at -200 deg C is $1141 kg/m^3$ [55] and its surface tension is $13.2 * 10^-3 Nm$ [55].

Firstly, it is assumed that the internal tank diameter is 95% the dimension of the stage diameter, this is substantiated by sources reporting that the centaur is a balloon tank with outer insulation [40]. This

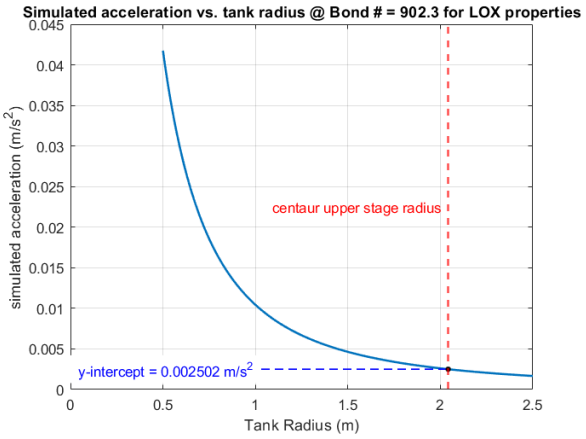

Figure 7.17: Acceleration vs tank radius for Bond number 902.3 and LOX properties

would produce an internal tank diameter of 4.085 m and therefore a radius of 2.0425 m. Combining this with the information regarding the LOX fuel, a curve based on Equation 7.2 can be plotted. As seen in Figure 7.17, the radius of the centaur tank has been recorded along with its equivalent acceleration.

Now that an equivalent acceleration of $0.002502m/s^2$ has been identified, it needs to be checked weather this is realistic for something that may have been experienced in flight. This will simply be done by employing $F = ma$ to the point in flight where the upper stage is full and has just been ignited so the engine is at max power.

$$a_{main} = \frac{147000}{18000} = 7.8191ms^{-2}$$

This is clearly 3 orders of magnitude larger than the equivalent acceleration needed to reproduce the Bond number of 902.3 which was present during experimentation. An alternative calculation is proposed where the upper stage has depleted 50% of its fuel supply and is being reoriented by firing one cluster of 4 Reaction Control Thrusters (RCS) thrusters and one cluster of 2 thrusters, for a total of 6 4.4N thrusters acting together.

$$a_{RCS} = \frac{4.4 \cdot 6}{10450} = 0.0025ms^{-2}$$

This configuration of propellant fill level and thruster activation matched the laboratory Bond numbers. This shows an equivalency between the sloshing tank containing water at 25 deg C having radius 8.15 cm at $9.81ms^{-2}$, and a 2.0425 m radius LOX tank at -200 dec C and $0.0025ms^{-2}$. The scenario of 6 thrusters firing during an attitude adjustment after having burned 50% of the propellant is realistic as the Centaur has relight capabilities [40].

This Bond number equivalency demonstrates that the sloshing tank in laboratory conditions is comparable to an equivalent realistic scenario in space. While the Centaur upper stage is definitely on the

larger end of possible upper stages, it still shows that the TRACTOR platforms results are applicable to scenarios that exist in space. Comparisons with more modern upper stages such as the ISAR Spectrum rocket where attempted but unfortunately due to lack of data could not be completed. Generally speaking, Bond numbers of smaller tanks undergoing a stronger acceleration are more easily reproducible by the TRACTOR platform with the current size tank.

7.2.2. Rotational Bond number

Following on from the classical Bond number equivalency, the same thing may be done utilising the rotational Bond number as identified in chapter 2. To relate the platform angular motion to conditions relevant for spacecraft propellant tanks, the peak angular accelerations measured on the platform are mapped to the angular acceleration that would produce the same rotational Bond number in a spacecraft tank. This allows us to infer the effective tank diameter that the platform corresponds to when operating at a given excitation level.

For rotational manoeuvres, the rotational Bond number is defined as

$$Bo_{\mathrm{rot}} = \frac{\rho\,\alpha\,R^3}{\sigma}, \tag{7.3}$$

where ρ is the liquid density, σ the surface tension, α the angular acceleration and R the tank radius. This expression follows directly from the inertial Bond number formulation presented in [26], with the characteristic length chosen as the tank radius as discussed in chapter 2.

The procedure is as follows: first, the Z-axis angular acceleration $\alpha(t)$ is obtained from the debiased angular rate $\omega_Z(t)$ using a centered finite-difference estimate, which has been cross-checked using a local polynomial derivative. The peak value α_{peak} within each constant-torque segment is extracted and used to form the experimental Bond number

$$Bo_{\mathrm{exp}} = \frac{\rho\,\alpha_{\mathrm{peak}}\,R_{\mathrm{plat}}^3}{\sigma}.$$

To determine the equivalent spacecraft tank radius corresponding to a target angular acceleration α_{target}, the Bond numbers are matched and the equivalent radius is obtained as

$$R_{\mathrm{eq}} = \left(\frac{Bo_{\mathrm{exp}}\,\sigma}{\rho\,\alpha_{\mathrm{target}}}\right)^{1/3}, \qquad D_{\mathrm{eq}} = 2R_{\mathrm{eq}}.$$

Water properties at approximately 25°C are used, with $\rho = 1000\,\mathrm{kg/m^3}$ and $\sigma = 0.072\,\mathrm{N/m}$, and the representative spacecraft angular acceleration is taken as $\alpha_{\mathrm{target}} = 5 \times 10^{-3}\,\mathrm{rad/s^2}$. This is one order of magnitude larger than the angular acceleration typically experienced by highly agile spacecraft as seen in by [26], however this acceleration was chosen as it produced feasible equivalent realistic sloshing tanks.

Applying this procedure to the experimental data yields the following representative values:

- For $\tau_{cmd} = 0.25\,\mathrm{N\,m}$, the measured peak acceleration $\alpha_{\mathrm{peak}} = 2.21\,\mathrm{rad/s^2}$ and a rotational Bond number of 45.87 it corresponds to an equivalent tank diameter of $D_{\mathrm{eq}} = \mathbf{1.2416\,m}$.

- For $\tau_{cmd} = 0.0125\,\mathrm{N\,m}$, the peak acceleration $\alpha_{\mathrm{peak}} = 0.222\,\mathrm{rad/s^2}$ and a rotational Bond number of 4.62 corresponds to $D_{\mathrm{eq}} = \mathbf{0.5778\,m}$.

These values are consistent with the cube-root dependence in Equation 7.3, where Bo_{rot} scales as αR^3. While being too large to be representative on any satellite that is currently operated in space, these numbers can be representative of an upper stage of a rocket. Often upper stages have to coast from the moment of burn off until the moment of re-lighting on interplanetary orbits. During this time a tank between 0.5 - 1.2m in diameter with fill levels of 50% could be subjected to angular accelerations of in the magnitude of $5 \times 10^{-3}\,\mathrm{rad/s^2}$ due to RCS as shown previously with the Centaur upper stage. The TRACTOR platform in its slosh configuration would produce equivalent Bond numbers to this on orbit scenario. The acceleration itself would depend on the exact configuration of the RCS, their given thrust levels and stage mass. The moment arm of the RCS thrusters was unfortunately not available in the Centaur [40] documentation therefore the acceleration could not be confirmed.

Albeit that it is a limited scenario as most satellite tanks are of a smaller diameter than the equivalent diameters calculated, the Bond number in the tank can be adjusted by adding a larger tank to the platform (as the Bond number scales with tank radius), this would allow for the modeling of smaller equivalent on orbit tanks. This would however come at the cost of potentially unbalancing the platform, resulting in more spillover movement into the undesired x and y axes.

8

Conclusions and Future Recommendations

In this chapter overall conclusions from the results presented in chapter 7 are discussed along with the strengths and weaknesses of the analysis done. The research questions proposed in chapter 4 are answered along with recommendations to be implemented that may be useful to whoever pursues this work in the future.

8.1. Conclusions from data

The experimental results presented in this thesis show that the dynamics of the platform and fluid system do not fall neatly into a single linear or nonlinear regime, but instead evolve in a way that depends strongly on the excitation amplitude, fill height, and the coupled behavior between platform, fluid, and bearing friction. One of the clearest observations is the redistribution of energy into the off axis directions at higher fill levels and higher excitation amplitudes. This behaviour is seen in both the energy measurements of the cross axis and the leakage ratios of the frequency domain, and it is consistent with the decreasing depth of the notch observed in the experimental FRFs. In the synthetic simulations the energy remains confined to the commanded axis of rotation, as expected from a purely linear model, whereas in the experimental system part of the input energy is diverted into fluid rotation and off axis platform motion. The conclusion for this is that at high amplitude, sweeps cannot be modeled with a simple linear pendulum as they lack fidelity, more advanced modeling of the platform and a rotary sloshing model needs to be constructed in order for the synthetic data to match reality closely.

This energy dispersion appears to originate from the transition of the fluid from a predominantly side to side sloshing mode into a rotating motion. Once the liquid begins to rotate, it introduces a dynamic imbalance that couples into the platform motion. At higher amplitudes this imbalance is amplified, and

the energy that would contribute to the main axis response instead populates the orthogonal axes or is absorbed into rotational fluid motion. Since the rotating liquid can spin faster than the imposed sweep frequency, some of the energy is not captured by the IMU and therefore does not appear in the FRF magnitude. This helps explain why the notch depth decreases with amplitude in the experimental data but remains monotonic in the synthetic model.

At the lowest excitation amplitudes, where linear motion was expected to be most clearly visible, the results show the opposite. The time domain Fit percentage, the residual input coherence, and the frequency domain Fit percent all show degraded performance in this region. Two factors likely contribute. First, the low signal to noise ratio hides the genuine linear motion. The platform and fluid motions are extremely small, and the IMU noise dominates the measurement, reducing the clarity of the identified FRFs and coherence estimates. Second, the system operates in the Stribeck region of the bearing friction at these low speeds, where the friction torque depends strongly on velocity. This introduces a platform nonlinearity that can obscure the underlying fluid response even when the fluid behavior itself is close to linear. These two effects together explain why the lowest amplitude data do not form a reliable reference for a clean linear sloshing regime.

The qualitative observations presented in Appendix A indicate that rotary sloshing first appears at sweep amplitudes around $0.1\,\mathrm{N}\cdot\mathrm{m}$. Several of the quantitative measures in this chapter show changes in the same amplitude region. Both fill heights exhibit a divergence in the frequency domain features around 0.1 Nm amplitude subsection 2.3.3, and the leakage and coherence metrics begin to deviate from their low amplitude behavior. These correlations support the idea that nonlinearities associated with the fluid motion begin to play a more substantial role once the excitation reaches this level. However, the transition from linear to nonlinear behavior is not sharply defined. Data suggests that several mechanisms are active, including nonlinear fluid dynamics, nonlinear friction in the platform bearings, and preferential directions in the platform response. These effects interact and make it difficult to isolate a single causal mechanism at any given amplitude.

Despite these complications, certain nonlinear signatures have been reliably detected. The most robust indicator is the amplitude dependent change in f_{res} and f_{dip}. The clear separation of these frequencies with increasing amplitude is a classical hallmark of nonlinear systems, as shown in subsection 2.3.3. The synthetic data, which include the nonlinear friction model and only a linear sloshing model, do not show this behavior. This distinction provides strong evidence that nonlinear sloshing has indeed been observed and that the experimental system exhibits fluid related nonlinear dynamics in addition to platform friction effects. These findings are further supported by the visual observations of rotary sloshing. The transition between linear and nonlinear sloshing as described in subsection 2.3.5 was unfortunately not observable directly as it relies on direct wave height measurements which did not occur as planned due to lack of time and direct angular measurements of the platform. While the platform itself is equipped with an optical angular encoder, it was not available for the majority of experiments and therefore accurate position readings by integration of velocity where not possible.

The behavior of the time and frequency domain Fit percents also reflects the presence of nonlinearities. The synthetic model increasingly deviates from the measured data at higher amplitudes, showing that a fixed three pole two zero model cannot account for the growing complexity of the response. The frequency domain Fit percent in particular declines steadily with amplitude, which confirms that the mismatch between the linear model and the true system widens as the nonlinear dynamics strengthen.

Finally, the residual to input coherence provides some indication of nonlinear behavior, although the interpretation of this metric is less clear. The expected trends are visible, but the sensitivity of the coherence calculation to noise and the difficulties in capturing the anti resonance accurately in the FRF limit its reliability. Nevertheless, when considered alongside the other results, it contributes to the overall picture.

Taken together, the results of this chapter show that the experimental system does not display a clean division between linear and nonlinear sloshing regimes. At low amplitudes the measurements are dominated by low coupling, sensor noise, and nonlinear friction. At high amplitudes, fluid rotation, platform imbalance, and energy leakage obscure the motion that would otherwise allow a clear interpretation. Within these constraints, however, nonlinear sloshing has been identified with confidence through consistent amplitude dependent changes in the FRF features and through qualitative video evidence. The results also underline the importance of considering both platform related nonlinearities and fluid related nonlinearities when interpreting data from rotating liquid filled tanks, especially when the goal is to separate linear and nonlinear behavior across a range of excitation amplitudes.

8.2. Answers to the Research Questions

The research questions originally proposed in chapter 4 are addressed head on and answers based on the work done during the thesis are proposed. The original research questions are reported for readers convenience and the answers presented after.

8.2.1. Reaserch Questions

RQ1 – Platform Capability

To what extent can a on-ground test platform replicate and characterize relevant sloshing regimes for spacecraft in microgravity and launch vehicles in high-g regimes?

a. Which gravity regimes expected in S/C or launcher are not reproducible and why?

b. Which distinct sloshing regimes (linear, non-linear, rotary) can be reliably induced and observed on the platform?

   b.i. Can the linear and rotary sloshing motion be decoupled in a 1 DOF testing platform?

c. What test conditions (excitation, frequency, amplitude, fill level, tank size & placement) are required to trigger each identified regime in 1g?

RQ2 – Model Validation and Real-World Modeling Implications

How accurately do existing sloshing models (linear and nonlinear) predict the behavior observed on the test platform?

a. How well does the linear model match data in the low excitation amplitude regime?

b. When and how do nonlinear models improve agreement with measurements at higher amplitudes?

c. What are the limitations in model-data agreement and what are implications for real world modeling?

c.i. Under what conditions is a linear model (spring mass) sufficient and when is a high-fidelity model warranted (conical pendulum, CFD) for capturing sloshing behavior?

c.ii. What practical design or simulation guidelines can be derived for slosh modeling in real spacecraft or launcher applications?

8.2.2. RQ1 – Platform Capability answer

1. **a.** The gravity regimes expected in spacecraft and launchers that are not reproducible on the current platform are the very low Bond numbers of the microgravity regime ($Bo < 30$), since Bond-number equivalency using Equation 7.1 and Table 5.6 shows that this would require tank diameters below roughly $5\,\mathrm{cm}$, for which the liquid mass is too small to couple measurably to the platform and IMU. In contrast, with the $d = 0.163\,\mathrm{m}$ tank, the classical Bond number is $Bo \approx 900$, i.e. at the upper end of the low g range (section 2.5), and the Bond number equivalency analysis in section section 7.2 demonstrates that these conditions are representative of realistic low g upper stage scenarios such as the Centaur LOX tank at about 50% fill during RCS firing.

   b. Linear, rotary and some strongly nonlinear sloshing regimes can be produced on the platform: this is visually confirmed by the observations in Appendix A, which show pendulum-like and rotary waves and wave breaking for increasing amplitudes (Figure 6.8, Figure 6.9), and quantitatively supported by the clear amplitude-dependent separation of resonance and dip frequencies in Figure 7.1 that is absent from the linear synthetic model (Figure 7.2).

   b.i. In principle, linear (pendulum like) and rotary sloshing motions are distinct and can be identified separately, as indicated by the qualitative video observations and FRF metrics in Appendix A and 7.1, distinct separation is seen in FRF's between linear low amplitude results in Figure 7.5 and higher amplitude nonlinear results in Figure 7.6. In practice, however, the TRACTOR data do not exhibit a clean separation between these regimes: at low amplitudes the linear slosh is obscured by low SNR (Figure 7.13) and friction-induced nonlinearities, while at higher amplitudes rotary slosh, platform imbalance, cross axis leakage Figure 7.16 and nonlinear bearing behavior section 5.2 mask a clear transition between linear and nonlinear fluid motion.

   c. The primary test condition controlling the transition from linear to nonlinear and rotary slosh-

ing is the excitation amplitude: increasing the commanded torque in the slow frequency sweeps systematically produces amplitude-dependent shifts in the FRF features signaling nonlinear behavior growth (Figure 7.1. Tank size and fill level also play a role but were only coarsely sampled (5 cm and 10 cm), and practical considerations: namely the need for sufficient liquid mass to couple to the platform and to cover the convex tank bottom meant that a relatively large, 0.163 m diameter tank and minimally 5 cm fill height were required for the IMU to detect the sloshing response.

8.2.3. RQ2 – Model Validation and Real-World Modeling Implications answer

1. **a.** The linear model matches the experimental data reasonably well in terms of dominant frequency in the low excitation regime, as shown by the comparison between synthetic and experimentally measured FRFs in Figure 7.2 and Figure 7.1. However, the SNR in the low excitation region is low (Figure 7.13), the fluid–platform coupling weakens at small amplitudes, and pure linear behavior does not appear in the coherence plots, likely due to contamination from nonlinear bearing friction (section 5.2) consistent with Stribeck type behavior at low speeds (Figure 7.9).

   b. Nonlinear sloshing models were not implemented in this thesis due to time constraints, and a linear matching strategy was therefore adopted. Nevertheless, the emergence of nonlinearities near actuation amplitudes of approximately $0.1\,\mathrm{Nm}$ and the divergence between experimental and synthetic linear responses (Figure 7.1) strongly suggest that above this level, a nonlinear model would improve agreement, provided that cross axis energy leakage (Figure 7.16) and platform nonlinearities effects not captured by the nonlinear pendulum model are accounted for.

   c. Limitations in model–data agreement arise primarily from platform–fluid coupling constraints, unmodelled disturbances such as nonlinear friction section 5.2 and preferential-direction bias section 5.4, energy leakage into non-target degrees of freedom (Figure 7.16), IMU SNR limitations (Figure 7.13), and observability limits inherent to the TRACTOR geometry and sensor placement. These factors collectively constrain the fidelity with which the experimental data can validate a sloshing model.

   c.i. A linear (spring–mass) model is sufficient for small fluid excitations at low-g Bond numbers, which in the experiments correspond to actuation amplitudes below roughly $0.1\,\mathrm{Nm}$ (Figure 7.1), Figure 7.2. Above this threshold, rotary and strongly nonlinear sloshing behaviors begin to appear, which as established in the literature and observed experimentally require higher fidelity modeling such as conical pendulum or CFD based approaches.

   c.ii. Practical modeling and design guidelines include ensuring adequate bearing selection and sizing, choosing sensors of sufficient quality and redundancy to observe fluid–structure coupling, and maintaining strict constraints on the platform so that only a single effective degree of freedom is excited. Additionally, matching Bond number conditions representative of spacecraft or launcher scenarios requires appropriate tank sizing and fill-level selection at $1g$ (section 7.2).

More detailed platform improvement recommendations are provided in chapter 8.

8.3. Reflections on Differences Between Plan and Reality

The original planning shown in Appendix B proved generally realistic and was followed closely up to the midterm checkpoint. However, the time required to develop a functioning model-matching infrastructure was significantly underestimated. Nearly two months were spent attempting to implement nonlinear least squares and time domain matching strategies before it became necessary to shift to a frequency domain approach, as the former did not yield satisfactory results. This delay increased the workload during the latter stages of the thesis and ultimately prevented the implementation of a nonlinear sloshing model.

A further challenge arose from delays in the delivery of key platform components. The previous platform relied on wired connections and lacked onboard power, while the redesigned version was ready in mid-July but could not be assembled or validated because the required components did not arrive until early October. As a result, system integration, electronics installation, and platform validation were compressed into the final phase of the project, adding additional time pressure.

Several planned experimental variations outlined in Table 3.1 could not be performed. These included mass variation studies, isolating rotary sloshing by mounting the tank on the rotation axis, changes in tank diameter, and camera based wave height measurements. Mass variation was deprioritised because it was expected to have limited influence on the transition from linear to nonlinear sloshing, and time constraints prevented its later inclusion. Investigations into tank diameter were attempted using an initial tank of $0.111\,\mathrm{m}$, but insufficient fluid platform coupling led to a change to a $0.163\,\mathrm{m}$ tank. Larger tanks could not be tested because platform imbalance became significant when larger fluid volumes oscillated near resonance. Isolating rotary sloshing was similarly infeasible due to the presence of the anti tilting rod at the rotation axis, which prevented mounting the tank centrally. Finally, the absence of a camera with sufficient memory, image quality, and mounting options prevented direct measurement of wave height, which had originally been planned but became impossible under the available time and resource constraints.

More broadly, the work highlighted the inherent challenges of experimental research. The platform frequently required debugging and unplanned troubleshooting, and issues such as characterizing the nonlinear friction consumed substantially more time than originally anticipated. These unforeseen tasks illustrate the difficulty of maintaining strict adherence to a predefined schedule when working with a complex physical system.

8.4. Platform Improvements

Improvements to the platform sensors, IMU and cameras are proposed along with correcting misalignments found and suggesting methodologies to limit the impact of nonlinear friction.

8.4.1. IMU Requirements

The current IMU imposes several limitations on the precision and interpretability of the measured platform motion. An improved unit should include direct tilt sensing, which would allow the platform inclination to be measured and corrected before each experiment. This would also make it possible to confirm whether the platform is properly balanced at the start of a run. In addition, an IMU capable of directly measuring angular acceleration would significantly reduce sensitivity to numerical noise, since the present approach relies on differentiating the angular rate measurement. A higher performance IMU would therefore enhance the quality of the data, particularly in the low amplitude regime where the signal to noise ratio is already limited.

8.4.2. Cameras

To improve the observability of the liquid motion, fixed cameras could be added to record the free surface shape and the wave dynamics throughout the experiment. Although the tests performed for this thesis were recorded using mobile phone cameras, these recordings were not suitable for complete analysis due to their limited duration relative to the forty five minute experiment length. Dedicated two dimensional cameras, similar to those used in other sloshing studies, combined with a dyed liquid against a dark background, would enable the extraction of wave height, wave shape and the precise moment at which the motion transitions from linear to rotary sloshing as done in other studies such as [57][26]. This information would complement the platform based measurements by providing a direct observation of the liquid behavior rather than only the coupled platform liquid response. The primary reason such a system was not implemented was the combination of limited time, funds and experience with camera based measurement systems.

8.4.3. Correcting Misalignment Within the Platform

Some structural elements of the platform introduce geometric imperfections that can affect the measured dynamics. An example is shown in Figure 8.1, where the central shaft and the surrounding bearing assembly are visibly misaligned. This misalignment was introduced when the bearing type was changed during development and the new mounting holes were not perfectly concentric with the central opening. As a result the main steel shaft is slightly offset from the intended axis, which likely contributes to the preferential direction observed in the experimental analysis section 5.4. Manufacturing a new aluminum top plate with precisely machined mounting holes would correct this issue. In addition, increasing the rigidity of the central support could be achieved by stacking multiple bearings or by transitioning from two to four bearing support struts to better constrain the platform to a single rotational axis.

8.4.4. Air Bearing or Suspended Platform

Since nonlinear friction in the thrust bearing has been identified as a major source of disturbance, especially at low rotational speeds, alternative support mechanisms should be considered. The current bearing has already undergone several design iterations and has reached a practical size limit of 31 mm

Figure 8.1: Misaligned central rod and bearing structure

in diameter. Reducing its size further would compromise platform stability, making it difficult to keep the center of gravity within the bearing footprint. To eliminate nonlinear friction effects entirely, two potential solutions exist.

The first option is to mount the platform on an air bearing table. Similar to an air hockey surface, this method levitates the platform on a thin cushion of air and removes mechanical contact friction. Under such conditions the dominant losses would be aerodynamic rather than mechanical. However, an air bearing introduces practical constraints, including limited experiment duration due to compressed gas supply, and a significant sensitivity to platform balance. Any static or dynamic imbalance, such as that introduced by rotating fluid, can cause noticeable nutation since the supporting air cushion distributes unevenly under asymmetric loading.

A second option is to suspend the platform from the laboratory ceiling using a thin, high strength fishing line. In this configuration the line behaves as a torsional spring with characteristics that can be modeled and compensated for. A swivel joint can be added to prevent excessive twist from accumulating in the suspension line. This approach is more accessible and less expensive than the air bearing alternative, but it shares the same requirement for precise platform balancing in order to minimize unwanted nutation.

8.5. Modeling Recommendations

In this section recommendations for improving the modeling techniques for sloshing experiments are proposed utilizing Autoregressive with Exogenous Input (ARX) and Autoregressive Moving Average with Exogenous Inputs (ARMAX) MATLAB tools, augmenting the analysis to directly include nonlinear friction in its ODEs and alternative model structures.

8.5.1. Nonlinear Time Domain Identification Using ARX and ARMAX Models

The identification results presented in this thesis show that the linear grey-box model estimated with `greyest` provides useful insight into the dominant dynamics of the platform but becomes increasingly

limited with the introduction of nonlinear friction. The model structure enforces a fixed three pole two zero linear transfer function, which cannot adapt to amplitude dependent effects such as frequency shifts, energy redistribution into off axis directions or nonlinear friction contributions. For this reason it is worthwhile to consider alternative time domain identification approaches that can better accommodate nonlinearities or model structure uncertainty.

A first candidate is to employ nonlinear ARX models. Unlike the grey-box model, an ARX structure does not assume any particular physical parametrization and instead learns the direct input–output mapping from data [29]. Nonlinear ARX models can incorporate regressors that are polynomial, wavelet based or based on neural network elements, allowing them to capture amplitude dependent changes in system gain and frequency response. This may help in modeling the different regimes of fluid behavior, including the transition from linear sloshing to rotary sloshing, without requiring a predefined analytical model. Such models could therefore be better suited for representing the soft nonlinearities that appear at intermediate amplitudes in the experimental data.

A second option is to use ARMAX models, which extend ARX by explicitly modeling the noise dynamics. This is particularly relevant for the present system because the low amplitude regime is strongly affected by sensor noise and nonlinear friction. The ARMAX structure separates the deterministic dynamics from the stochastic component, allowing for more accurate identification when the residual contains correlated disturbances [28]. This may improve performance in the low amplitude range where the signal to noise ratio is low and the differentiation of angular velocity amplifies measurement noise. By modeling the noise process explicitly, ARMAX identification could provide a more robust estimate of the underlying linear dynamics, which can then be compared against the nonlinear features extracted through the FRF analysis.

Both nonlinear ARX and ARMAX approaches also allow for model order selection and structure testing, which is a limitation of the fixed-structure grey-box model. This flexibility can help determine whether fluid nonlinearities should be treated as parameter variations within a linear framework or as genuine nonlinear contributions requiring a more expressive model class. In this way these methods could complement the grey-box identification used in the thesis and provide a more nuanced view of how fluid behavior changes across excitation levels.

8.5.2. Direct ODE-Based Modeling with Nonlinear Friction

Another possible direction for future work is to move from input output identification to a full state-space formulation in which the coupled platform liquid dynamics are described by a set of ordinary differential equations that explicitly include the nonlinear friction characteristics of the thrust bearing. In this framework the nonlinear friction law, including both the Stribeck behavior at low speeds and the velocity-dependent dissipative components, is embedded directly into the system equations rather than being approximated or compensated for through identification routines. This would remove the need for numerical differentiation of noisy IMU data and would provide a physically transparent way

of analyzing the interactions between fluid forces, platform inertia and frictional effects.

Such an approach is computationally expensive, especially if the fluid is represented with a high-fidelity model or if parameter estimation is performed through nonlinear least-squares optimization over full time histories. However, with access to more powerful computational resources, this method could enable joint estimation of platform parameters, friction terms and fluid response features within a single unified model. This would also provide a natural route for comparing synthetic simulations and experimental data at the EoM level, which may help resolve some of the ambiguities observed in the present study at both low and high excitation amplitudes.

Although not practical within the scope of this thesis, a direct ODE-based model with embedded nonlinear friction represents a promising long-term approach for achieving a higher degree of physical realism and for improving the interpret ability of the nonlinear phenomena identified in the experimental results.

8.5.3. Alternative Model Structures

In the present work the identification strategy relies on matching a fixed three pole two zero linear model to data that contain both linear and nonlinear sloshing behavior. While this provides a consistent baseline across all amplitudes, the limited model order restricts the ability of the identification to represent sharper resonance features or the gradual broadening and shifting of peaks observed in the experimental FRFs. Increasing the number of poles and zeros in the linear model would give the estimator greater flexibility in reproducing the curvature of the resonance and anti resonance regions. A higher order model can better approximate the underlying fluid structure dynamics by capturing multiple lightly damped modes or by shaping the frequency response more precisely around the dominant sloshing peak. This may reduce the residual structure attributed to unmodeled dynamics and lead to a clearer separation between genuine nonlinear effects and artifacts of insufficient model complexity.

A second direction is to shift the matching approach from a purely linear representation to a model that reflects the expected physics of the sloshing modes. Given that the experimental results exhibit a transition from planar, pendulum like sloshing to rotary sloshing, an alternative approach would be to identify a conical sloshing model and examine the amplitudes for which this model ceases to match the data. In such a framework the breakdown of the conical model would serve as an indicator of when the sloshing ceases to behave like a coherent rotating mode and transitions into a more irregular nonlinear regime. This may help resolve some of the ambiguities encountered in this thesis, particularly the difficulty in distinguishing between nonlinear fluid behavior, nonlinear friction effects and energy leakage into off axis motion.

By combining a more flexible linear model structure with physics informed model matching, it would be possible to localize more precisely the amplitude regions where the dominant sloshing mechanism changes. This could improve the interpretability of the nonlinear signatures observed experimentally and provide a more robust basis for comparing against future synthetic or high fidelity computational models.

An equivalent mechanical model for rotary sloshing is presented in chapter 2 specifically in subsection 2.3.3 and Figure 2.8. The associated equations and formulation is reported int that section, during the course of this thesis it was unfortunately not in included due to time constraints.

8.6. Experimental Improvements

Improvements in experimentation strategies have been identified and reported below, these are increasing the torque capability of the reaction wheel to enable broadband excitation and integrating physical pendulums onto the platform.

8.6.1. Broadband tests

At present, the platform is excited using sine sweeps with a linearly increasing frequency. While effective at exciting a dominant sloshing mode, this approach never allows the excitation to remain stationary, extends the experiment duration, and complicates the identification of additional modes. To address these limitations, broadband excitation is proposed, in which the reaction wheel provides a constant-amplitude sinusoid with superimposed colored noise over the 0–20 Hz band, causing the TRACTOR platform with sloshing tank to act as a dynamic filter. Under such conditions, the primary resonant frequency is expected to emerge clearly, while secondary or tertiary modes may also appear with reduced amplitudes and weaker coupling. Moreover, broadband excitation permits the sloshing motion to develop under steady forcing, rather than being continually disrupted by a time-varying excitation frequency. This approach was attempted; however, the reaction wheel saturated in torque and was unable to realize the desired excitation profile.

This limitation is fundamentally linked to the finite torque capability of the reaction wheel. Unlike sine sweep inputs, which concentrate excitation energy at a single frequency at any given time, broadband signals contain simultaneous frequency components across the entire excitation band. For a rate based excitation, the actuator torque required to track the commanded signal is governed by the rigid-body rotational dynamics

$$\tau(t) = I\,\dot{\omega}(t), \tag{8.1}$$

where I denotes the inertia of the platform and $\omega(t)$ is the body angular rate. As a consequence, the highest-frequency components of the broadband input dominate the torque requirement, since the time derivative of $\omega(t)$ scales linearly with frequency. Imposing the maximum available reaction wheel torque therefore places a strict upper bound on the admissible excitation amplitude at the cutoff frequency. For the present system, with a platform inertia of $I = 0.32241\ \mathrm{kg\,m^2}$ and a reaction wheel torque limit of $0.26\ \mathrm{N\,m}$, this constraint severely restricts the achievable excitation bandwidth and amplitude, preventing the simultaneous generation of colored-noise excitation and sufficient forcing to robustly excite multiple sloshing modes without saturation.

From a design perspective, these observations provide a clear methodology for establishing torque requirements for a future reaction wheel upgrade. Given a desired excitation bandwidth with upper cutoff

frequency f_c and a target angular rate amplitude Ω at that frequency, the minimum required actuator torque can be estimated by evaluating the corresponding angular acceleration demand. For a sinusoidal component at f_c, the associated torque amplitude is given by

$$\tau_{\text{amp}} = I\, 2\pi f_c\, \omega. \tag{8.2}$$

This relationship provides a physically motivated framework for selecting the torque capability of a future reaction wheel, directly linking actuator sizing to the intended excitation bandwidth and amplitude, and ensuring that broadband tests can be conducted without saturation.

8.6.2. Differing tank shape

Alternative tank shapes could be evaluated, for example a long square (rectangular) tank mounted tangentially to the platform's rotation axis. While rectangular tanks possess as many sloshing modes as symmetry axes, the geometry may provide a constraint against rotary sloshing and reveal additional nonlinear behaviors (e.g., wave breaking or nonstandard waveforms). These effects may yield more informative experimental results, as the resulting nonlinear sloshing could couple more strongly with the platform and thus be easier to identify from the IMU data.

8.6.3. Physical Pendulum Models

A practical alternative is to mount physical pendulums on the platform: a constrained 2D pendulum to emulate linear (planar) sloshing and a 3D conical pendulum to emulate rotary sloshing. By selecting pendulum length and bob mass to match the equivalent liquid parameters (e.g., mode 1 values in Table 8.1) using relations from the literature [16], the pendulums can serve as a direct model matching proxy. The key advantage is that platform nonlinearities (e.g., friction, imbalance) are shared between the "mechanical slosh" and the actual tank test, so discrepancies primarily reflect differences between the fluid model and its mechanical analog rather than hard to identify platform effects. Practical challenges include mechanically integrating the pendulum so it remains free from unintended supports, and the need for multiple pendulums to capture higher modes; to keep complexity manageable, this approach is best applied to a single dominant mode. However, the pendulum length reported in Table 8.1 show that 4.5 and 5.5 cm pendulums would be needed, these dimensions could be implementable in the TRACTOR platform.

Table 8.1: Mode 1 Multi-Pendulum Parameters for Two Fill Levels

Fill level	m_n	L_n	H_n	f_n [Hz]
10 cm	0.757	0.0452	0.0235	2.344
5 cm	0.627	0.0545	0.0343	2.133

References

[1] H. N. Abramson, W.-H. Chu, and Jr. Ransleben G. E. “Representation of Fuel Sloshing in Cylindrical Tanks by an Equivalent Mechanical Model”. In: *ARS Journal* 31 (1961), pp. 1697–1705.

[2] H. Norman Abramson and J. M. Ransleben. *Simulation of Fuel Sloshing Characteristics in Missile Tanks by Use of Small Models*. Tech. rep. NASA Technical Note D-395. San Antonio, Texas: Southwest Research Institute, 1960. URL: `https://ntrs.nasa.gov/citations/19980227566`.

[3] M. Alenany et al. “Guidance, Navigation, and Control of In-Orbit Assembly of Large Antennas – Technologies and Approach for IOANT”. In: *41st ESA Antenna Workshop on Antennas and RF Systems for Space Science*. Session on Innovative Antennas and Arrays. European Space Agency (ESA). Noordwijk, The Netherlands, Sept. 2023.

[4] M. Amabili, F. Pagnanelli, and M. Pellegrini. “Experimental modal analysis of a water-filled circular cylindrical tank”. In: *Fluid Structure Interaction*. Accessed from provided PDF. WIT Press, 2001, pp. 267–276.

[5] Helmut F. Bauer. “Nonlinear Mechanical Model for the Description of Propellant Sloshing”. In: *AIAA Journal* 4.9 (1966), pp. 1662–1666. DOI: `10.2514/3.3752`.

[6] F. Bugg. *Determination of Liquid Oscillation Frequency in an Inclined Right Circular Cylinder*. NASA Technical Memorandum TM X-64540. NASA, 1970.

[7] Rick Burow. “Identification of liquid sloshing dynamics by CFD analysis on board of a spin stabilized satellite”. MA thesis. University of Bremen (M.Sc. Thesis), 2016.

[8] V. Carrara and H. Kuga. “Estimating Friction Parameters in Reaction Wheels for Attitude Control”. In: *Mathematical Problems in Engineering* 13 (2013). DOI: `10.1155/2013/249674`.

[9] Yichao Chen and Mi-An Xue. “Numerical Simulation of Liquid Sloshing with Different Filling Levels Using OpenFOAM and Experimental Validation”. In: *Water* 10.12 (2018), p. 1752. DOI: `10.3390/w10121752`.

[10] L. V. Clark and D. G. Stephens. “Simulation and Scaling of Low-Gravity Slosh Frequencies and Damping”. In: *AIAA Space Simulation Symposium Preprint*. Philadelphia, Pennsylvania, Sept. 1967.

[11] K. M. Crosby et al. “A Sounding Rocket Payload Experiment on Zero Gravity Fuel Gauging Using Modal Analysis”. In: *Global Climate Change Impacts on Lake Michigan*. Wisconsin Space Grant Consortium. Kenosha, WI, 2013, pp. 1–10. URL: https://dione.carthage.edu/ojs/index.php/wsc/article/view/10.

[12] Alexis Dalmon et al. “Comparison between the FLUIDICS experiment and direct numerical simulations of fluid sloshing in spherical tanks under microgravity conditions”. In: *Microgravity Science and Technology* 31.1 (2019), pp. 123–138. ISSN: 0938-0108.

[13] Y. Delannoy, L. Brosset, and J. M. Ghidaglia. “Sloshing and Scaling: Results from the Sloshel Project”. In: *Proceedings of the Twentieth International Offshore and Polar Engineering Conference (ISOPE)*. ISOPE. Beijing, China, 2010.

[14] Y. Delannoy, L. Brosset, and J.M. Ghidaglia. “Sloshing and Scaling: Experimental Study in a Wave Canal at Two Different Scales”. In: *Proceedings of the Twentieth International Offshore and Polar Engineering Conference (ISOPE)*. ISOPE. Beijing, China, 2010.

[15] Frank T. Dodge and Luis R. Garza. *Simulated Low-Gravity Sloshing in Spherical Tanks and Cylindrical Tanks with Inverted Ellipsoidal Bottoms*. Tech. rep. Technical Report No. 6. Prepared for George C. Marshall Space Flight Center, NASA, Huntsville, Alabama. Contract NAS8-20290, Control No. DCN 1-6-75-00010, SwRI Project No. 02-1846. San Antonio, Texas: Southwest Research Institute, Feb. 1968.

[16] Franklin T. Dodge. *The New “Dynamic Behavior of Liquids in Moving Containers”*. Tech. rep. NASA, 2013.

[17] Engineering Toolbox. *Water - Density and Specific Weight*. Accessed: 2025-02-10. 2025. URL: https://www.engineeringtoolbox.com/water-density-specific-weight-d_595.html.

[18] M. Eswaran and Ujjwal K. Saha. “Sloshing of liquids in partially filled tanks – a review of experimental investigations”. In: *Ocean Systems Engineering* 1.2 (2011), pp. 131–155. DOI: 10.12989/ose.2011.1.2.131.

[19] European Cooperation for Space Standardization (ECSS). *Adoption Notice of ISO 24113: Space systems – Space debris mitigation requirements*. ECSS-U-AS-10C Rev.1. ESA-ESTEC, Requirements & Standards Division, Noordwijk, The Netherlands. Dec. 2019.

[20] L. E. Freed. *Stability of Motion of Conical Pendulums*. Technical Report GM-45 3-437. Ramo Wooldridge Co., 1957.

[21] R. E. Hutton. *An Investigation of Resonant, Nonlinear, Nonplanar Free Surface Oscillations of a Fluid*. NASA Technical Note NASA-TN-D-1870. Contract Grant: NASR-80. Space Technology Labs., Inc., Redondo Beach, CA, United States: NASA, May 1963.

[22] RA Ibrahim, VN Pilipchuk, and T Ikeda. “Recent advances in liquid sloshing dynamics”. In: *Applied Mechanics Reviews* 54.2 (2001), pp. 133–199. DOI: 10.1115/1.1357585.

[23] *ITTC – Recommended Procedures and Guidelines: Sloshing Model Tests*. Approved by the 28th ITTC Seakeeping Committee. 2017.

[24] Rumen Kobilarov et al. “Nanosatellite Design Considerations for Mission to Explore the Propellant Sloshing Problem”. In: *Journal of Multidisciplinary Engineering Science and Technology (JMEST)* 7.3 (2020), pp. 11942–11947. URL: https://www.jmest.org/wp-content/uploads/JMESTN42353389.pdf.

[25] Wiley J. Larson and James R. Wertz, eds. *Space Mission Analysis and Design*. 3rd ed. El Segundo, CA; Dordrecht; Boston; London: Microcosm Press and Kluwer Academic Publishers, 1999. ISBN: 1-881883-10-8.

[26] Jens Levenhagen and Christina Jetzschmann. *Fuel Sloshing Modelling, Identification & Control from an AOCS/GNC Engineer's Point of View*. Interagency G&C Seminar, Sloshptember 8th, 2022. Friedrichshafen and Bremen, Germany. 2022.

[27] Lennart Ljung. *System Identification: Theory for the User*. 2nd. Upper Saddle River, New Jersey: Prentice Hall PTR, 1989.

[28] MathWorks. *ARMAX Model*. Accessed: 2025-02-15. MathWorks Documentation. 2024. URL: https://www.mathworks.com/help/ident/ref/armax.html (visited on 02/15/2025).

[29] MathWorks. *ARX Model*. Accessed: 2025-02-15. MathWorks Documentation. 2024. URL: https://www.mathworks.com/help/ident/ref/arx.html (visited on 02/15/2025).

[30] MathWorks. *greyest — Estimate ODE Parameters of Linear Grey-Box Model*. System Identification Toolbox Documentation. 2024. URL: https://www.mathworks.com/help/ident/ref/greyest.html (visited on 11/25/2025).

[31] maxon motor ag. *EC 60 flat Ø60 mm, brushless, 150 watt: Motor Data Sheet*. Technical Data Sheet. February edition. Subject to change. maxon motor ag. Sachseln, Switzerland, Feb. 2025. URL: https://www.maxongroup.com/.

[32] maxon motor ag. *ESCON 50/5 Servo Controller: Hardware Reference*. Technical Manual. Edition: January 2024. Subject to change without notice. maxon motor ag. Sachseln, Switzerland, Jan. 2024. URL: https://www.maxongroup.com/.

[33] Jean Mignot. *FLUIDICS (FLUId DynamICs in Space) SLOSH4AOCS Executive Summary Report*. Tech. rep. CAD-NT-CP1007-7401-CNS. Prepared for CADMOS, Fluidics Slosh4AOCS experiment, Issue 01, Revision 00. Toulouse, France: Centre National d'Études Spatiales (CNES), Aug. 2021.

[34] NASA Advanced Supercomputing Division. *SLOSH - Simulating Liquid Sloshing*. Accessed: 2025-06-05. NASA Ames Research Center. 2015. URL: https://www.nas.nasa.gov/SC15/demos/demo12.html.

[35] Katsuhiko Ogata. *Modern Control Engineering*. Illustrated. Instrumentation and Controls Series. Upper Saddle River, NJ: Prentice Hall, 2010. ISBN: 0136156738, 9780136156734.

[36] D. Okhotsimskii. *Theory of the Motion of a Body with Cavities Partially Filled with a Liquid*. Technical Translation TT F-33. NASA, 1960.

[37] Jeb S. Orr et al. “Modeling and Simulation of Rotary Sloshing in Launch Vehicles”. In: *AAS/AIAA Space Flight Mechanics Meeting*. AAS 21-667. American Astronautical Society. Virtual, 2021.

[38] Lee D. Peterson, Edward F. Crawley, and R. John Hansman. “Nonlinear Fluid Slosh Coupled to the Dynamics of a Spacecraft”. In: *AIAA Journal* 27 (Sept. 1989). Sandia National Laboratories, MIT, Contract Grants: NAGW-21, DE-AC04-76DP-00789. ISSN: 0001-1452.

[39] Ron Potter. “Matrix formulation of multiple and partial coherence”. In: *Journal of the Acoustical Society of America* 61.3 (1977), pp. 776–781. DOI: 10.1121/1.381366.

[40] Thomas J. Rudman and Kurt L. Austad. “The Centaur Upper Stage Vehicle”. In: *4th International Conference on Launcher Technology: Space Launcher Liquid Propulsion*. Accessed from user-provided document. Lockheed Martin Space Systems Company. Liège, Belgium, 2002.

[41] Judy A. Rumerman. *A History of Aerospace Problems, Their Solutions, Their Lessons*. Tech. rep. TP-3653. NASA Technical Paper. NASA, Sept. 1996.

[42] ECSS Secretariat. *Space engineering Spacecraft mechanical loads analysis handbook ECSS-E-HB-32-26A*. ESA-ESTEC Requirements & Standards Division. Noordwijk, The Netherlands, Feb. 2013.

[43] *SKF 51104 Single Direction Thrust Ball Bearing*. https://www.skf.com. Accessed: 24 Oct. 2025.

[44] Finn Solaas. *Scaling Laws in Hydrodynamics*. https://www.ntnu.edu/documents/140152/0/Scaling+Laws+in+Hydrodynamics. Lecture notes, Norwegian University of Science and Technology (NTNU). 2018.

[45] *Space Engineering: Mechanical Loads Analysis Handbook*. ECSS-E-HB-32-26A. ESA Requirements and Standards Division. Noordwijk, The Netherlands: European Cooperation for Space Standardization (ECSS), 2013.

[46] STMicroelectronics. *LSM6DS3: iNEMO inertial module - always-on 3D accelerometer and 3D gyroscope*. Datasheet - production data. 2017. URL: https://www.st.com/resource/en/datasheet/lsm6ds3.pdf.

[47] T. E. Strikwerda et al. “NEAR Shoemaker: Major anomaly survival, delayed rendezvous and mission success”. In: *Guidance and Control 2001*. Breckenridge, CO: Guidance and Control Conference, 2001, pp. 597–614.

[48] The Engineering Toolbox. *Surface Tension of Liquids*. Accessed: 2025-02-01. 2024. URL: https://www.engineeringtoolbox.com/surface-tension-d_962.html.

[49] Inc. The MathWorks. *spa – Spectral analysis method (spa) for transfer function estimation*. Accessed: 2025-11-24. 2025. URL: https://www.mathworks.com/help/ident/ref/spa.html.

[50] Inc. The MathWorks. *tfest – Estimate transfer function model*. Accessed: 2025-11-24. 2025. URL: https://www.mathworks.com/help/ident/ref/tfest.html.

[51] Jose Francisco Briz Valero et al. "Guidance, Navigation, and Control of In-Orbit Assembly of Large Antennas – Technologies and Approach for IOANT". In: *41st ESA Antenna Workshop on Large Deployable Antennas*. Conference Paper. ESA-ESTEC, Noordwijk, The Netherlands, Oct. 2023.

[52] J.P.B. Vreeburg. "Measured States of Sloshsat FLEVO". In: *Proceedings of the 56th International Astronautical Congress (IAC)*. IAC-05-C1.2.09. International Astronautical Federation. Fukuoka, Japan, 2005.

[53] Jan P. B. Vreeburg. "Spacecraft maneuvers and slosh control". In: *IEEE Control Systems Magazine* 25.3 (2005), pp. 12–16. DOI: 10.1109/MCS.2005.1432593. URL: https://ieeexplore.ieee.org/document/1432593.

[54] Wikipedia contributors. *Falcon 1 – Third Flight*. https://en.wikipedia.org/wiki/Falcon_1Third_flight. Accessed: May 12, 2025. 2025.

[55] Wikipedia contributors. *Liquid Oxygen*. Accessed: 2025-02-10. 2025. URL: https://en.wikipedia.org/wiki/Liquid_oxygen.

[56] H. Q. Yang et al. "Prediction of Liquid Slosh Damping Using a High Resolution CFD Tool". In: *48th AIAA/ASME Joint Propulsion Conference & Exhibit (AIAA 2012-4473)*. Atlanta, GA: American Institute of Aeronautics and Astronautics, 2012.

[57] Ran Zhou et al. "Experimental and Numerical Investigation of Liquid Slosh Behavior Using Ground-Based Platforms". In: *Journal of Spacecraft and Rockets* 49.6 (Nov. 2012), pp. 1000–1008. DOI: 10.2514/1.A32052.

[58] S. Zhou, Y. Kong, S. Zhang, et al. "Numerical simulation of sloshing in the propellant tank of reusable rocket vehicle using meshfree method". In: *Computational Particle Mechanics* 10 (2023). Published online: 21 June 2022, Issue Date: February 2023, pp. 173–184. DOI: 10.1007/s40571-022-00488-4.

[59] Nikolay E. Zhukovskii. *On the Motion of a Rigid Body Having Cavities Filled with a Homogeneous Liquid*. Vol. 3. Originally published in Russian. Collected Works, 1936.

A

Qualitative observations

Table A.1: Qualitative observations for 5 cm fill level.

Amplitude [N m]	Status	Qualitative observations	Platform behavior at resonance	Date	Water temp. [□]
0.25	Done	Very small side-to-side motion prior to resonance; rapid, violent transition with splashing and intermittent resonance before settling into a large, stable rotary sloshing mode.	Strong platform nutation at resonance, with noticeable shaking.	04 Nov	24.0
0.225	Done	Brief, violent side-to-side pendulum motion when entering resonance, with splashing, followed by a large, stable rotary sloshing mode; intermittent fluid resonance persists.	Large platform nutation at resonance.	11 Nov	24.0
0.20	Done	Side-to-side pendulum motion when entering resonance, with intermittent resonance, before transition to a stable rotary cycle.	Platform nutation present at resonance.	04 Nov	24.0
0.175	Done	Side-to-side pendulum motion at resonance onset with intermittent behavior, then transition to a stable rotary cycle.	Platform nutation present at resonance.	18 Nov	25.0
0.15	Done	Side-to-side pendulum motion when entering resonance, followed by stable fluid rotation; intermittent resonance remains visible.	Platform nutation present at resonance.	04 Nov	24.0
0.125	Done	Side-to-side pendulum motion when entering resonance, followed by stable fluid rotation; intermittent resonance remains visible..	Platform nutation present at resonance.	01 Dec	25.0
0.10	Done	Side-to-side pendulum motion when entering resonance, followed by visible rotation after the pendulum phase; intermittent fluid resonance persists.	Slight platform nutation at resonance.	04 Nov	24.0
0.075	Done	Small platform motion; resonance dominated by linear side-to-side motion which is stable for most of the resonance period; weak and unstable fluid rotation appears occasionally.	Platform motion approximately flat, with no clear nutation.	19 Nov	24.5
0.050	Done	Small platform motion; resonance produces side-to-side pendulum-like fluid motion with no visible rotation; only minimal intermittent resonance.	Platform motion approximately flat, with no clear nutation.	04 Nov	24.0
0.025	Done	Small platform motion; at resonance the fluid shows side-to-side pendulum-like motion without visible rotation; minimal intermittent resonance.	Platform motion approximately flat, with no clear nutation.	04 Nov	24.0
0.0125	Done	Extremely small platform motion; at resonance the fluid exhibits small-amplitude side-to-side pendulum motion with no visible rotation.	Platform motion approximately flat, with no clear nutation.	11 Nov	23.5

Table A.2: Qualitative observations for 10 cm fill level.

Amplitude [N m]	Status	Qualitative observations	Platform behavior at resonance	Date	Water temp. [□]
0.25	Done	Very small side-to-side motion prior to resonance; rapid, violent transition with splashing and intermittent resonance before settling into a large, stable rotary sloshing mode.	Large platform nutation at resonance.	04 Nov	24.0
0.225	Done	Very small side-to-side motion prior to resonance; rapid transition into large rotary sloshing mode	Significant platform nutation reported at resonance.	01 Dec	25.0
0.20	Done	Initially linear pendulum motion which collapses into a stable rotary sloshing mode; some liquid detachment observed; rotary mode later collapses, producing on–off cycles and a return to linear motion.	Platform nutation present at resonance.	04 Nov	24.0
0.175	Done	Very brief side-to-side pendulum motion when entering resonance, followed by visible rotation after the pendulum phase; intermittent fluid resonance observed.	Platform nutation present at resonance.	18 Nov	25.0
0.15	Done	Side-to-side pendulum motion when entering resonance, with visible rotation after the pendulum phase; intermittent resonance persists.	Platform nutation present at resonance.	04 Nov	24.0
0.125	Done	Side-to-side pendulum motion when entering resonance, with visible rotation after the pendulum phase; intermittent resonance persists.	01 Dec	Platform nutation present	25.0
0.10	Done	Side-to-side pendulum motion when entering resonance, with visible rotation after the pendulum phase; intermittent resonance persists.	Slight platform nutation at resonance.	04 Nov	24.0
0.075	Done	Side-to-side pendulum motion when entering resonance, with some rotation visible after the pendulum phase; intermittent fluid resonance present.	Platform motion approximately flat, with only weak nutation.	17 Nov	24.0
0.050	Done	Small platform motion; resonance produces side-to-side pendulum-like fluid motion with no visible rotation; minimal intermittent resonance.	Platform motion approximately flat, with no clear nutation.	04 Nov	24.0
0.025	Done	Small platform motion; at	Platform motion approxi-	04 Nov	24.0

B

Gannt chart for project planning

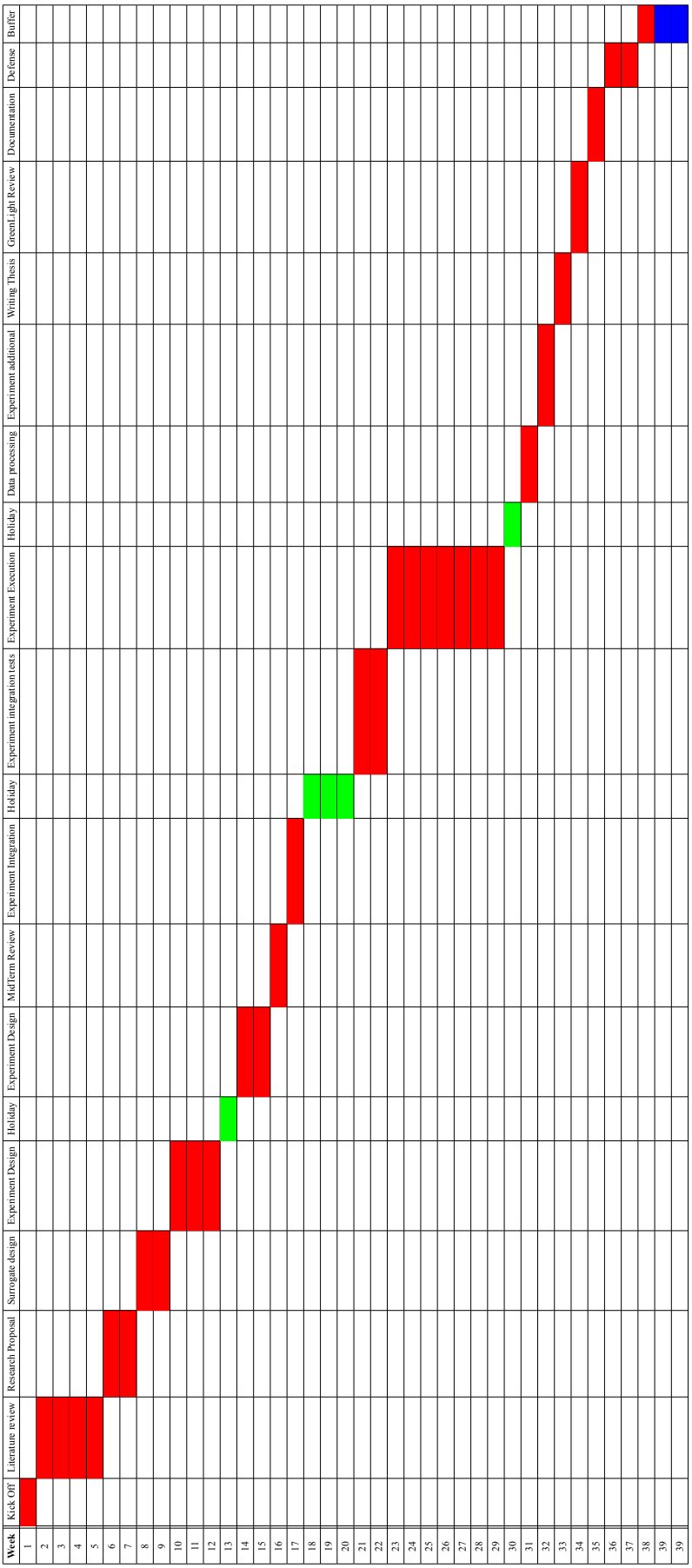

Table B.1: Gantt Chart for thesis planning